

1 **Clay minerals and continental-scale remagnetisation: a**
2 **case study of South American Neoproterozoic**
3 **carbonates**

4 **Ualisson Donardelli Bellon^{1,2}, Ricardo Ivan Ferreira Trindade¹, Wyn**
5 **Williams², Douglas Galante³, Lucy Gomes Sant'Anna⁴, Thales Pescarini¹**

6 ¹University of São Paulo, Institute of Astronomy, Geophysics and Atmospheric Sciences (IAG),

7 Department of Geophysics, São Paulo, 05360020, Brazil

8 ²University of Edinburgh, School of Geosciences, Edinburgh, EH9 3FE, Scotland

9 ³University of São Paulo, Institute of Geosciences, Department of Sedimentary and Environmental

10 Geology, São Paulo, 05508080, Brazil

11 ⁴Institute of Energy and Environment (IEE), São Paulo, 05508010, Brazil

12 **Key Points:**

- 13 • Remagnetised Neoproterozoic carbonates of South America may not consistently
14 display anomalous hysteresis parameters
- 15 • Synchrotron-based analysis revealed pseudo-single domain-sized magnetite spatially
16 correlated with aluminosilicates (smectite-illite)
- 17 • The Late Cambrian Gondwana assembly thermally reset remanence in these carbon-
18 ates, which was finally blocked during a sequential cooling

Corresponding author: Ualisson Donardelli Bellon, ualisson.bellon@usp.br

Corresponding author: Wyn Williams, wyn.williams@ed.ac.uk

Abstract

Carbonate rocks frequently undergo remagnetisation events, which can partially/completely erase their primary detrital remanence and introduce a secondary component through thermoviscous and/or chemical processes. Despite belonging to different basins hundreds of kilometres apart, the Neoproterozoic carbonate rocks of South America (over the Amazon and São Francisco cratons) exhibit a statistically indistinguishable single-polarity characteristic direction carried by monoclinic pyrrhotite and magnetite, with paleomagnetic poles far from an expected detrital remanence. We use a combination of classical rock magnetic properties and micro-to-nanoscale imaging/chemical analysis using synchrotron radiation to examine thin sections of these remagnetised carbonate rocks. Magnetic data shows that most of our samples failed to present anomalous hysteresis properties, usually referred to as part of the “fingerprints” of carbonate remagnetisation. Combining scanning electron microscopy-energy-dispersive X-ray spectroscopy (SEM-EDS), highly sensitive X-ray fluorescence (XRF), and X-ray absorption spectroscopy (XAS) revealed the presence of subhedral/anhydrous magnetite, or spherical grains with a core-shell structure of magnetite surrounded by maghemite. These grains are within the pseudo-single domain size range (as well as most of the iron sulphides) and spatially associated with potassium-bearing aluminium silicates. Although fluid percolation and organic matter maturation might play an important role, smectite-illitisation seems a crucial factor controlling the growth of these phases. X-ray diffraction analysis identifies these silicates as predominantly highly crystalline illite, suggesting exposure to epizone temperatures. Therefore, we suggest that the remanence of these rocks should have been thermally reset during the final Gondwana assembly, and locked in a successive cooling event during the Early-Middle Ordovician.

Plain Language Summary

Carbonate rocks serve as important records of ancient climates and host magnetic minerals capable of documenting the evolution of Earth’s magnetic field. Nevertheless, their initial magnetisation, acquired during sedimentation, is frequently supplanted by a secondary magnetisation, originating from various geological processes altering local thermochemical stability. For carbonate rocks, this remagnetisation process is often associated with a “magnetic fingerprint”. In South America, carbonate rocks from different sedimentary basins (hundreds of kilometres apart) exhibit statistically similar magnetic components that deviate from their formation origin, indicating secondary processes. This multidisciplinary study integrates classic paleomagnetic analysis with micro-chemical and imaging analysis to comprehend the geological phenomena responsible for remagnetising such an extensive continental area. We demonstrate that not all remagnetised samples display the anticipated magnetic fingerprint. Highly detailed chemical analysis confirms the presence of nanoscopic magnetic minerals spatially correlated with clay minerals indicating that while organic matter transformation may play a significant role, clay mineral transformation is a key phenomenon governing remagnetisation in these rocks. However, our data also supports the notion that these rocks underwent heating during the final assembly of the ancient continental landmass, Gondwana, and a sequential cool-down event is suggested as locking their magnetisation in the state observed today.

1 Introduction

The natural remanent magnetisation (NRM) carried by magnetic minerals depends on the geological processes that result in rock formation and preservation, as well as the Earth’s geomagnetic field intensity and direction (Butler, 1992). Because the magnetic mineralogy of carbonate rocks is influenced by the redox state (Pourbaix, 1974) and the chemical composition of seawater and pore water, valuable insights into the Earth’s paleoenvironmental conditions can be acquired from them (Evans & Heller, 2003; Liu et al., 2012; Roberts et al., 2013). Carbonate sedimentation, including those primarily sourced from marine organ-

isms (Grotzinger & James, 2000), allows for the correlation of paleomagnetic information in carbonate deposits with significant geological events that influenced the evolution of life (Trindade et al., 2003; Trindade & Macouin, 2007; Golovanova et al., 2023). However, the search for the primary detrital remanence of carbonate rocks often encounters single-polarity components that do not align with the corresponding age of the unit (R. D. Elmore et al., 2012). This secondary component may originate from numerous geological processes that occur below the Curie temperature (Jackson & Swanson-Hysell, 2012) of natural ferromagnetic phases and may alter the original remanence of carbonate rocks. For instance, any phenomenon able to change the preservation conditions of a rock might have the potential to cause alterations that lead to the acquisition of secondary components. We call remagnetisation the process of substituting a primary remanence with a secondary one (partially or entirely).

Remagnetisation might occur due to thermal or chemical phenomena. Thermal activation will partially (or entirely) overwrite a remanence by simply achieving the relaxation time of a population of grains at a given temperature. On the other hand, any transformation of a magnetic mineral below its Curie temperature may cause the development of a chemical remanent magnetisation (CRM) (Dunlop & Özdemir, 1997; Levi, 2007). CRMs might be approached and segmented into two subdivisions (Tauxe et al., 2018): grain growth remanent magnetisation (g-CRM), and oxidation and further reordering of magnetic moments, said to be acquiring an alteration chemical remanence (a-CRM). When nucleating from nanometric grain ranges, authigenic particles will experience a change in their thermal relaxation properties as they go from superparamagnetic (SP) to single-domain (SD) magnetic structures, yielding stable remanence records of the geomagnetic field (Dunlop & Özdemir, 1997). Depending on the local conditions, specific morphologies will arise and constrain the magnetic anisotropy properties of the particles.

Carbonate rocks make one of the most favourable examples of natural materials to study CRMs, because particular magnetic properties often arise in these rocks, resulting in what is usually called "magnetic fingerprints" of remagnetisation, observed in worldwide examples, such as (Jackson, 1990; Jackson & Swanson-Hysell, 2012; R. D. Elmore et al., 2012) single polarity components; an outstanding contribution of superparamagnetic particles; abnormal magnetic hysteresis ratios; and contradictory domain-state tests. Chemical remagnetisation of carbonate rocks might occur due to two main geological processes: sediment burial and fluid migration. During sediment burial, early diagenetic processes are strongly controlled by the redox conditions and the cellular respiration processes of microorganisms in the sedimentary column (Roberts, 2015), which might use iron oxides/hydroxides in the metabolic process together with organic matter (also causing reduction of ferric ions). Late diagenetic processes, such as clay-mineral transformations, release ions in the medium (including ferrous ions) that under the appropriate kinetic/thermodynamic conditions might lead to the growth of authigenic ferromagnetic phases (Hirt et al., 1993; Woods et al., 2002; Tohver et al., 2008). Fluid transport through the natural porosity of sedimentary rocks can induce mineral transformation, while hot basinal brines and hydrothermal associated with nearby magmatic activity/orogenies may trigger the dissolution of detrital phases and growth of others (McCabe et al., 1983; Miller & Kent, 1988; McCabe & Elmore, 1989; Jackson, 1990; Stamatakos et al., 1996; D'Agrella-Filho et al., 2000; Davidson et al., 2000; Trindade et al., 2004; Huang et al., 2017; Jiao et al., 2019; Dannemann et al., 2022; Xu et al., 2022). Finally, the maturation of organic matter and biodegradation of hydrocarbon in sedimentary basins might produce acidic solutions and disturb the local thermochemical equilibrium also contributing to the formation of new magnetic phases (Font et al., 2006; Aldana et al., 2011; Emmerton et al., 2013).

While we have identified various processes associated with remagnetisation, connecting these phenomena becomes a challenging endeavour, especially when observing remagnetisation on a continental scale. The Neoproterozoic cap carbonates of South America present a fascinating puzzle, as they span different geological basins (see Figure 1a), separated by vast

122 distances and encompassing diverse cratonic regions. Remarkably, these regions exhibit
 123 a singular-polarity characteristic component, yielding almost identical paleomagnetic fea-
 124 tures (see Figure 1b). Previous studies (e.g., (D’Agrella-Filho et al., 2000; Trindade et al.,
 125 2004; Font et al., 2006)) have highlighted the magnetic similarities in these rocks, aligning
 126 with the anticipated fingerprints of chemical remagnetisation. Despite numerous proposed
 127 mechanisms to explain remanence resetting in these basins, the mystery persists regarding
 128 how specific geological events targeted these rocks across West Gondwana, resulting in such
 129 coherent and tightly clustered paleomagnetic directions. This paper embarks on a mul-
 130 tidisciplinary study of these remagnetised carbonate rocks. Our approach combines bulk
 131 macroscopic measurements of their magnetic properties with synchrotron-based microscopic
 132 chemical and imaging analyses, aiming to understand the spatial relationships of remanence-
 133 bearing grains with surrounding minerals (especially clay minerals). Additionally, we revisit
 134 the magnetic signatures, questioning the reliability of the commonly invoked ”fingerprints
 135 of remagnetisation.”

136 Our primary objective is to establish a correlation between the observed magnetic properties
 137 in these rocks, the processes leading to chemical remanence acquisition, and the geological
 138 events responsible for inducing such transformations in West Gondwana. Through this
 139 exploration, we aim to shed light on the intricate connections between magnetic phenomena
 140 and the dynamic geological history of the region.

141 2 Geological setting and previous studies

142 Remagnetised carbonates are found throughout the whole of South America, extending from
 143 the Amazon craton towards the São Francisco-Congo craton (Font et al., 2012). We select
 144 three targets over three different basins for our study (Figure 2). Over the São Francisco
 145 craton (Figure 2a), we have sampled the cap carbonates of the Sete Lagoas Formation
 146 (Bambuú group, São Francisco basin) as well as the carbonates of the Salitre Formation
 147 (Irecê Basin). Although within the same craton, these formations are separated by hundreds
 148 of kilometres. The third target comprehends the carbonates of the Araras group, which
 149 extends through both an undeformed region of the Amazon craton (Figure 2b), but also
 150 over the deformed terrain of the Paraguay belt. The two formations studied here are the cap
 151 carbonates of the Mirassol d’Oeste Formation and an overlying unit, the Guia Formation
 152 (Figure 2e). In the following section, we summarise the geological setting of these units and
 153 discuss the results of previous studies.

154 2.1 The São Francisco and Irecê basins

155 The rocks of the Neoproterozoic São Francisco Basin (Figure 2a) can be divided into two
 156 groups: the Macaúbas at the base and the Bambuí, overlying it (Dardenne, 1978). The
 157 Bambuí Group includes a thick sequence of more than 1000 km of a siliciclastic carbonate
 158 succession in the southwest of the São Francisco Craton (Paula-Santos et al., 2015). Two
 159 large subgroups segment the Bambuí: a) a shallow basal marine stratum with two cycles
 160 of carbonate deposition and pelitic-psammitic sedimentation and; b) a superior alluvial
 161 stratum. Deformation in the Bambuí rocks progressively increases towards Neoproterozoic
 162 mobile belts (D’Agrella-Filho et al., 2000): the Brasília orogen on the east side and the
 163 Araçuaí orogen on the west side (Figure 2a), with two regions recognised as being free of
 164 deformation in the centre of the basin.

165 The age of the Bambuí has long been a matter of discussion. Early studies determined the
 166 maximum depositional ages of the Macaúbas as 900 Ma (Pedrosa-Soares et al., 2000). Di-
 167 rect dating ($^{207}\text{Pb}/^{206}\text{Pb}$) of the cap-carbonates from the lower portion of the Sete Lagoas
 168 Formation (the base of the Bambuí group) yielded ages of 740 ± 22 Ma (Babinski et al.,
 169 2007), interpreted as Sturtian cap carbonates. Later, rocks from the Sete Lagoas Formation
 170 were also dated by Rodrigues (2008): five grains from foliated argillaceous siltstones yielded
 171 ages around 610 Ma (U-Pb in zircon) and the youngest age found for a marble sample was

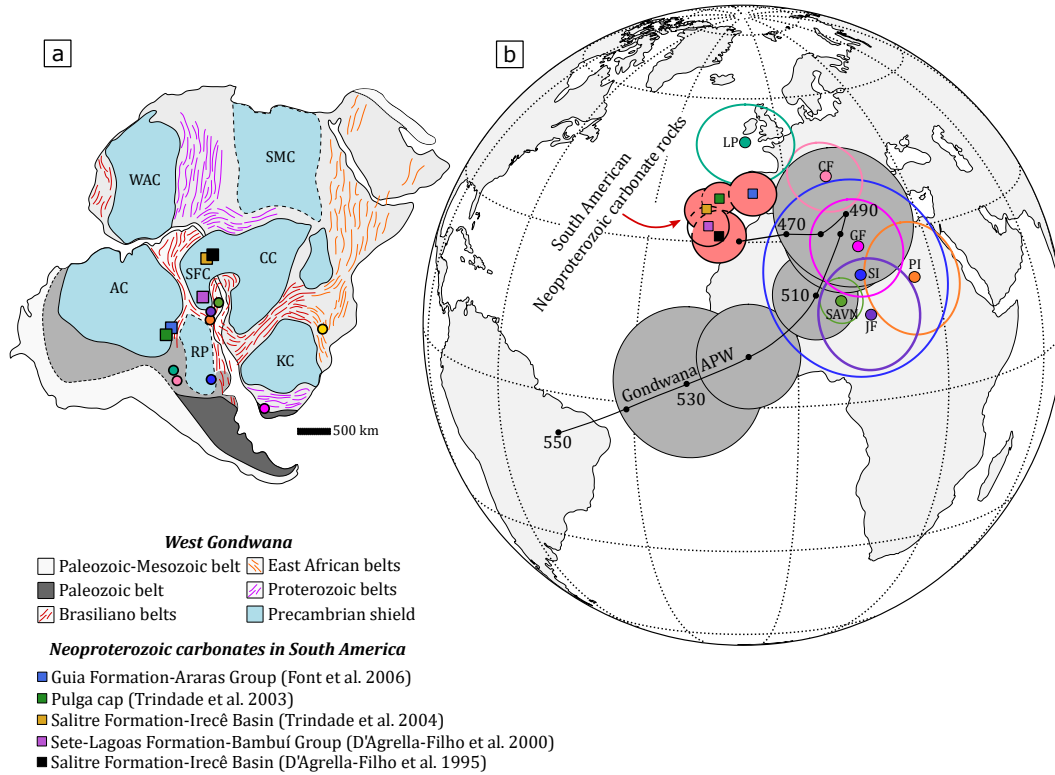


Figure 1. a) Tectonic context of the geological targets studied in this project. Spheres and squares show the geographic location of the palaeomagnetic poles from (b), modified from Alkmim et al. (2006). b) APW curve of West Gondwana considering South Africa in its current position (data from Torsvik (2012)), showing mean palaeomagnetic poles of millions of years old ages ($A95 < 20^\circ$, grey circles). Poles represented by a sphere are Late Neoproterozoic/Early-Cambrian (check Table 1) and their respective $A95^\circ$ interval, rotated to South Africa ($55.7^\circ, -34.8^\circ, 43.3^\circ$) when necessary. Squares are palaeomagnetic poles of remagnetised carbonates, centred at their $A95^\circ$ interval (pinkish). Confidence intervals of Neoproterozoic remagnetised poles from South America intersect themselves. AC: Amazon craton, WAC: West-African craton, CC: Congo Craton, SFC: São Francisco craton, RP: Rio dela Plata craton, KC: Kalahari craton, SMC: Sahara Meta craton.

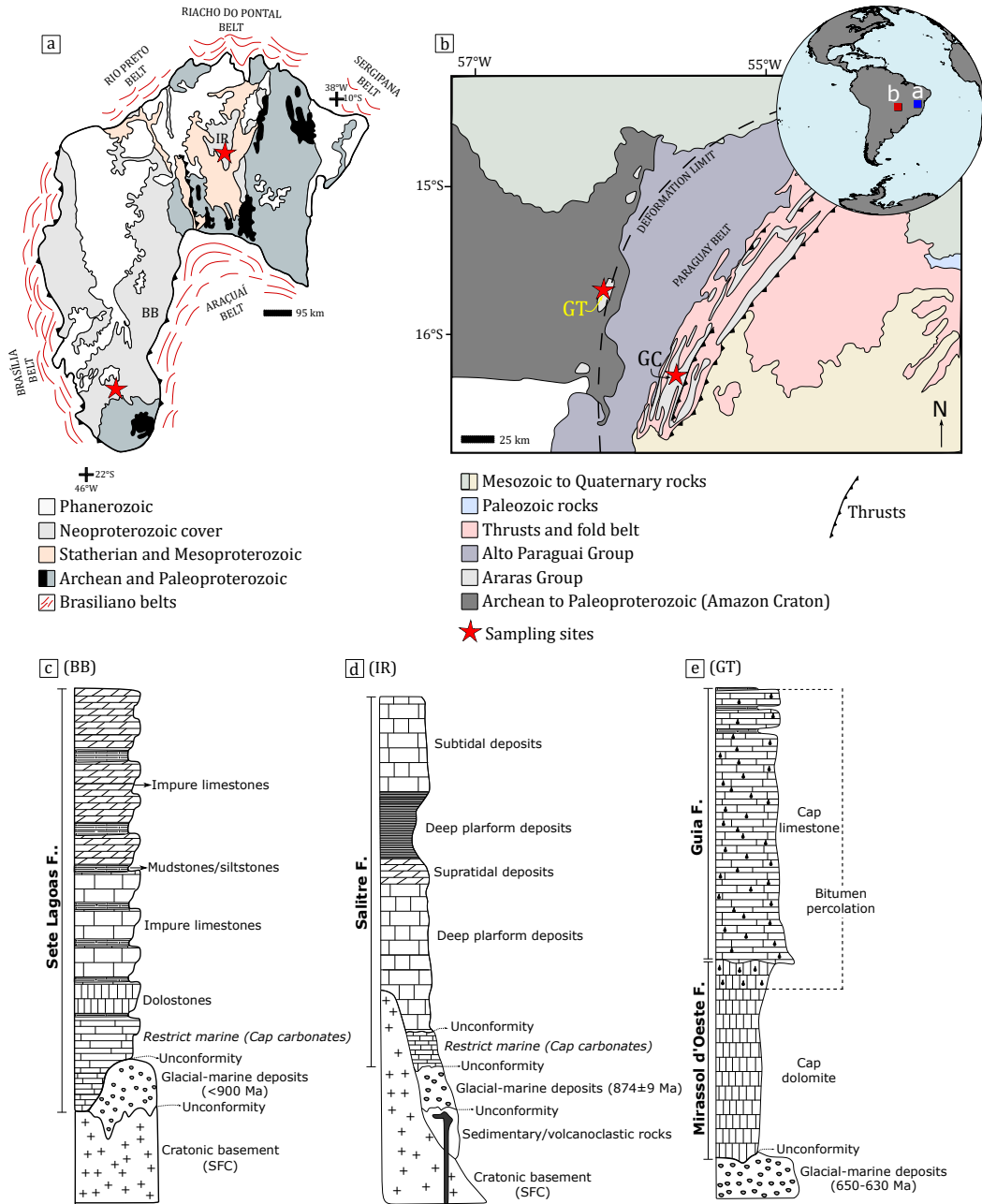


Figure 2. Simplified geological context of the studied units. a) São Francisco Craton, showing the basins of Irecê (BB) and São Francisco, where the Bambuí group lies (BB), surrounded by Neoproterozoic orogenies. Modified from Paula-Santos et al. (2015) b) Tectonic map of the southeast part of the Amazon Craton and the Paraguay belt, showing the distribution of the Araras Group in both terranes. Modified from Font et al. (2006) c, d, and e) are representative stratigraphic profiles of sections of the Bambuí, Irecê, and Araras group (over the Amazon Craton), modified from Guacaneme et al. (2017); Santana et al. (2021); Trindade et al. (2003).

172 609 Ma. More recently, Paula-Santos et al. (2015) provided new ages (U-Pb in zircon) for
 173 the Bambuí group. These authors reported maximum depositional ages, set by the youngest
 174 population of detrital grains, as 557 Ma, which would indicate that the uppermost portion
 175 of the Sete Lagoas Formation was not related to either the Sturtian or the Marinoan glacial
 176 events. D’Agrella-Filho et al. (2000) have performed a palaeomagnetic and Pb-isotopic
 177 study of the Sete Lagoas Formation, sampling rocks in what is said to be an undeformed
 178 area of the São Francisco basin. New experimental data of our work also belong to the
 179 base of the Sete Lagoas Formation. The authors reported that samples majorly showed
 180 features commonly associated with remagnetised carbonates, such as (i) wasp-waisted mag-
 181 netic hysteresis, (ii) samples with abnormally high Bcr/Bc ratios, and (iii) contradictory
 182 Lowrie-Fuller and Cisowski tests. Lowrie tests in some samples indicated the presence of
 183 a hard component with blocking temperatures around 340°C and soft components with
 184 blocking temperatures around 500°C, associated with monoclinic pyrrhotite and magnetite
 185 (respectively). Like Paleozoic carbonates, spherical magnetite and other irregularly shaped
 186 magnetites were also reported, which were analysed through SEM-EDS data. Three major
 187 components were identified in their work (check their respective palaeomagnetic poles in Fig-
 188 ure 1b): (i) a NW component (A) with negative inclination, yielding blocking temperatures
 189 between 150 – 275°, (ii) a NE (B) component with positive inclination showing blocking
 190 temperatures between 300 – 400° and (iii) a third (C) component, similar to component B
 191 but showing higher blocking temperatures (350 – 530°). While component A was assumed
 192 to be the result of a thermoviscous component, B/C components were interpreted as the
 193 result of a more ancient geomagnetic field.

194 The age of B and C components was not believed to result from a depositional remanence,
 195 since their paleolatitudes were far from the environment of carbonate development (39-
 196 5°) (D’Agrella-Filho et al., 2000). Stable and reliable Pb/Pb ages (obtained from low-
 197 Pb and high-U samples, U/Pb_i) from the undeformed area of the basin showed variable
 198 $^{207}\text{Pb}/^{206}\text{Pb}$ ages, one of the samples yielding a 520 ∓ 53 Ma age and $^{238}\text{U}/^{206}\text{Pb}$ age of 603
 199 ∓ 80 Ma. Samples from the region affected by the orogenies also showed trustworthy Pb/Pb
 200 ages, but with much greater uncertainties, whereas $^{238}\text{U}/^{204}\text{Pb} \times ^{206}\text{Pb}/^{204}\text{Pb}$ errochrons
 201 indicate a resetting of the isotopic system around 545 Ma. The authors use these data
 202 to suggest an extensive fluid percolation throughout the São Francisco Basin, which they
 203 interpreted to be constrained between 500-530 Ma by the palaeomagnetic poles calculated
 204 from the B/C components when these are compared with palaeomagnetic poles from the
 205 Gondwana APW (D’Agrella-Filho et al., 2000).

206 The Bebedouro and Salitre Formations are the equivalents of the Macaúbas and Bambuí
 207 in the Irecê basin, north of the Bambuí (in the São Francisco Craton, Figure 2a). The
 208 Bebedouro formation is a glacial/marine record that yields a wide range of ages for detrital
 209 zircons, the youngest around 875 Ma (Babinski et al., 2004; Figueiredo et al., 2009). The
 210 Salitre Formation comprises a carbonate deposit of a marine platform, with white dolostones
 211 and pink/red limestones rich in clay minerals, overlying diamictites and tillites. These
 212 carbonates have typical features of cap carbonates, such as columnar stromatolites (Misi
 213 & Kyle, 1994). Misi and Veizer (1998) suggested depositional ages around 600-670 Ma for
 214 preserved carbonate rocks of the Salitre Formation (derived from $^{87}\text{Sr}/^{86}\text{Sr}$ data compared
 215 with secular strontium isotopic curves of Neoproterozoic sea waters). More recently, Santana
 216 et al. (2021) reported that the maximum depositional age for deep ramp and subtidal to
 217 intertidal deposits of the Salitre Formation was around 670 Ma.

218 After previous studies of D’Agrella-Filho (1995), Trindade et al. (2004) performed geochrono-
 219 logical (Pb-Pb) and palaeomagnetic studies in samples from the Salitre Formation. The
 220 samples from this work belong to the same formation as reported in their works. These
 221 rocks also showed the expected behaviour of remagnetised carbonate rocks. A similar mul-
 222 ticomponent signature (to the Sete Lagoas samples) was also observed during the thermal
 223 demagnetisation of Salitre samples (Trindade et al., 2004). The calculated poles of compo-
 224 nent A (SaA) and component C (SaC) of the Salitre Formation are statistically indistin-

Table 1. Palaeomagnetic poles of remagnetised carbonates from South America, in comparison with other matching palaeomagnetic poles of similar age (same as in Figure 1. (p) – Primary magnetisation; (r) – remagnetisation; N – number of poles.

Source	Age (Ma)	PLAT	PLON	A95	Reference
BaC (r)	500-530?	30.2°	321.0°	3.8°	(D’Agrella-Filho et al., 2000)
SaC (r)	500-530?	33.0°	323.0°	4.0°	(Trindade et al., 2004)
Slt (r)	≈500?	27.5°	321.4°	4.9°	(D’Agrella-Filho, 1995)
GF (r)	≈520?	29.9°	332.6°	4.3°	(Font et al., 2006)
PcS (r)	≈520?	33.1°	326.6°	3.2°	(Trindade et al., 2003)
SAVN (p)	500	4.7°	333.2°	4.06°	(Temporim et al., 2021)
PI (r)	510-500	−0.8°	346.5°	10.2°	(D’Agrella-Filho & Pacca, 1986)
JF (r)	510-500	−0.6°	335.2°	10.0°	(D’Agrella-Filho et al., 2004)
SI (p)	≈520	5.9°	338.1°	18.1°	(Sánchez-Bettucci & Rapalini, 2002)
CF (p)	≈519	23.6°	346.5°	7.0°	(Franceschinis et al., 2019)
LP (p)	477-485	38.3°	340.4°	8.8°	(Piceda et al., 2018)
GF (p)	≈485	28.0°	14.0°	9.0°	(Bachtadse et al., 1987)

225 guishable from those from the same components (BaA and BaC) in the Bambuí formation
 226 (D’Agrella-Filho et al., 2000). Poles calculated with component B of both formations are
 227 also very close (although their confidence ellipses do not overlap, Figure 1b)). Regarding
 228 the isotopic dating, dark-grey carbonate samples of the middle-upper part of the Salitre
 229 Formation and stromatolite-bearing samples (cap carbonates) from a layer right above the
 230 diamictites of the Bebedouro formation were collected by Trindade et al. (2004) to perform
 231 Pb-Pb measurements. $^{207}\text{Pb}/^{206}\text{Pb}$ ages of the stromatolitic samples were calculated as 517
 232 ∓ 27 Ma, but it decreases to 486 ∓ 28 Ma when considering all the Pb ratios together.

233 Since the samples of Salitre and Sete Lagoas are more than 600 km apart and show such
 234 similar palaeomagnetic and isotopic-Pb data, their main hypothesis of a remagnetisation
 235 throughout the carbonates of the São Francisco craton would be considering a percolation
 236 of basinal saline fluids around 520 Ma. Therefore, the magnetic remanence carried by B/C
 237 components of both basins would be carried by authigenic ferrimagnetic minerals that crys-
 238 tallised due to reactions triggered by the percolation of an orogenic fluid associated with the
 239 Brasiliano orogenies. Although the authors bring the discussion to highlight the trigger of
 240 remagnetisation in the carbonates of these basins, they do not argue about the actual mech-
 241 anism related to the growth of the authigenic ferromagnetic grains (smectite-illitisation,
 242 biodegradation of hydrocarbon, and growth of ferrimagnetic phases, thermochemical oxida-
 243 tion, etc.), which is a role yet to be explored.

244 2.2 The Araras group

245 The Araras Group (Figure 2a) overlies the Puga Formation, a sequence of siltstones and
 246 diamictites sedimented in a glaciomarine environment (Alvarenga & Trompette, 1992). Post-
 247 glacial cap carbonates were followed by an extensive accumulation of bituminous lime mud-
 248 stones and shales that represent deep platform deposits (Nogueira et al., 2003). The cap
 249 carbonates covering the Puga Formation are pinkish dolostones and cap cementstones (bitu-
 250 minous limestones with a high amount of terrigenous) (Trindade et al., 2003). Radiometric
 251 ages of the Araras Group are not available in the literature. Rocks of the Alto Paraguay
 252 Group (which includes mudstones, sandstones, and calcarenites) overlie the Araras Group,
 253 but their age is debatable (Rb-Sr, 569 ∓ 20 Ma) (Riccomini et al., 2007). Sedimentary rocks
 254 correlated to the rocks of the Araras Group are intruded, in the Paraguay belt, by a post-
 255 tectonic granite around 528 Ma (U-Pb in zircon) (Guimarães et al., 2017), which could mark

256 a minimum depositional age. As discussed by (Nogueira & Riccomini, 2006), the presence
257 of macrofossils (e.g. Cloudina, Gaucher et al. (2003)) in the Corumbá Group (which is
258 toponomic related to the Araras Group) indicates a penecontemporary occurrence to the
259 Ediacaran biota.

260 In the basal section of the Araras Group lies the dolomites of the Mirassol d'Oeste Formation
261 and, overlying them, the limestones of the Guia Formation (Figure 2e). The Mirassol d'Oeste
262 formation is composed of laminated pinkish-dolomitic mudstones with bioturbated structures,
263 overlaid by greyish dolomites impregnated with hydrocarbon fluids and calcitic cementation
264 (Font et al., 2006). The Guia Formation is composed of bituminous limestones associated
265 with terrigenous grains. In the area over the Amazon Craton, the layers are sub-horizontal
266 and undisturbed, while the area over the Paraguay Belt is intensely deformed. Trindade et
267 al. (2003) performed palaeomagnetic studies on rocks from the Puga cap carbonates. From
268 their studies, samples near the contact with the diamictites of the Puga Formation have
269 shown a dual polarity component (A), that although similar to the current GAD yields high
270 unblocking temperatures (ca. 520°C) and positive reversal tests, indicating paleolatitudes
271 around $22 + 6^{\circ}$ and consequently suggesting its primary nature. Twenty meters above
272 in the sedimentary column, after the transition with the Guia Formation, a single polarity
273 component (B) with positive inclination steeply plunges to NE. Component B, when rotated
274 from South America towards Africa plots near the Irecê and Bambuí poles (Figure 1b), which
275 could indicate that these are also a result of a remagnetisation around the Middle-to-Late
276 Cambrian. Samples from the Mirassol d'Oeste studied in this review, as a way of comparison
277 with remagnetised units, belong to the basal stratum (the ones carrying detrital remanence)
278 as well.

279 Font et al. (2005) further investigated the remanence carried by the dolostones of the Mi-
280 rassol d'Oeste Formation. The response found in a new set of samples also showed a dual
281 polarity behaviour that passed reversal tests, indicating a palaeolatitude of 22° . High un-
282 blocking temperatures/coercivities and IRMs (isothermal remanent magnetisation) that do
283 not saturate up to 3 T indicated that haematite dominates magnetisation carried by Mi-
284 rassol d'Oeste rocks studied in their work. In the work of Trindade et al. (2003), however,
285 magnetite is clearly the main primary-remanence bearing mineral, which suggests that local
286 heterogeneities in the sedimentary column with distinct sources should exist.

287 Although the upper section of the Mirassol d'Oeste has bitumen, the Guia Formation is the
288 one where it strongly percolates. Font et al. (2006) have studied the carbonate rocks from
289 the Guia Formation in two distinct terranes: in the Tercony Quarry at the Amazon Craton
290 (where the outcrops lie undeformed) and in the Cáceres region at the Paraguay belt (where
291 the samples are affected by the orogeny). Thermal demagnetisation of these samples resulted
292 in a single polarity component that coherently matches other remagnetised Neoproterozoic
293 rocks (Figure 1b). In samples from the Amazon craton, the component held by pyrrhotite
294 is completely demagnetised around $320 - 360^{\circ}\text{C}$, while a second step of decay occurs around
295 500°C in samples from the Cáceres region, indicating that magnetite and pyrrhotite yield
296 the same direction. They reported a high contribution of SP particles in these samples,
297 especially when compared with Mirassol d'Oeste samples. A higher amount of SP particles
298 was also detected in the area affected by the Paraguay belt. Iron oxides and framboid struc-
299 tures enriched in sulphur were also spotted where bitumen is concentrated. This evidence
300 was interpreted as the result of a growing chemical remanence, probably related to hydro-
301 carbon maturation, leading to the formation of pyrrhotite. It is also suggested that smectite
302 illitisation could be responsible for the presence of magnetite, a mechanism triggered by the
303 folding of the part affected by the orogenic belt (Font et al., 2006). Nevertheless, this makes
304 the Araras Group an interesting target for deeper studies on remagnetisation, since its base
305 unit is not remagnetised while an upper unit is.

3 Methods

In our pursuit of comprehending the geological mechanisms responsible for remagnetizing basins dispersed over considerable distances, our objective is to conduct a meticulous and multidisciplinary investigation. If the magnetic properties of these rocks align with the anticipated magnetic fingerprints of remagnetised carbonates, we undertake a comprehensive analytical approach from macro to micro scales. In our methodological framework, depicted in Figure 3, we initiate the analysis by characterising the magnetic assemblages in our samples, sourced from locations previously explored in paleomagnetic studies (D’Agrella-Filho et al., 2000; Trindade et al., 2004; Font et al., 2006). Once we identify samples exhibiting the expected magnetic signatures of chemically remagnetised rocks, we progress to the compositional investigation.

We utilize X-ray diffractometry with a particular focus on clay content and conduct thermogravimetric analysis to refine our understanding of volatile components, including organic matter, within these rocks. Subsequently, with analytical findings in hand, we transition to a microscopic characterisation. This final phase involves the examination of thin sections from remagnetised units, employing synchrotron-based XRF and XAS data. This microscopic scrutiny enhances our comprehension, providing a nuanced perspective on the geological intricacies under investigation.

Because samples from the Guia Formation come from two distinct locations they were named correspondingly, Cáceres – GC in the deformed terrain, and Tangará (GT) over the Amazon craton (Figure 2b). Because the basal section of Mirassol d’Oeste (Figure 2e) formation was said to carry only a primary component, samples from the same sections studied by Trindade et al. (2003) were re-investigated, to check the occurrence of false positive “remagnetisation fingerprints”. Samples from the Irecê basin (from the Salitre Formation) are identified as IR, and samples from the Bambuí (Sete Lagoas Formation) are identified as BB (Figure 2a).

3.1 Rock magnetism

Most of the magnetic carriers of the Neoproterozoic rocks used in this project were characterised more than fifteen years ago (D’Agrella-Filho et al., 2000; Font et al., 2006; Trindade et al., 2004). An updated experimental approach, mixing traditional and updated techniques, is the first step towards a better understanding of the magnetic assemblage in these carbonate rocks. The original set of samples are classical cylindrical palaeomagnetic samples. Initially, to characterise the remanence carriers, ARMs were induced in AF demagnetised samples using a Long Core SQUID magnetometer (2G Enterprises), imparting a DC field of $100\mu T$ and AF fields from 0-10 mT along the Z-axis.

Since the contribution of grains between SP and SD states may play an important role in the fingerprints of remagnetised carbonates, we intended to semi-quantified their presence by measuring the magnetic susceptibility (of the cylindrical specimens) in low and high frequencies as well as out-of-phase and in-phase magnetic susceptibility with an Agico Kappabridge MFK1 equipment. The magnetic susceptibility of each sample was measured five times in succession and sequentially calculating their arithmetic mean. These measurements were performed in a room with a controlled temperature (21°) on the same day (to avoid any instrumental disturbances). Frequency-dependent magnetic susceptibility is traditionally used to investigate the occurrence of superparamagnetic and stable single-domain grains (Hrouda et al. (2013)). The most common frequencies for these studies are 976 Hz (low frequency) and 15616 Hz (high frequency), which were used here to investigate the susceptibility at a low-intensity AC field of $200 Am^{-1}$. The parameter χ_{FD} (Eq. 1) introduced by Dearing (1996) measures the percentage of susceptibility loss between low and high frequencies (related to the contributions of ultrafine ferromagnetic particles), in which χ_{LF} and χ_{HF} are the in-phase low and high frequencies, respectively. Hrouda (2011) introduced the χ_{FN} (Eq. 2) parameter, which despite representing the same interpretation of χ_{FD} has a decreased dependency on the operating frequency, allowing a more realistic approach. Finally, the

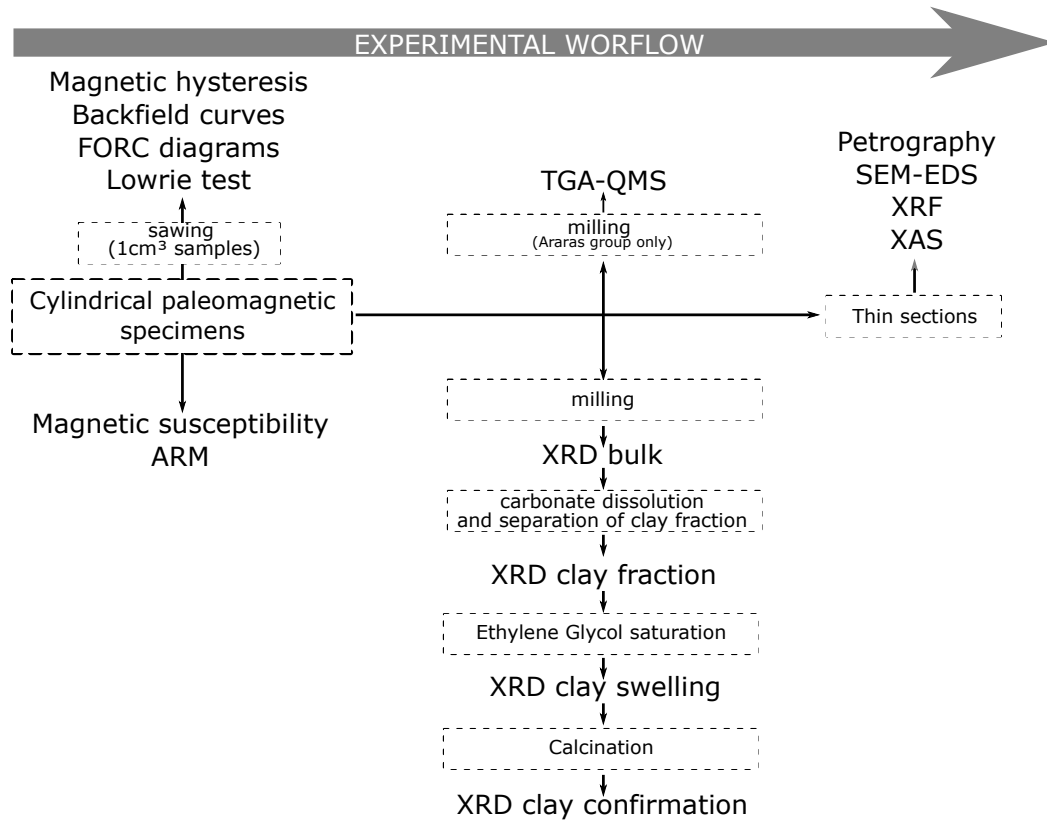


Figure 3. Experimental workflow, moving from macro to micro analysis. FORC: First Order Reversal Curves; ARM: anhysteretic remanent magnetisation; XRD: X-ray diffractometry; TGA-QMS: Thermogravimetric analysis coupled to a Quadrupole Mass Spectrometer; SEM-EDS: Scanning electron microscopy with energy dispersive X-ray spectroscopy; XRF: X-ray fluorescence; XAS: X-ray absorption spectroscopy.

357 low-frequency phase angle (δ_{LF}) related to the out-of-phase susceptibility is also an inter-
 358 esting tool used to calculate the contributions of the SP/SD threshold through the χ_{ON}
 359 parameter (Eq. 3). We make use of these parameters to verify the loss of susceptibilities in
 360 our samples.

$$\chi_{FD} = \frac{\chi_{LF} - \chi_{HF}}{\chi_{LF}} \cdot 10^2 \quad (1)$$

$$\chi_{FN} = \frac{\chi_{FD}}{\ln(HF) - \ln(LF)} \quad (2)$$

$$\chi_{FN} = 200 \cdot \pi^{-1} \tan(\delta_{LF}) \quad (3)$$

361 Sequentially, the cylindrical samples were sawed to extract small fragments for measurements
 362 in a vibrating sample magnetometer (Princeton Measurements Corporation MicroMag, VSM
 363 Model 2900; noise level $2 \cdot 10^{-9} Am^2$). Magnetic hysteresis and backfield curves were per-
 364 formed for all of them. Samples that represent the overall behaviour of each population
 365 followed by the acquirement of first-order reversal curves (FORCs, Roberts et al. (2000))
 366 to further investigate the domain state and magnetic interactions of these assemblages of
 367 particles. The use and processing of FORC (First-Order Reversal Curves) diagrams to in-
 368 vestigate the magnetic domain (for rock/environmental magnetism and palaeomagnetism
 369 fields) regarding an assemblage of ferromagnetic particles in rocks have increased over the
 370 last two decades (Carvallo et al., 2004, 2006; Egli et al., 2010; Egli, 2013; Heslop, 2020;
 371 Lascu et al., 2018; Muxworthy & Dunlop, 2002; Pike et al., 2001; Roberts et al., 2000),
 372 including its use in carbonate geological materials (Abrajevitch & Kodama, 2009; Chang,
 373 2013, 2014; Roberts et al., 2013). FORCs may offer a more robust approach than other
 374 techniques that infer magnetic domain, since the investigation occurs through scanning of
 375 different coercivities, almost as a map of the components that would form a magnetic hys-
 376 teresis. There are distinct approaches to acquiring the data for FORC diagrams. As the
 377 distribution of the FORC is calculated through a mixed second derivative of the magnetisa-
 378 tion by the reversal and applied fields (Roberts et al., 2000), any noise is strongly intensi-
 379 fied. This can be problematic when dealing with carbonate rocks, mainly because data tends to
 380 be naturally noisy.

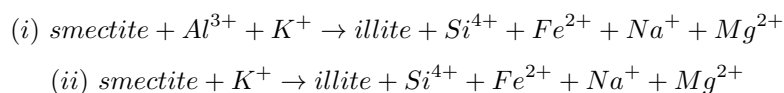
381 In our experiments, FORC measurements were carried out in cubic samples ($\approx 2cm^3$). For
 382 each sample, the routine involved acquiring 300 first-order reversal curves (N-FORCs) using
 383 the following parameters: (i) a discrete field sweep mode; (ii) an averaging time of 0.5 s;
 384 (iii) pauses of 1s at the saturation, calibration, and reversal fields; (iv) $B_{cmin} = 0$ mT and
 385 $B_{cmax} = 150$ mT; $B_{u_{min}} = -80$ mT and $B_{c_{max}} = +80$ mT; and a saturation field of 400 mT.
 386 Data were acquired in triplicates and further linearly combined to enhance signal/noise
 387 ratios, and finally processed through a Python-based statistical machine learning package
 388 (FORCsensei, Heslop (2020)). Preprocessing involved corrections of saturation slope (at
 389 70%), drift measurements, and normalisation by mass. Even after stacking the data, its
 390 noisy nature requires a considerable amount of smoothing. For that, it was also assumed a
 391 symmetrical vertical and horizontal smoothing, limiting the maximum smoothing factor to
 392 5.

393 Finally, Lowrie (1990)'s test was also carried out on representative samples by imparting
 394 three orthogonal IRM (through a 2G pulse magnetic field inducer, with distinct field in-
 395 tensities of 1.2T, 0.4T, and 0.12T) and further thermally demagnetising (100-700°C) the
 396 samples to estimate unblocking temperatures of the hard (1.2-0.4T), medium (0.4-0.12T)
 397 and soft ($< 0.12T$) magnetic carriers. The remaining remanence after each demagnetising
 398 step was measured.

3.2 X-ray diffractometry and crystallinity index

Authigenic growth of ferromagnetic phases due to smectite-illite transformations is among the common phenomena summoned for carbonate remagnetisation. As discussed by Huggett (2005), the illitisation of smectites vs depth is the most studied aspect of clay diagenesis. Smectites are a group of phyllosilicates (Kloprogge et al., 1999), which consist of layers of two-dimensional “sheets” formed by planes of oxygen atoms coordinated to Si, Al, Mg, and Fe. These minerals have a 2:1 structure layer, formed by two tetrahedral sheets with a single bound (on each side) of an octahedral sheet.

Illites are a clay mineral class that has non-expandable layers (Brigatti et al., 2013), being a common phyllosilicate. The illitisation of smectites, which starts around 70° and peaks around 120/130° (although the geothermal gradients of a basin might lead to earlier reactions), occurs if K^+ is available, following either of two reactions (Huggett, 2005):



K-feldspar dissolution is the main source of K^+ inputs. The second (ii) reaction preserves aluminium but requires a partial dissolution of the smectites. These processes represent a continuous transformation that results in mixed layers of smectite-illite (I-Sm), in a way that illite is randomly interstratified between the expandable layers when the transformation is at the earlier stages of the reaction (Lanson et al., 2009). Because one of the possible mechanisms related to the growth of authigenic magnetite is a conversion of Fe-rich smectite to illite, selected samples were submitted to X-ray diffractometry (XRD) to identify their solid phases (especially to verify the presence of clay minerals). The selection criteria were to select the samples that showed, simultaneously: (i) the highest magnetic susceptibility, (ii) paramagnetic contribution to hysteresis larger than 80% (iii) a considerable loss in magnetic susceptibility for higher frequencies (greater than 10%).

Samples were manually crushed with agate mortar and pistil, then settled in a section to be further analysed in a Bruker diffractometer, from 2 to 99° with step sizes of 0.02° (2θ) using a copper source radiation (25 mA, 40 kV). Sequentially, the raw data were treated using the software HighScore Plus (Malvern Panalytical) by stripping any K-Alpha2 Å contributions and quintic smoothing the product. Peaks were identified and matched to the solid phases by analysing both their position and their lattice spacing (d-spacing).

The series of crystalline arrangements and the progressive transformation of smectite to illite is a temperature-dependent process, so the crystallinity of illite increases with temperature increase. A common way to access palaeotemperatures in illite-bearing sedimentary rocks is to use the Kübler index (KI, (Kübler, 1964, 1967, 1968, 1990)). To calculate KI, the clay fraction ($< 2\mu m$) of the sedimentary rock is separated, and XRD data is collected using a $CuK\alpha$ radiation source, and the full width at half maximum (FWHM) of the 10° peak is calculated. This index is used to separate late-diagenetic (towards anchizone, very low grade/incipient metamorphism) and epizone (low greenschist facies), in a way that the smaller KI the higher the palaeotemperature (Jaboyedoff et al., 2001). XRD data of the remagnetised units in our work were further investigated to use the KI as a constraint for possible exposure to low-grade metamorphic conditions.

Powder samples were individually submitted to a weak acid solution (acetic acid 2 M + sodium acetate 1M [4:1], pH \approx 4, as Strehlau et al. (2014)) in a Becker flask, and stirred at 40°C for an hour. After neutralising the solution, the thin fraction was separated through a decantation process, and the supernatant was transferred to a plate, so the clay minerals could settle as they dried. Platy clay minerals tend to orient themselves parallel to the glass slide during settling, which enhances the peak intensities of basal planes (Tohver et al., 2008). Finally, samples were submitted to sequential XRD acquisition procedure:

446 (i) ordinary data acquisition after drying the clay fraction, (ii) XRD after ethylene glycol
 447 impregnation, and (iii) after calcination at 550°C. Background removal was performed by
 448 adjusting a forward model, either with linear or logarithmic decaying curves to better de-
 449 scribe the spectrum. Calculation of KI values was performed by optimising the parameters
 450 of a Gaussian distribution through a non-linear least squares fitting (Gauss-Newton method,
 451 Aster et al. (2013)) in a Python environment.

452 3.3 Micro-to-nanosopic imaging/chemical analysis

453 Using the same criteria as those for XRD, thin sections of four samples were produced to
 454 perform an overall microscale analysis of their petrographic features (under natural and po-
 455 larised light). Microscopic imaging was performed on the same thin sections (after carbon
 456 plating) study on the petrographic analysis. An electronic microscope (HELIOS 5 PFIB
 457 CXE DUALBEAM) is used to achieve visual analysis (on the secondary electrons, SE-mode)
 458 and to accomplish chemical mapping of microscopic regions through energy dispersive spec-
 459 troscopy (EDS). Since the major interest is in the thin magnetic carriers of stable remanence,
 460 this section focuses on finding PSD-range iron oxides/sulphides in the remagnetised units,
 461 and their spatial correlation with other mineral constituents.

462 Synchrotron radiation is a powerful electromagnetic wave (Yamashita, 2003) and an im-
 463 portant X-ray source that can help to understand the physical properties of materials at
 464 a nanoscopic scale, providing also (Duncan, 2018): a chemical profile with incomparable
 465 resolution, and measurements of geometric structures to thousands of nanometers with el-
 466 emental sensitivity. For geological samples, it has potential use in matters such as X-ray
 467 absorption spectroscopy, X-ray diffraction, and X-ray fluorescence (Henderson et al., 1995).
 468 Since X-rays are ionising radiation, they can absorb energy and eject core electrons from
 469 atoms. Scanning the X-ray through a specific binding energy results in the detection of
 470 an abrupt increase in absorption (called rising absorption edge, sometimes preceded by a
 471 brief increase in absorption that is called a pre-edge), which will be specific to a determined
 472 core-electron binding energy (and therefore specific to an element) and named according to
 473 the quantum number of the excited electron (Penner-Hahn, 2003). X-ray absorption spec-
 474 troscopy (XAS) comprises two segments: X-ray absorption near-edge structure (XANES),
 475 and ii) extended X-ray absorption fine structure. While EXAFS studies are more commonly
 476 applied to amorphous/unstructured materials providing information on the electronic struc-
 477 ture of specific sites within materials, XANES gives relatively straightforward information
 478 about the oxidation state of the central absorbing atom (Ormerod, 2001). Besides, XANES
 479 is also sensitive to local coordination, chemical composition, and crystal structure (Zhu et
 480 al., 2021).

481 Since most studies of carbonate rocks are characterised by bulk measurements (mainly due
 482 to the low content of iron oxides and their nanoscopic size), this work explores synchrotron
 483 radiation for both XRF and XAS analysis to achieve in-situ high-sensitive characterisation
 484 of remagnetised samples (Sete Lagoas, Salitre, and Guia Formations). Because no significant
 485 magnetic distinction between GC and GT is observed, the following analyses were performed
 486 on a GC sample. Experiments were conducted in a Coherent X-ray Nanoprobe Beamline
 487 (CARNAÚBA, Oliveira et al. (2014)), at the Brazilian Synchrotron Facility (SIRIUS, Figure
 488 4a) which yields a spectroscopic range of 2.05 to 15 keV energy (Tolentino, 2017). Data was
 489 acquired through an environmental in-air nanoprobe (tender-to-hard X-ray for sub-micro
 490 analysis, TARUMÁ, Figure 4b), where the thin sections were positioned (Figure 4c) to
 491 adjust the beam to selected regions (around 2 mm²). The samples are then raster-scanned
 492 to obtain two-dimensional data (Tolentino, 2021).

493 For XRF data, Gaussian distributions were adjusted to the log of peak intensity (y) vs
 494 energy (E), using mean distribution values μ to obtain a qualitative concentration of this
 495 element within an area. XAS data was collected in fluorescence mode around the Fe K-edge
 496 (activation energy, $E_0 \approx 7112$ eV), using metallic Fe-foils to calibrate the monochromator,

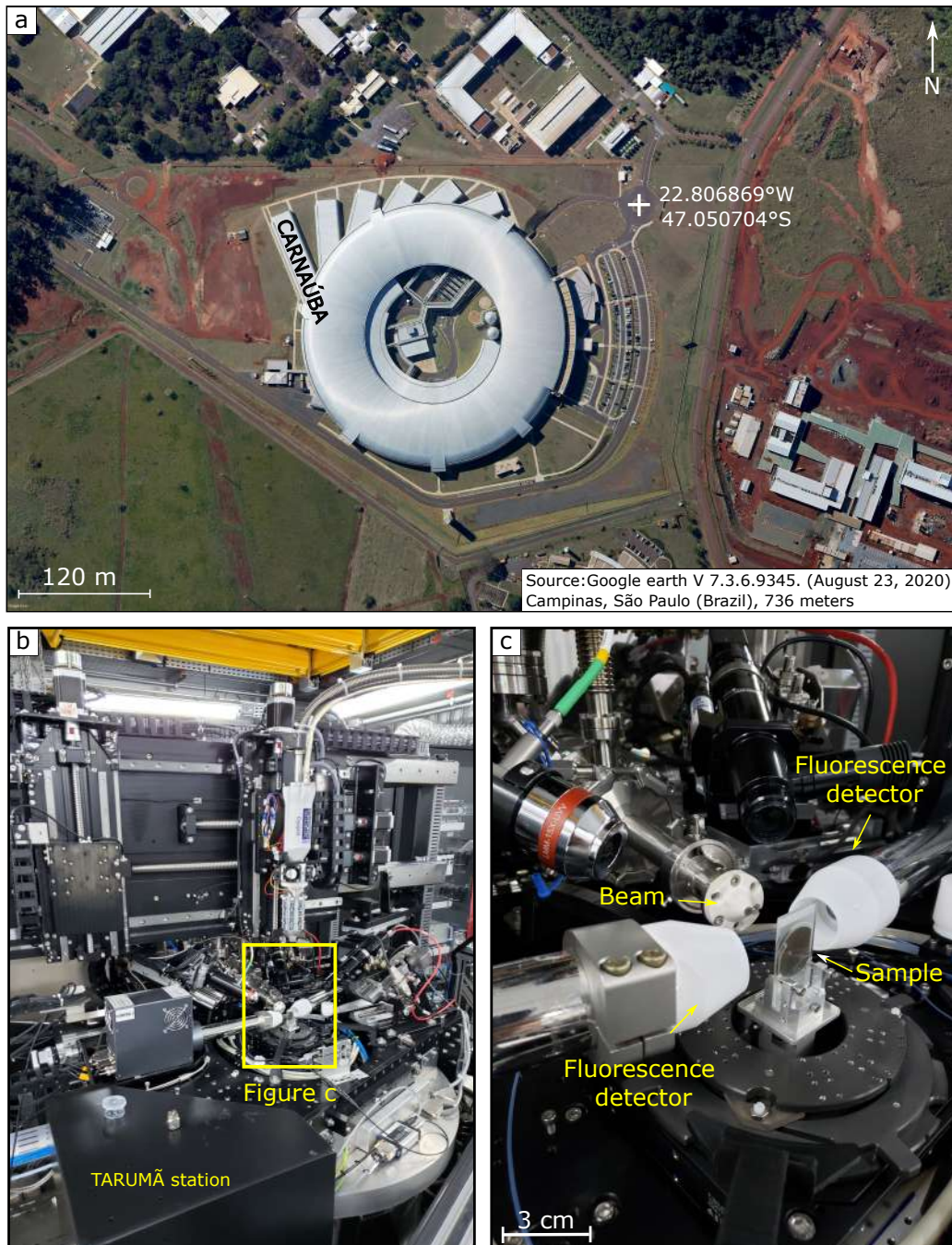


Figure 4. Experimental setup for highly detailed XRF and XAS analysis. a) SIRIUS, the Brazilian Synchrotron facility, and the CARNAÚBA beamline. (c) the TARUMÃ station (at the CARNAÚBA beamline), and focus on the sample holder region (b), showing fluorescence detectors and the position of the incoming synchrotron radiation beam.

497 performing three sequential scans in each sample to optimise the signal/noise ratio. The nor-
 498 malisation procedure applied in this work is similar to those applied in specialised software
 499 (Ravel & Newville, 2005). XAS data of αFe_2O_3 , γFe_2O_3 and Fe_3O_4 were compiled from
 500 Piquet et al. (2014), while FeS_2 data was retrieved from Ravel (2013), used as comparisons
 501 against our experiments.

502 3.4 Thermogravimetric analysis coupled to a Quadrupole Mass Spectrometer 503 (TGA-QMS)

504 To better correlate the presence of hydrocarbon and sulphur in samples of the Mirassol
 505 d'Oeste and Guia Formation (Check Figure 2e for clarity), thermogravimetric analysis cou-
 506 pled to a Quadrupole Mass Spectrometer (TGA-QMS) was performed under constant syn-
 507 thetic air flow (40m/min) on samples from the Guia Formation over the Amazon craton (GT)
 508 and its underlying bitumen-enriched dolostones from the Mirassol d'Oeste ($MO_{transition}$),
 509 as well as bitumen-poor samples from the dolostones immediately above the diamictites
 510 of the Puga formation (MO_{base}). We intend to understand the differences in the amount
 511 of organic matter (CO_2) and sulphur content (SO_2 , SO_3), by checking the mass loss as
 512 temperature increases.

513 4 Results

514 4.1 Rock magnetism

515 4.1.1 Frequency dependent magnetic susceptibility

516 Samples from the three studied basins showed magnetic susceptibility loss from low to high
 517 frequencies. The displacement in the susceptibility distribution is better observed in the
 518 respective boxplots of each group (Figure 5). The calculated large χ_{FD} values for most of
 519 the samples are considerably large, although some of them (mostly for the Irecê samples,
 520 IR) are below 5% (Figure 5h). Samples from the Araras Group had the most expressive loss
 521 of susceptibility, which is evident in the χ_{FN} values of Guia Formation (Figure 5i,j).

522 Two GT and GC samples have shown extreme values of susceptibility loss (Figure 5i,j).
 523 Because χ_{FN} and χ_{ON} parameters should be equivalent, we would have expected a linear
 524 trend. Such anomalous responses in GT and GC samples are present in distinct frequencies
 525 since they show a linear tendency when comparing χ_{FN} and χ_{ON} parameters. As discussed
 526 by Hrouda et al. (2013), diamagnetic materials, such as calcite, tend to increase δ_{LF} and
 527 result in large χ_{ON} values. Yet, χ_{FN} and χ_{ON} values are coherent, so linear regression
 528 through least squares fit for all the groups shows determination coefficients $R^2 > 0.79$. The
 529 higher dispersion, observed when comparing χ_{FN} and χ_{ON} for the Irecê (IR) samples is more
 530 evident, which could be the result of paramagnetic phases decreasing δ_{LF} or susceptibility
 531 measurements that are close to the minimum experimental.

532 Remagnetised carbonate rocks usually show χ_{FD} greater than 5% (Font et al., 2006; Jackson
 533 & Sun, 1992), and such has been interpreted as a result of an important contribution of
 534 superparamagnetic grains. χ_{FN} values of remagnetised units indeed show an important
 535 loss of magnetic susceptibility. However, the Mirassol d'Oeste basal samples (which are
 536 our control test) yield a considerable loss of susceptibility (> 5%), showing a comparable
 537 behaviour to the IR samples.

538 4.1.2 ARMs, Magnetic hysteresis and backfield curves parameters

539 Apart from a few samples, the general behaviour of ARM curves (*Supplementary file*,
 540 Figure S1) is coherent within the same unit. Some samples of the Bambuí and Irecê units
 541 seem to be far from reaching saturation at 100 mT. In Bambuí samples, the slope of mag-
 542 netisation curves is shallower compared to those of Irecê, indicating the presence of more

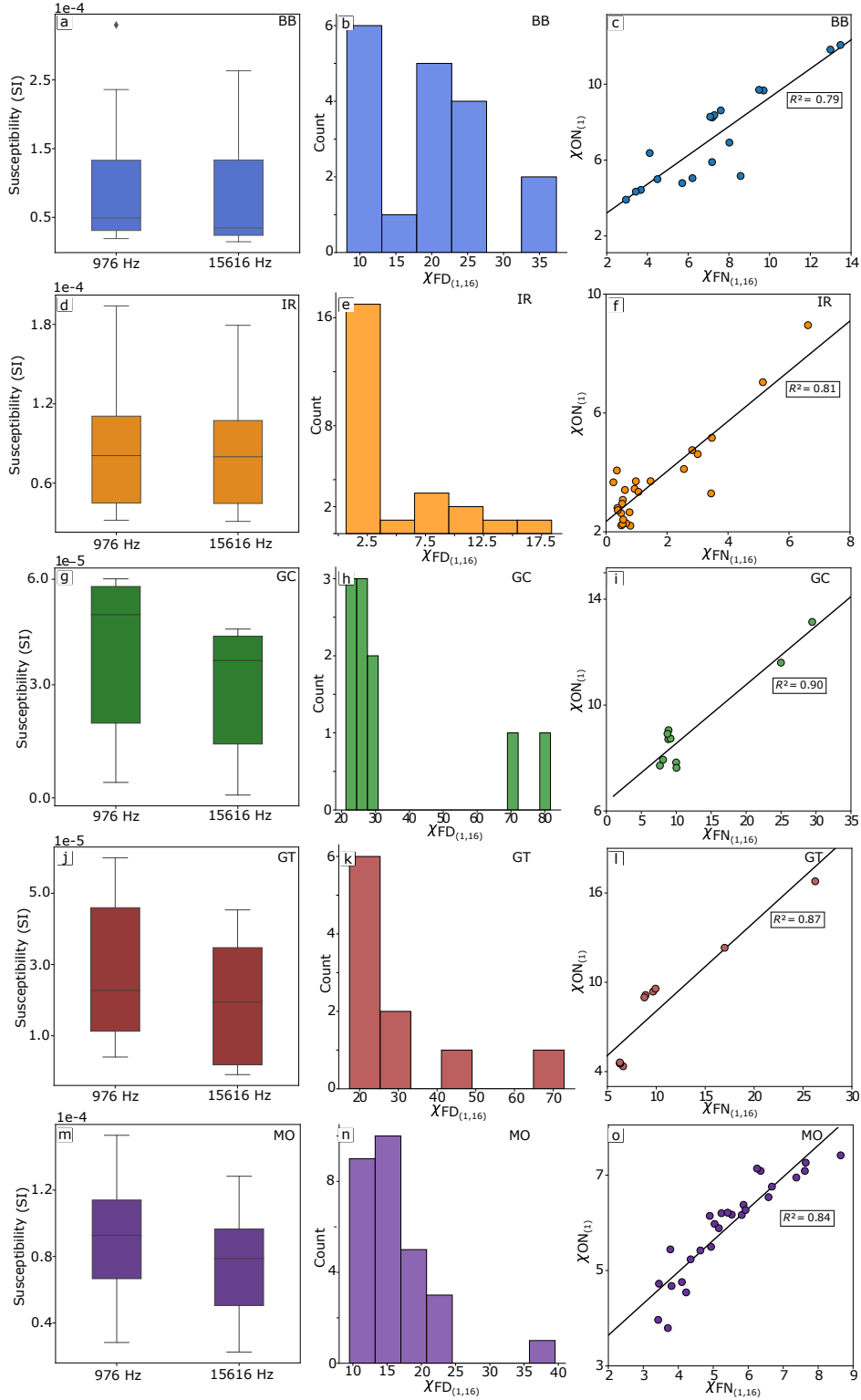


Figure 5. Frequency-dependent magnetic susceptibility of samples from the Bambuí (BB) and Irecê basin (IR), as well as from the Araras group: Guia Formation (GC, GC) and Mirassol d'Oeste formation (MO). χ_{FD} , χ_{FN} and χ_{ON} follow Eq. 1, Eq. 2, and Eq. 3, respectively. The subscript number in front of the susceptibility parameters indicates an approximation of the experimental frequencies in kHz. Diamonds are outliers in the boxplot distribution.

543 coercive phases in the second ones. However, another behaviour can also be observed in
 544 other samples from the same units, which are very similar to those of the Guia Formation,
 545 where most of the magnetisation is acquired up to 70 mT. In the Araras Group, samples
 546 from Guia Formation and Mirassol d'Oeste seem near to reaching saturation at 100 mT.
 547 Regardless, the slope of Mirassol d'Oeste samples is steeper, indicating a larger contribution
 548 of low coercivity minerals. The gradient of the ARMs acquisition curves of all units shows
 549 that most of the magnetisation is achieved at coercivities below 20 mT, which could be
 550 typically explained by the presence of magnetite. Coincidentally, these samples (BB, IR,
 551 GC, and GT) also show coincident peaks of coercivity around 40 mT, which is absent in
 552 the dolomites of the Mirassol d'Oeste Formation. Such behaviour could be related to the
 553 significant presence of more than one remanence-bearing mineral in the remagnetised units.

554 The uncorrected hysteresis analysis reveals a significant involvement of paramagnetic ma-
 555 terials in the examined samples (Figure 6 b, c, d, and e). This is evident, with over 75%
 556 of the samples demonstrating a paramagnetic contribution of approximately 80% at the
 557 maximum applied field. Furthermore, upon analysing the gradient of an irreversible loop,
 558 the presence of a linear component in magnetisation (attributed to the paramagnetic com-
 559 ponent) is observed, resulting in a positive basal displacement of the gradients ((U. Bellon
 560 et al., 2023)). Notably, this paramagnetic contribution can entirely surpass the ferromag-
 561 netic contribution, reaching values as high as 99% of the sample saturation magnetisation
 562 in some instances. This is an important observation because it points towards a signifi-
 563 cant input of iron-bearing silicates in these carbonate rocks. Some examples of minerals
 564 associated with paramagnetic behaviour that could be accessory phases in carbonates are
 565 kaolinite ($Al_2(Si_2O_5)(OH)_4$), a silicate that might have small amounts of transitional el-
 566 ements, such as Fe, Mn, and V which might lead to paramagnetic behaviour (Schreiner,
 567 2002); chlorites (Mg, Al, Fe)₁₂[(*Si, Al*)₈O₂₀](OH)₁₆ (Martín-Hernández & Hirt, 2003), a
 568 group of micaceous phyllosilicates; and more interestingly, Fe-rich smectites (Callaway &
 569 McAtee, 1985) and (iii) illites (Potter et al., 2004).

570 When corrected from the paramagnetic/diamagnetic contribution, distorted hysteresis loops
 571 are more clearly observed for the remagnetised carbonates. Saturation is not achieved in
 572 fields below 100 mT for most of the samples. Bambuí samples have commonly a wasp-waisted
 573 (constricted middles) hysteresis loop (Figure 6b), which is indicative of mixing populations
 574 of magnetic carriers with very distinct coercivities, or the combination of superparamagnetic
 575 and single domain behaviours in the same sample (Tauxe et al., 1996). Hysteresis from Irecê
 576 samples, however, look more like potbellies (wider middles and curved shoulders, Figure
 577 6c). While this behaviour is more common in magnetic assemblages where the population
 578 of SP grains is $< 30nm$, wasp-waisted hysteresis caused by a mixture with SP grains is not
 579 common to thresholds smaller than 8 nm (Tauxe et al., 1996). Whereas the signature of the
 580 Bambuí samples is compatible with the presence of magnetite, coercivities as large as those
 581 in some of Irecê samples indicate the presence of minerals with larger coercivities but are not
 582 excluded, however, the presence of magnetite as well. Samples from the Guia (Figure 6d)
 583 and Mirassol d'Oeste (Figure 6e) formations have similar magnetic hysteresis but distorted
 584 loops frequently appear for the Guia samples. There is no significant difference between
 585 the deformed and undeformed terranes (GC and GT samples, respectively). Potbellies are
 586 absent in this group, but wasp-waisted hysteresis frequently occurs.

587 One of the ways to interpret the results of magnetic hysteresis and backfield data as bulk
 588 indicative of the magnetic domain state. As there are other methodologies to infer domain
 589 state (as FORC diagrams, which will be further discussed), remagnetised carbonates are
 590 known to follow a trend in Day plot (Day et al., 1977). Therefore, we still believe it is a
 591 valid discussion comparing our signatures against these trends in such a diagram. Parry
 592 (1982), as discussed by (Jackson, 1990), showed that mixtures of PSD + MD or SD + MD
 593 magnetite follow a power law that relates magnetisation and coercivity as:

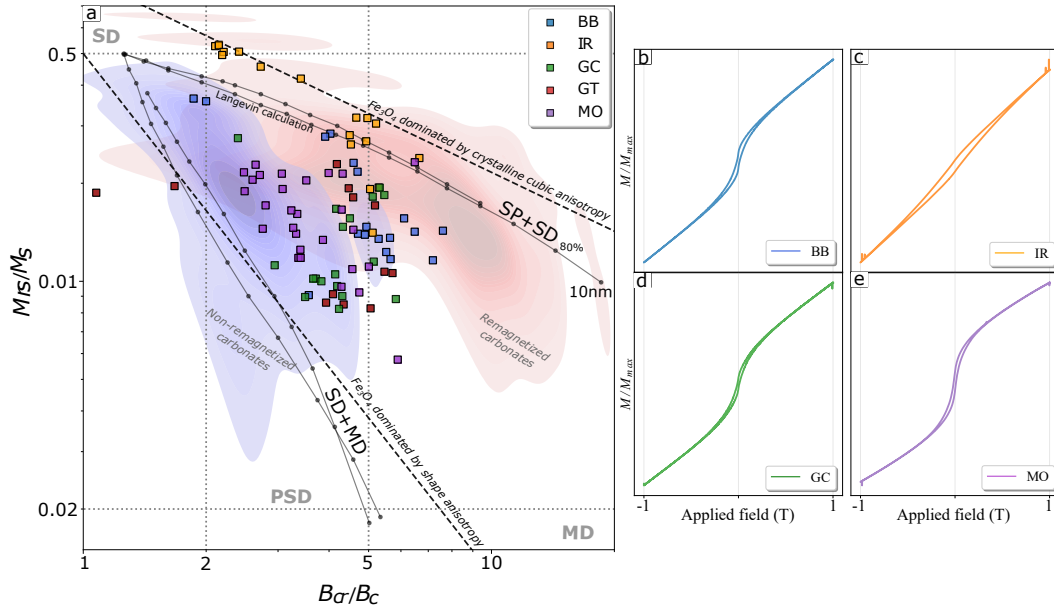


Figure 6. a) Bilogarithmic Day plot compiling data from magnetic hysteresis and backfield curves from the analysed samples. Solid black lines are the mixtures of multidomain (MD) + single-domain (SD), or a mixture between single domain (SD) and superparamagnetic population of magnetite (following Dunlop (2002)). Solid grey lines are the theoretical trends followed by a single-sized population of magnetite controlled by shape anisotropy (intercept at 0.5 in the M_r/M_s -axis) and controlled by crystalline cubic anisotropy (intercept at 0.89 in the M_r/M_s -axis) (Parry, 1982; Jackson, 1990). The blue and red contours represent density frequencies of non-remagnetised/remagnetised carbonates, respectively (data manually acquired from Jackson and Swanson-Hysell (2012)). Plots on the right are representative magnetic hysteresis of each studied unit. Remagnetised carbonates yielded distorted loops, for which Bambuí (b) and Guia samples (d) are mostly wasp-waisted and Irecê samples are potbellies (c). Mirassol d’Oeste samples (e) are ordinary low coercivity loops expected for magnetite-bearing rocks.

$$\frac{M_{rs}}{M_s} = c \cdot \left(\frac{B_{cr}}{B_c} \right)^m \quad (4)$$

594 If shape anisotropy is dominant in the particles that compose the sample, and if the particles
 595 are normally single-sized, the trend produced by Eq. 4 will follow a line defined by $c = 0.5$
 596 and $m = -1.6$ (Jackson, 1990; Parry, 1982). In the bilogarithmic Day plot of Jackson
 597 and Swanson-Hysell (2012), when the Bcr/Bc ratio approaches unity, the trend related to
 598 remagnetised Appalachian carbonates reaches a shallower slope $m = -0.6$ and a higher
 599 intercept ($c = 0.86$). Such a ratio coincides with the expected magnetocrystalline cubic
 600 anisotropy of SD particles (Wohlfarth & Tonge, 1957). However, as previously discussed,
 601 the hypothesis of magnetocrystalline cubic anisotropy being responsible for the abnormal
 602 hysteresis ratios originates directly from the intercept value of the power law-trend-line
 603 in the Day plot. Therefore, a stronger influence of particles dominated by magnetocrystalline
 604 anisotropy could not necessarily be a fingerprint of remagnetised carbonate rocks (as
 605 discussed by Jackson and Swanson-Hysell (2012)). Samples from the Bambuí group and
 606 Araras group mostly plot far from the single-sized shape-controlled anisotropy but do not
 607 follow the North American carbonate trend as well (Figure 6a), which is considered to be a
 608 “false negative” to magnetic fingerprinting, in other words: samples are palaeomagnetically
 609 remagnetised but their bulk hysteresis properties do not follow the expected fingerprint.
 610 Most of the Irecê samples, in turn, plot right under this trend and seem to follow a trend.

611 Domain states have a size/shape-constrain dependence. Superparamagnetic threshold (d_s)
 612 and the critical single-domain size (d_0) vary for different materials and even change de-
 613 pending on the shape of the same material (Butler & Banerjee, 1975). For equidimensional
 614 grains, at 20°C, of (i) magnetite, d_s are usually between 0.025 and 0.030 μm and $d_0 =$
 615 0.05- 0.06 μm ; (ii) for haematite, d_s are similar to those in magnetite, but d_0 might reach
 616 dimensions of up to 15 μm , while (iii) pyrrhotite have a critical single domain size at 1.6
 617 μm (Dunlop & Özdemir, 1997). Most of the magnetic particles in rocks are, however, not
 618 entirely described by MD or SD theory, exhibiting a non-uniform magnetic state classified
 619 as PSD (Nagy, 2017). Most of the analysed data fall within the PSD field, although some
 620 of them could be explained by the non-linear mixing theory from (Dunlop, 2002), especially
 621 the samples from the Mirassol d’Oeste formation.

622 U. Bellon et al. (2023) employed an unmixing method to discern susceptibility components
 623 within distorted hysteresis loops from both the Salitre and Sete Lagoas Formations. De-
 624 spite the inherent limitations of any parametric unmixing method, which relies solely on the
 625 model’s capacity to explain a given phenomenon, the researchers demonstrated that pot-
 626 bellies and wasp-waisted features in BB and IR samples could arise without necessitating
 627 a substantial contribution from SP particles. Instead, these features were attributed to the
 628 presence of different coercivity components, corresponding to distinct minerals. Given that
 629 paleomagnetic data already indicate the presence of both monoclinic pyrrhotite and PSD
 630 magnetite in the remagnetised units, their alignment in the Day plot posed challenges in
 631 connecting them to their respective domain states. Nevertheless, it was noted that mixing
 632 scenarios involving SP + SD, PSD + SP, and similar combinations could generate a variety
 633 of distributions below the 0.5 M_{rs}/M_s threshold, as discussed by (Dunlop, 2002). Con-
 634 sequently, the mixture of distinct magnetic populations in remagnetised carbonates could
 635 exhibit considerable dispersion.

636 4.1.3 FORC diagrams

637 Most of the Bambuí samples (Figure 7a’) comprise an important contribution in the coerciv-
 638 ity axis (B_c), with little contribution to the interaction axis (B_u), typical of non-interactive
 639 SD particles (Roberts et al., 2000; Roberts, 2022). Central-ridge contribution is also com-
 640 monly related to the presence of biogenic magnetite, like magnetotactic bacterial magnetite
 641 in pelagic sediments (Roberts, 2011), whose sharpness is associated with little magnetostatic
 642 interactions. Ultrafine authigenic magnetic particles may also contribute to the central ridge

643 response, but this contribution depends on how dispersed the matrix of the particles is (Egli
 644 et al., 2010). Geiss et al. (2008) also argued that highly dispersed pedogenic SD magnetite
 645 contributed to a lack of magnetostatic interactions. The centre of the distribution in (Fig-
 646 ure 7a') is near the origin of Bc and spreads towards higher field values, which probably
 647 suggests the presence of an assemblage of particles with a variety of coercivities. This could
 648 be explained by a range of SD/vortex-state particles of magnetite and pyrrhotite sparsely
 649 distributed within the carbonate matrix.

650 As previously shown by the hysteresis curves, Irecê samples contain a set of variable coer-
 651 civity ranges. For most of them, FORC diagrams are extremely noisy, even after linearly
 652 combining multiple stacks of the same samples. The FORC below resembles potbelly-like
 653 loops (Figure 7b). The effects of smoothing and artefacts generated through the processing
 654 are recognised as medium-intensity contributions far from both the central ridge and the
 655 origin of the Bu-axis (Figure 7b'). However, the main distribution is centred along the
 656 coercivity axis, which is similar to the Bambuí samples.

657 Guia Formation samples from both Tangará and Cáceres regions bear very similar hystere-
 658 sis/backfield parameters. As expected, FORC diagrams also show no clear signs of magnetic
 659 differentiation of both terranes. The main response is usually asymmetric, with distribu-
 660 tions centred in the Bc-axis, with small spreading towards the interaction axis, a product
 661 attributed to the PSD state. Increasing grain size within the PSD threshold results in a
 662 decrease of coercivity and in progressive diverging towards the Bu-origin and becoming more
 663 MD-like (Roberts et al., 2000, 2014). However, some samples have only a major distribution
 664 along the coercivity axis, similar to what is observed in the Bambuí-samples. Very few sam-
 665 ples of the Guia Formation (both from Tangará and Cáceres regions) showed an important
 666 diamagnetic contribution, since the majority of them bear an important amount of clays.
 667 Even in these samples, the ferromagnetic contribution is distinguishable (Figure 7c), but
 668 diamagnetic correction results in diagonal positive/negative intercalation of artefacts (Fig-
 669 ure 7c'). Nevertheless, the major contribution to the coercivity axis is visible, a probable
 670 result of non-interactive single-domain grains.

671 FORC diagrams of the non-remagnetised unit of the Araras Group (Mirassol d'Oeste) often
 672 show a PSD-like behaviour, which is similar to the major response of the Guia Formation
 673 samples, and diagonal artefacts might appear as a response from paramagnetic corrections.
 674 However, a few of them show (besides the PSD behaviour), an important contribution in
 675 the Bu-axis near the origin, indicating that MD particles might be contributing to their
 676 spectrum as well (Figure 7d').

677 In a broad context, the remagnetised carbonates under investigation exhibit similar fea-
 678 tures in their FORC diagrams. The prominent central ridge not only strongly suggests the
 679 presence of stable SD/PSD grains across varying grain sizes but also hints at the potential
 680 existence of superparamagnetic grains, as indicated by the eventual extension towards zero
 681 along the Bc-axis. While FORC diagrams serve as invaluable tools, it's important to note
 682 that they represent the response of the entire assembly of ferromagnetic particles within
 683 the rocks. In cases involving samples with magnetic mixtures, discerning the individual
 684 contributions of each component to the overall spectrum poses a challenging task. While
 685 procedures for unmixing FORC components are available in the literature (Harrison et al.,
 686 2018), their effective application necessitates well-defined assemblages, a characteristic not
 687 commonly observed in these remagnetised carbonates.

688 *4.1.4 Lowrie test*

689 For the Lowrie test (Figure 8), medium and hard-coercivity components of the BB-2 (Figure
 690 8a) sample show blocking temperatures near 350°C and a residual (intensity $< 10\%$) com-
 691 ponent that is completely decayed at 450°C , which is indicative of the presence of pyrrhotite
 692 and a smaller amount of magnetite, while the soft fraction smoothly decays up to 550°C
 693 (typical of MD-magnetite). In a few other samples (e.g., BB-16, Figure 8b), pyrrhotite seems

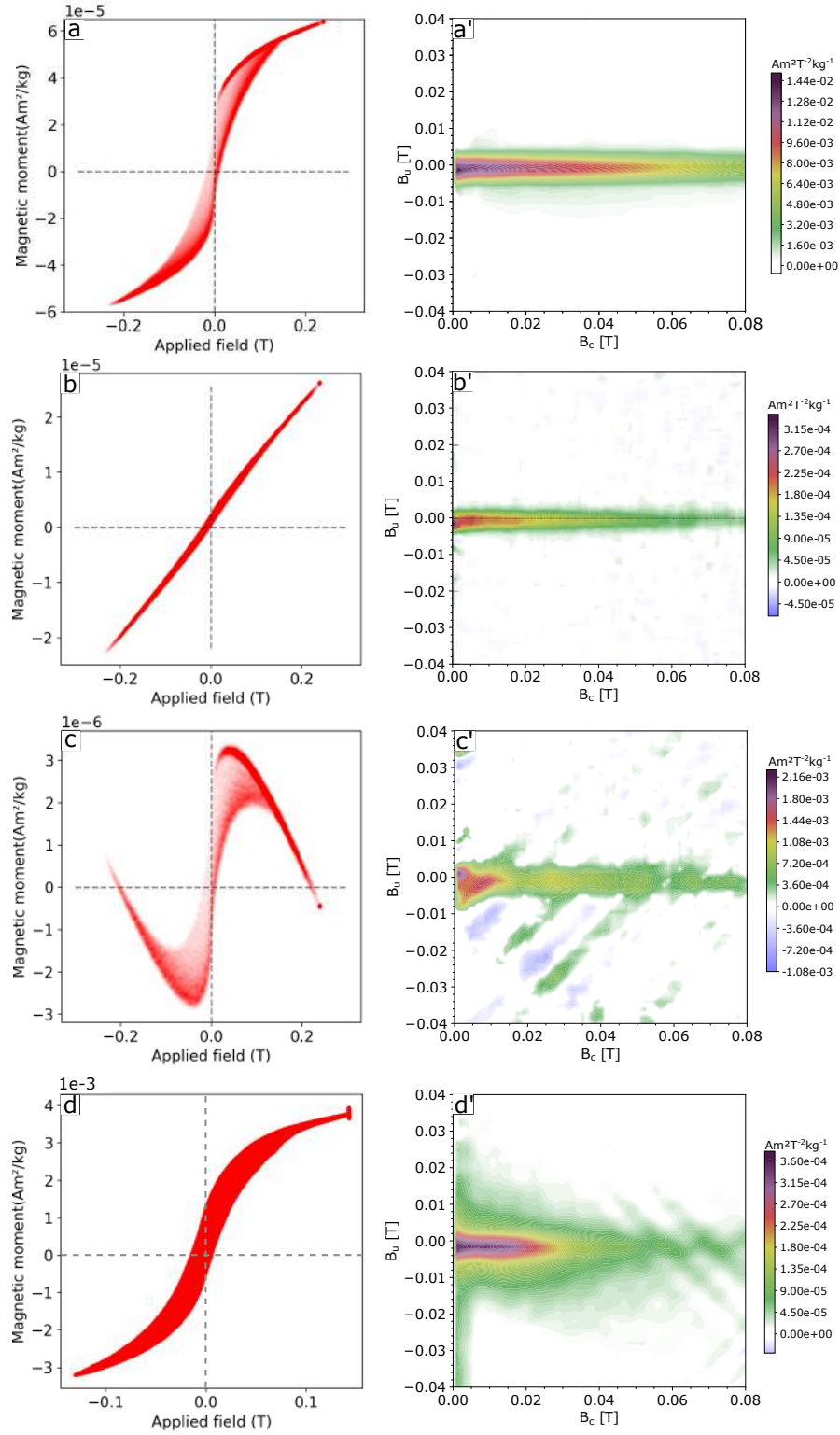


Figure 7. First-order reversal curves (FORC) of representative samples of both remagnetised (a,b, and c) units and non-remagnetised units (d). These FORCs are linear combinations (stacks) of sequential acquisition, to improve the signal/noise ratio. The respective FORC diagrams (a',b',c' and d') were processed through the FORCsensei package and optimised to a smoothing factor of 5.

694 not to be present as the three components smoothly decay to zero between 500/550°C. Irecê
 695 samples that yielded magnetic hysteresis with coercivities larger than 100 mT showed all
 696 three components completely decaying at 700°C (indicative of haematite), with no hints of
 697 the presence of magnetite or pyrrhotite (e.g., IR-6, Figure 8d). These samples are, however,
 698 much less common than those with a coercivity of remanence smaller than 100 mT (e.g.,
 699 IR-11, Figure 8c), which have shown two components: one around 350°C (pyrrhotite) and
 700 another one that slowly completely demagnetises around 500°C (magnetite). The soft com-
 701 ponent of the IR-11 sample should also be associated with magnetite. These samples are
 702 more similar to the signatures observed in the Bambuí samples.

703 Sample GT-11 (Figure 8e) shows a slower decay of the hard component up to 250°C, from
 704 which the decay is steeper up to 350°C, further smoothly demagnetising until 550°C. In this
 705 case, the smaller decay temperatures could be associated with maghemite and/or pyrrhotite,
 706 while the higher blocking temperature (together with soft and medium components) repre-
 707 sents magnetite. For the GC-2 sample (Figure 8f), hard and medium components slowly
 708 decay to 400°C, but only completely demagnetise at 500°C (together with the soft com-
 709 ponent that linearly demagnetises up to such temperature). The latter behaviour is proba-
 710 bly related to maghemite/oxidised magnetite (lower blocking temperature) and magnetite
 711 (higher blocking temperature).

712 Medium and hard components of the MO-2 sample (Figure 8g) quickly decay right from
 713 100°C up to 150°C before linearly decreasing up to 580°C. That quick decay could indicate
 714 the presence of a higher coercivity mineral (such as goethite). Although there is a component
 715 of the soft fraction that demagnetises at 350°C (MO-2 sample, Figure 8c) it differs from
 716 Bambuí and Irecê samples in terms of coercivity (since in those the pyrrhotite component
 717 is held by medium and high coercivity components). Most of the samples are, however,
 718 dominated by magnetite, showing a behaviour more similar to those from the MO-22 sample
 719 (Figure 8h), with medium and hard components smoothly demagnetising until 580°C and
 720 a soft component linearly demagnetising up to 450°C, from which it slowly demagnetises
 721 up to 550°C.

722 The strong indication of the presence of magnetite and pyrrhotite in remagnetised samples
 723 comes from the thermal decomposition of their artificial remanence, as suggested in the
 724 bulk magnetic measurements. Additionally, the agreement between the Lowrie test and
 725 the previously published NRM demagnetisation data for these units (refer to Section 2)
 726 further supports this, where the stable B and C components are associated with monoclinic
 727 pyrrhotite and magnetite, respectively. However, the observed varied behaviours within
 728 the same units indicate compositional variability within the samples. This variability may
 729 explain the dispersion of magnetic ratios within the Day plot (see Figure 6). Moreover,
 730 the soft components linked to magnetite may also be associated with coarser grain sizes,
 731 potentially originating from a detrital source. This explanation could also be valid for
 732 samples containing haematite, as illustrated in Figure 8d.

733 4.2 XRD

734 Samples from the Bambuí (Figure 9a) are essentially composed of calcite, but the diffraction
 735 patterns also indicate the presence of quartz (SiO_2), chlorite, and possibly feldspars (both K-
 736 feldspar and plagioclase), and a minor presence of dolomite. The mineralogical composition
 737 of the analysed samples from the Irecê basin (Figure 9b) is very similar to the Bambuí.
 738 However, the presence of dolomite and K-feldspar is strongly marked. Data from the Guia
 739 Formation (Figure 9c) is different (in some aspects) depending on the different locations
 740 since most of the diffraction data from the Cáceres region is related to dolomite and from
 741 Tangará it is related to calcite. Samples from the lowermost stratum of the Araras Group,
 742 the Mirassol d'Oeste formation (Figure 9d), are almost monomineralic (in terms of major
 743 constituents) and composed of dolomite and calcite. The presence of chlorite, however,
 744 will be further investigated using ethylene glycol, since smectites have a similar d-spacing

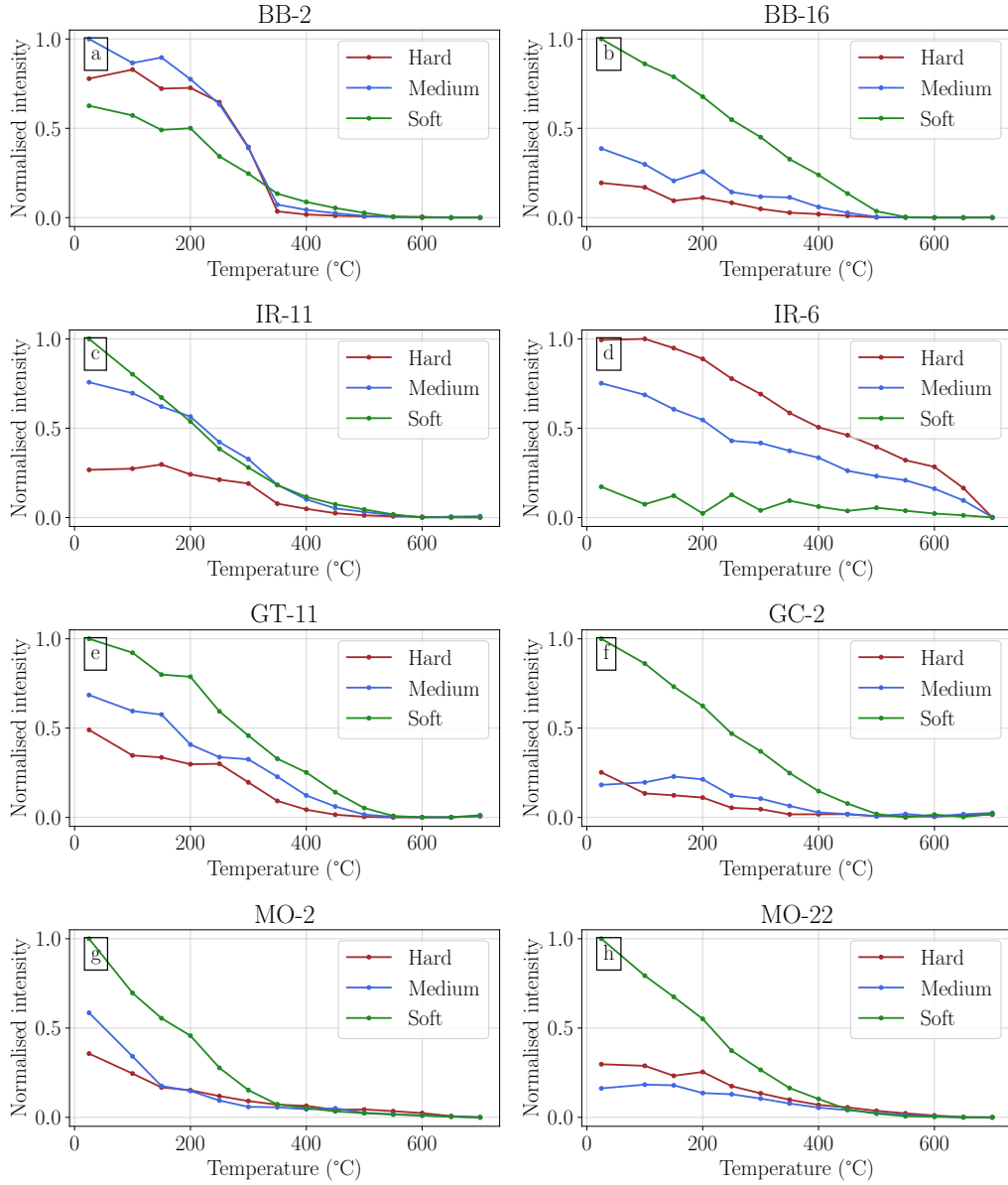


Figure 8. Lowrie (1990) test: an IRM is imparted in three orthogonal directions at three different intensities (1.2 T, 0.4 T, and 0.12 T), followed by thermal demagnetisation.

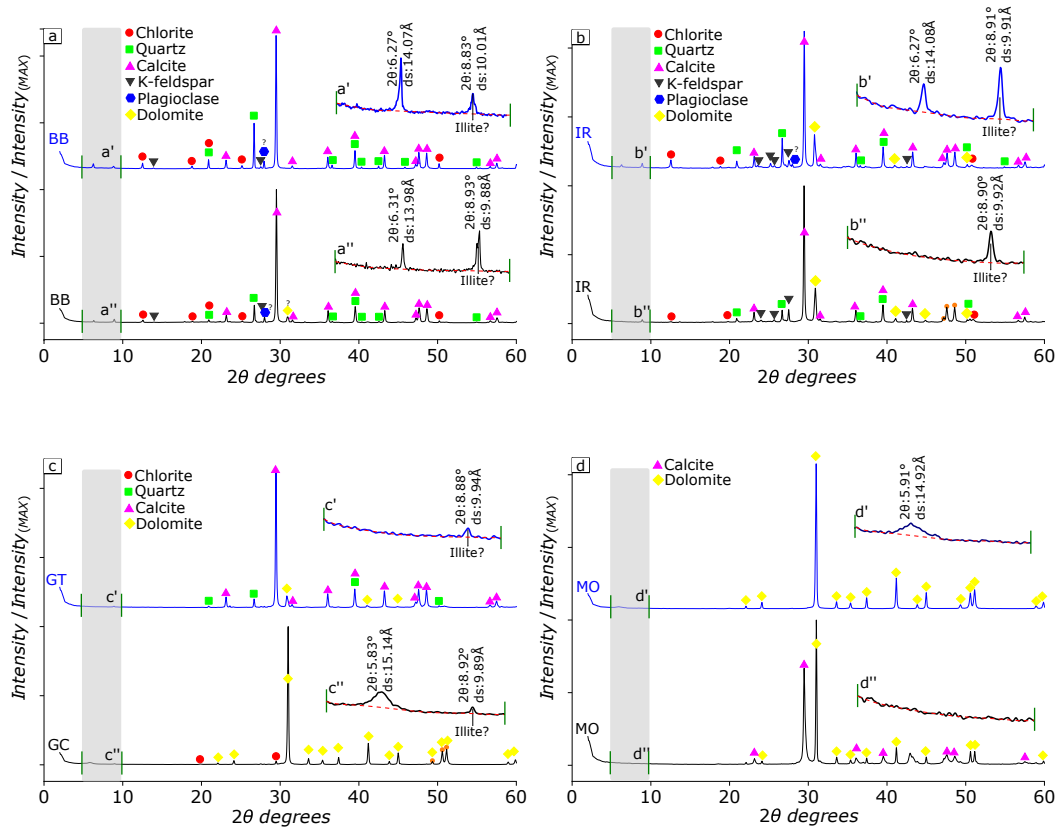


Figure 9. XRD diffractograms of samples from the Bambuí (a), Irecê (b), Guia (c), and Mirassol d'Oeste formation (d). Diffractograms are coloured following the sample names (two per unit). The shaded grey marks the expanded areas between 4 – 10° (2θ) shown in the upper right of each diffractogram (e.g., a' and a'' are the expanded areas for BB-6 and BB-12 samples, respectively) to highlight the occurrence or lack of the 10Å peak of illite around 8.9° (2θ).

745 (14Å) compared to chlorite, which might vary due to liquid-phase adsorption (9.6 – 21.4Å)
 746 (Tucker, 2001), and also because if illite is authigenic the transformation may not have been
 747 complete, and some residual smectite may remain (either isolated or intercalated with illite
 748 layers).

749 A common behaviour for Bambuí, Irecê, and Guia Formation samples is the occurrence of
 750 a peak around 8.9° (2θ). These peaks have a very small intensity compared to the major
 751 constituents of the samples but are distinct from the background signal (Figure 9). Lattice
 752 spacing values of such peaks are near 10Å, which is an indication of the presence of illite-like
 753 clay minerals (Patarachao, 2019; Tohver et al., 2006). Interestingly, none of the samples from
 754 the Mirassol d'Oeste formation showed the presence of such a peak, indicating its absence
 755 or only a trace amount concentration. Regarding remagnetisation due to clay diagenesis,
 756 Font et al. (2006) had already suggested that Guia limestones remagnetisation could have
 757 an important role in the formation of authigenic magnetite. Now, our data supports such
 758 observation by showing the lack of detectable amounts of illite in the Mirassol d'Oeste
 759 formation. Besides, the role of Fe-rich smectite-illite transformation and the growth of
 760 authigenic magnetite had not been discussed yet for the Bambuí and Irecê basins as well.

761 After separation of the clay fraction, both samples of the Sete Lagoas and Salitre Formation
 762 optimisation returned a good fitting of Gaussian curves within the peak signatures of illite

763 (≈ 9), yielding quite similar KI indexes of 0.14° and 0.13° (Figure 10a,b). These values
 764 indicate a high crystalline index, coherent with low greenschist metamorphic facies (epizone)
 765 (Mählmann & Frey, 2012). Although deformation is recognised in the borders of the Bambuí
 766 group as a consequence of the Araçuaí and Brasília belts (Moreira et al., 2020), the area
 767 from which samples studied here were collected are derived from the stable cratonic region
 768 (Chemale et al., 1993).

769 The results reported here indicate that even if the area was not disturbed tectonically, they
 770 could have been exposed to temperatures as high as 350° , which is the limit of the the
 771 epizone. These are conditions far apart from diagenetic environments, and if the correlation
 772 between remagnetisation and illite generation is confirmed, it indeed points to the remanence
 773 of Bambuí rocks as non-diagenetic. Smectite-illitisation requires not only temperature but
 774 an input of K^+ . The dissolution of K-feldspars in these rocks can serve as an in-situ
 775 potassium source for illitisation. However, hydrothermal percolating fluids can also work as
 776 triggers for illitisation. In the Salitre Formation, $\delta^{13}C$ and $\delta^{18}O$ data have been interpreted
 777 as indicatives of the percolation of external fluids of a hydrothermal nature (Couto, 2020).
 778 Ethylene glycol treatment for the BB sample induces a slight increase in the FWHM but
 779 causes a considerable displacement after calcinating at 550° (*Supplementary file*, Figure
 780 S2a). Ethylene glycol penetrates the interlayer spaces of smectite leading to the formation
 781 of a two-layer structure (Szczerba et al., 2014). This indicates that not very significant I-Sm
 782 structure persists in the Bambuí-sample. That is supported by a crystalline index, pointing
 783 out an ordered sequence mostly composed of illite layers (Lanson et al., 2009). For the IR
 784 sample, the illite peak suffers almost neglectful changes, indicating a purer illite content.
 785 Besides illite, XRD data (bulk samples) indicate peaks at 6.27° for the Sete Lagoas and
 786 Salitre Formations. If these were related to smectite, it would be contradictory to find such
 787 crystalline illites. However, none of their peaks (of BB and IR samples) swelled to 17 \AA
 788 when using ethylene glycol treatment, as would be expected if these peaks were attributed
 789 to smectite (Szczerba et al., 2014), instead, they are here interpreted as chlorite peaks.

790 For the Guia Formation, the results are distinct for the two terranes: those over the Amazon
 791 Craton (GT) yielded a KI value of 0.25° (Figure 10b), while the sample over the Paraguay
 792 belt (GC, Figure 10d) yielded a much higher index 0.11° . While GT samples indicate tran-
 793 sitional conditions from mid-to-high anchizone, representing incipient metamorphic condi-
 794 tions, GC is located at similar conditions to the Salitre and Sete Lagoas Formations. These
 795 results are coherent with illite crystalline indexes for the transitional region of the Amazon
 796 Craton to the Cáceres region (Alvarenga, 1990). The behaviour after ethylene glycol satu-
 797 ration for the GT illite peaks indicates an I-Sm structure (*Supplementary file*, Figure
 798 S2c) while the GC sample is more similar to Bambuí, suffering no considerable changes.
 799 Unfortunately, the previously observed 15.14 \AA peak (Figure 9c) was not further detected
 800 after carbonate dissolution.

801 Not only the presence of illite in all remagnetised units is a piece of important information
 802 for gathering a strongly based hypothesis for the process responsible for remagnetizing
 803 carbonate units throughout the west Gondwana, but its crystallinity also offers hints on
 804 the palaeotemperature conditions these rocks were submitted. Mainly because these rocks
 805 bear distinct magnetic minerals with statistically indistinguishable paleomagnetic directions,
 806 but because temperatures found in the anchi/epizone kinetically favour the formation of
 807 monoclinic pyrrhotite (present at the Salitre, Sete Lagoas and Guia Formation).

808 4.3 Microscopic data

809 4.3.1 Petrography

810 Petrographic observations in this study are used to support bulk characterisation of XRD
 811 data. They are specially important to select the regions where SEM-EDS and micro-
 812 XRF/XAS were further analysed.

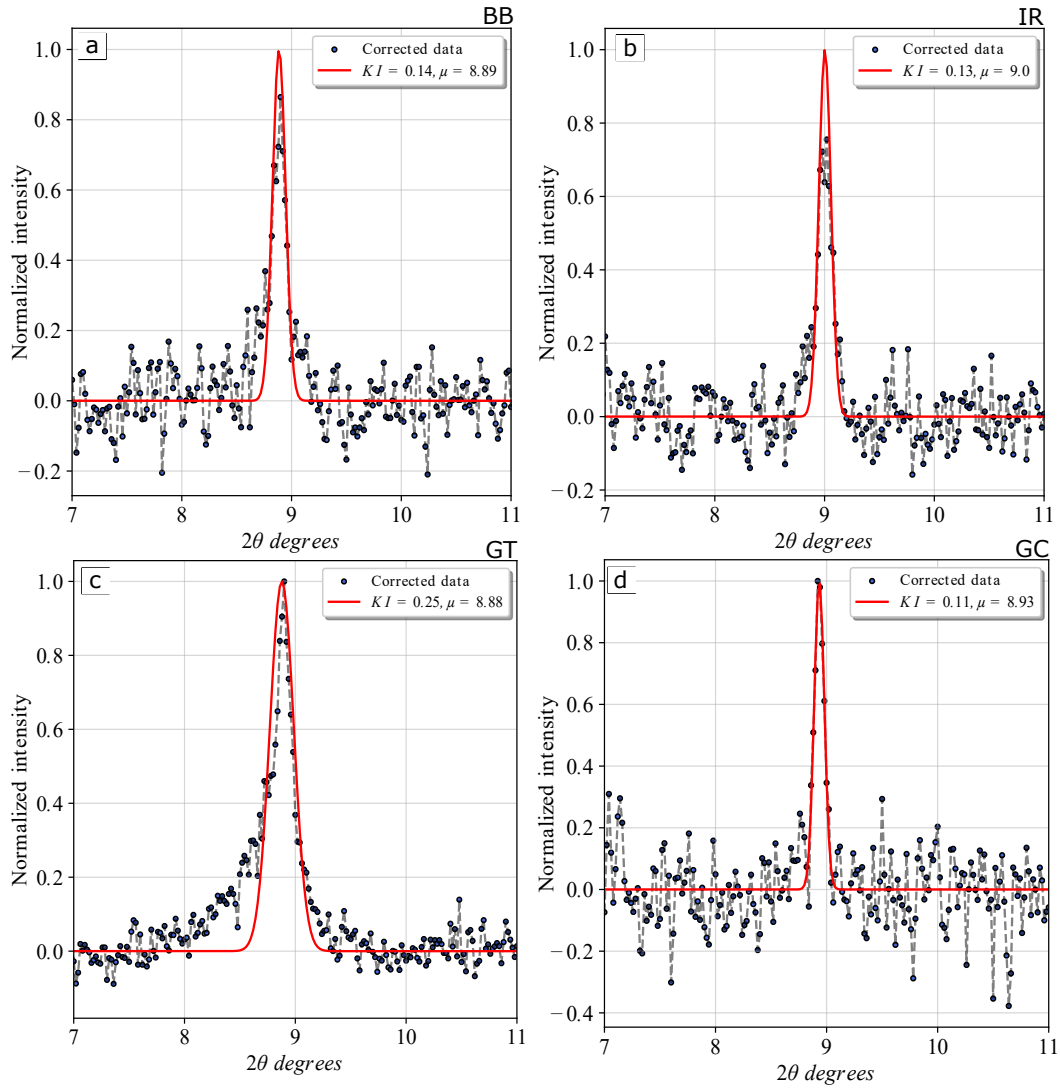


Figure 10. XRD experiments after carbonate dissolution of samples from Sete Lagoas (a), Salitre (b), and Guia Formations (c,d). Corrected data refers to XRD background subtraction. Fitting of Gaussian components at the illite peaks ($\approx 9^\circ$) was performed to sequentially calculate the Kübler index ($2\sqrt{2\ln 2} \cdot \sigma$), where σ is the dispersion around the mean.

813 Bambuí samples are essentially argillaceous micritic limestones (Figure 11a). There is no
 814 direct evidence of microfossil or bioturbation features. Embedded in the matrix, there is
 815 a considerable amount of clay minerals, whereas detrital grains include very thin particles
 816 (anhedral ones, $< 0.075\text{mm}$) of orthoclase and quartz. The latter, although rare, exhibits
 817 undulose extinction. Dolomite eventually appears as euhedral grains ($< 0.075\text{mm}$), which
 818 indicates localised dolomitisation. Calcite veins (0.1-0.25 mm of thickness) crosscut the mi-
 819 critic matrix (Figure 11b), showing discrete signs of border dissolution. Opaque minerals
 820 are mostly randomly distributed throughout the matrix, the subhedral grains varying in size
 821 from 0.05-0.075 mm and anhedral (more rounded ones) reaching up to 0.30 mm. However,
 822 thin ($< 0.1\text{mm}$) euhedral grains occur within calcite veins (sometimes recognised as mag-
 823 netite due to their characteristic cubic habit) which might indicate their contemporaneity.

824 Irecê samples are even more enriched in clay minerals, these differ from the Bambuí samples
 825 in the level of opacity, sometimes showing green/brownish colours (Figure 11c), possible
 826 evidence of their incipient chloritisation. They are argillaceous dolomitic limestones, with
 827 portions enriched in micrite and other portions enriched in intraclasts. These intraclasts
 828 are euhedral to subhedral grains of dolomite (0.1-0.15 mm) (Figure 11d), with interference
 829 colours distinct from the calcite forming the matrix. Although thin ($< 0.075\text{mm}$) subhedral
 830 grains occur, opaque more constantly appear as anhedral ($\approx 0.25\text{mm}$) particles, very often
 831 associated with clay minerals.

832 As previously discussed, Guia samples have suffered percolation of hydrocarbon fluids.
 833 These are observed as strips, irregularly percolating through the micritic matrix (Figure
 834 11e) in Cáceres samples (GC), whereas it follows the parallel planes in Tangará samples
 835 (GT). These limestones are also enriched in clay minerals, most mixed with micrite. Euhed-
 836 ral dolomite grains are, however, present in the samples as well (up to 0.1 mm). Anhedral
 837 grains of orthoclase (0.1-0.2 mm) and quartz (0.1-0.15) are found frequently in contact with
 838 hydrocarbon, both yielding strong undulose extinction. Opaque grains are widely spread
 839 through the matrix, more frequently euhedral in a cubic habit (0.05-0.1mm). Rocks from
 840 the Mirassol d'Oeste formation are dolomitic limestones, with a considerable amount of
 841 clay content (such as the remagnetised units described above). Large anhedral crystals of
 842 calcite (0.25-0.75mm) are randomly located in the matrix (Figure 11f), with no evidence
 843 to help understand whether they have grown during diagenesis or were deposited together
 844 with the matrix. Quartz grains also occur with a considerable frequency, with a range of
 845 sizes (0.1-0.50mm), marked by an undulose extinction. Anhedral opaque grains ($\approx 0.1\text{mm}$)
 846 are rarely present, with no clear association with other minerals in rock fabric.

847 Calcitic veins percolating the samples of the Bambuí are important evidence of the trans-
 848 port of fluids in a sin/post-cementation scenario. These fluids, either intrabasinal or al-
 849 lochthonous, could disturb local thermochemical stability and induce the transformation
 850 of iron-bearing minerals (which might explain the presence of opaque minerals within
 851 the veins). Regions of well-formed dolomite grains in the micritic matrix of Irecê sam-
 852 ples are a probable result of dolomitisation. Dolomitisation might occur in both solid
 853 (late-diagenetic/post-sedimentary) or untied limestones (early diagenetic/sin-sedimentary),
 854 achieved only by the presence of a solvent adding Mg-ions to the rock (Haldar & Tišljár,
 855 2014). As most of the rock is dominated by micrite, the dolomites in the Irecê are probably
 856 a result of a post-sedimentary fluid percolation.

857 These pieces of evidence of fluid percolation are important for considering the illitisation
 858 of smectite as a central hypothesis in the remagnetisation of these carbonates. Firstly,
 859 because micropetrographic observation confirms an important presence of clay minerals
 860 within the matrix of these carbonates, and secondly, because illitisation itself requires an
 861 input of K^+ that could be carried by it. Detrital feldspar is in thermodynamic disequilibrium
 862 with meteoric waters, undergoing thorough dissolution processes in all diagenetic regimes,
 863 including when entering in contact with acid waters charged with CO_2 , or organic acids
 864 derived from biodegradation of oil (Morad, 1978). Nevertheless, the same is relevant for
 865 the samples of Guia formation, where hydrocarbon percolates through the rock. Although

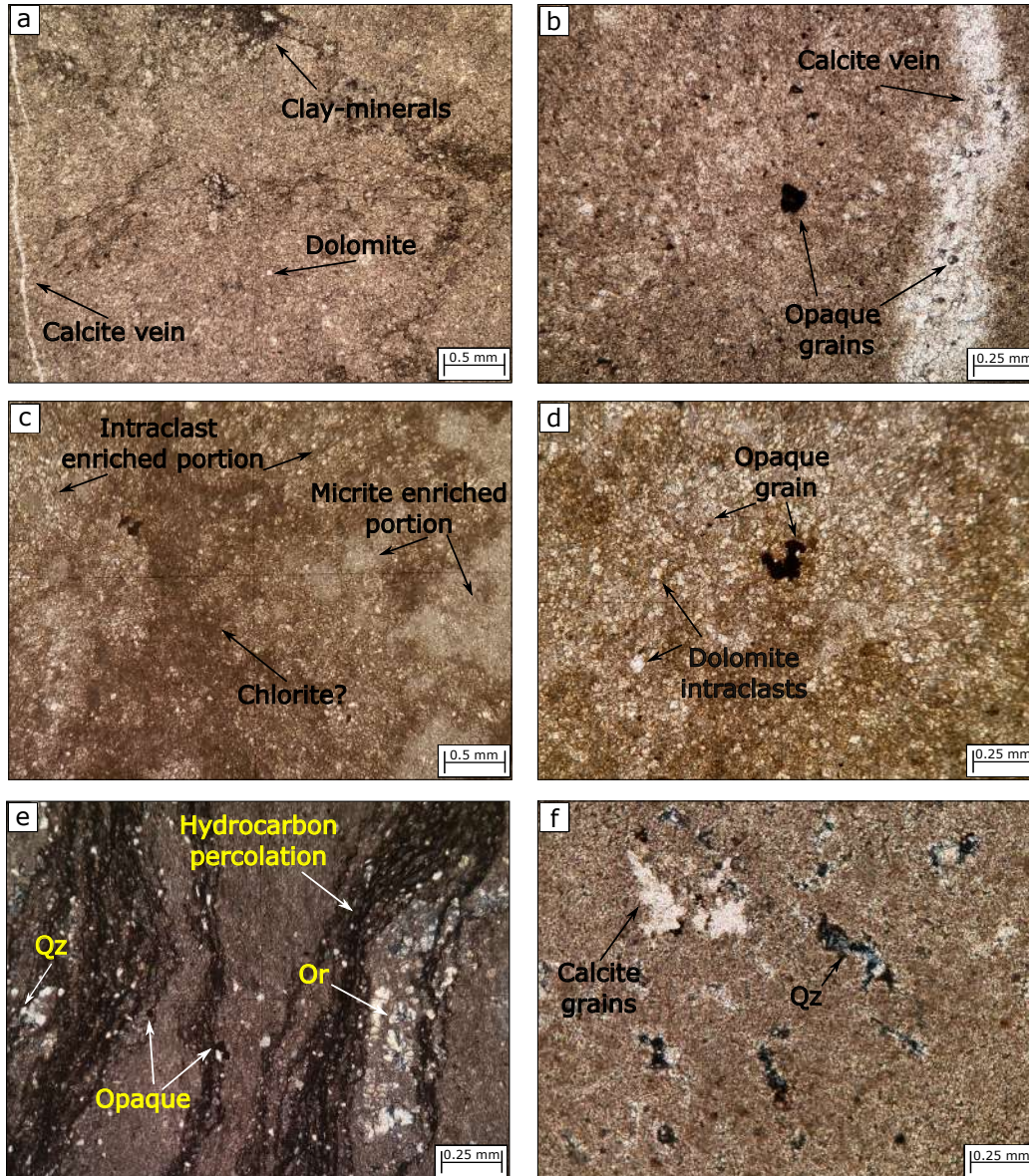


Figure 11. Thin sections ($30\mu\text{m}$ of thickness) of carbonate rocks under polarised light. Sete Lagoas (a, b), Salitre (c,d), Guia Formation (e) and Mirassol d'Oeste formation (f). All these samples are enriched in clay content, which confirms the previous observation of important paramagnetic contribution to magnetic hysteresis and, also, the XRD data.

866 there are clear signs of fluid percolation in the Mirassol d'Oeste samples and they are also
 867 enriched in clay content, their texture is more “homogeneous” compared to the examples of
 868 the Guia Formation that were investigated. A commentary is also necessary on the opaque
 869 minerals observed in thin sections, since if these are ferromagnetic phases (l.s.) they would
 870 be in the MD range. Most of these anhedral grains are probably from a detrital origin, while
 871 more euhedral ones could have resulted from sin/post-diagenetic processes.

872 **4.3.2 Scanning electron microscopy with energy dispersive X-ray spectroscopy** 873 **(SEM-EDS)**

874 A first and textural observation is the lack of microporosities, which might indeed indicate
 875 a high degree of compaction (as suggested by their tenacity, previously observed in sample
 876 preparation methods) and partial recrystallisation reached in low-grade metamorphic condi-
 877 tions. Iron-bearing minerals are distributed throughout the thin sections, dispersed within
 878 the matrix. The largest concentrations of iron are in single-elementary regions (with the
 879 exception of oxygen), indicating these are dominant phases as iron oxides. There are large
 880 anhedral (probably MD) grains, spread in the carbonate matrix. Confirming petrographic
 881 observations, most of the carbonate material in all the studied samples is calcite. Dolomite
 882 is more frequent in samples of the Salitre Formation. A large amount of aluminosilicates
 883 is present in the three remagnetised units. Based on petrographic and XRD data, one can
 884 assume these to be smectite, illite, chlorite, or K-feldspar. Therefore, it is possible to seg-
 885 ment the occurrence of these aluminosilicates based on the presence of Al, Si, Mg, Fe, and
 886 K: (R_i) regions with the presence of both Si, Al, Fe (or Si and Al only) and depleted in
 887 Mg and K (Figure 12a,c); (R_{ii}) regions with the presence of Si, Al, Mg, Fe but depleted of
 888 K (Figure 12b); and (R_{iii}) regions gathering Si, Al, K but depleted of Mg and Fe (Figure
 889 12b). Both chlorite and smectites are aluminosilicates that may contain Fe and Mg in their
 890 structure, so regions (R_i) and (R_{ii}) could correspond to such phases. In contrast, K-feldspar
 891 and illite chemical signatures would match region (R_{iii}), but I-Sm structures could show all
 892 these elements in their spectrum (depending on the degree of illitisation).

893 Observations show a strong spatial correlation between aluminosilicates and iron oxides and
 894 sulphides. In examples like in Figure 12b, the proximity of clays and iron oxides could even
 895 be a direct proxy for the crystallisation of magnetic minerals due to smectite illitisation.
 896 The texture of the iron oxide particles is usually rounded, with some examples of subhedral
 897 habits, and diameters smaller than 1000 nm. Iron sulphides usually occur as small isolated
 898 particles (not larger than $2\mu\text{m}$), especially in the Bambuí (*Supplementary file*, Figure
 899 S3a) and Irecê (*Supplementary file*, Figure S3a) samples. Framboids frequently occur
 900 in the Guia Formation, as euhedral cubic crystals (< 1000 nm) in between clay layers
 901 (*Supplementary file*, Figure S3c). In the last case, percolating hydrocarbon might trigger
 902 smectite-illitisation by carrying K^+ from dissolved K-feldspars, and with strong inputs of
 903 hydrogen sulphide within and the releasing as Fe^{2+} from clay-transformation, the nucleation
 904 of pyrite and its framboid aggregation will occur.

905 **4.4 Synchrotron X-ray fluorescence (XRF) and X-ray absorption spectroscopy** 906 **(XAS)**

907 For all the studied samples, calcium, iron, and potassium characterised the main constituents
 908 of the regional XRF spectrum (*Supplementary file*, Figure S4d). Dark regions within the
 909 maps are composed of elements invisible to the detectors (*Supplementary file*, Figure
 910 S4a,b,c). In this case, this element is most likely silicon, since (i) its emission energies
 911 ($K\alpha \approx 1739.98\text{eV}$) are below the spectroscopic range of the CARNAÚBA; (ii) the thin
 912 sections are attached to a silica plate (of 1 cm^2); and (iii) the high-energy X-ray beam
 913 penetration depth completely trespass the $30\ \mu\text{m}$ thickness of the samples, which also differs
 914 this data from other analytic methodologies, like ordinary EDS, since it receives signal not
 915 only from superficial particles but also for those in depth.

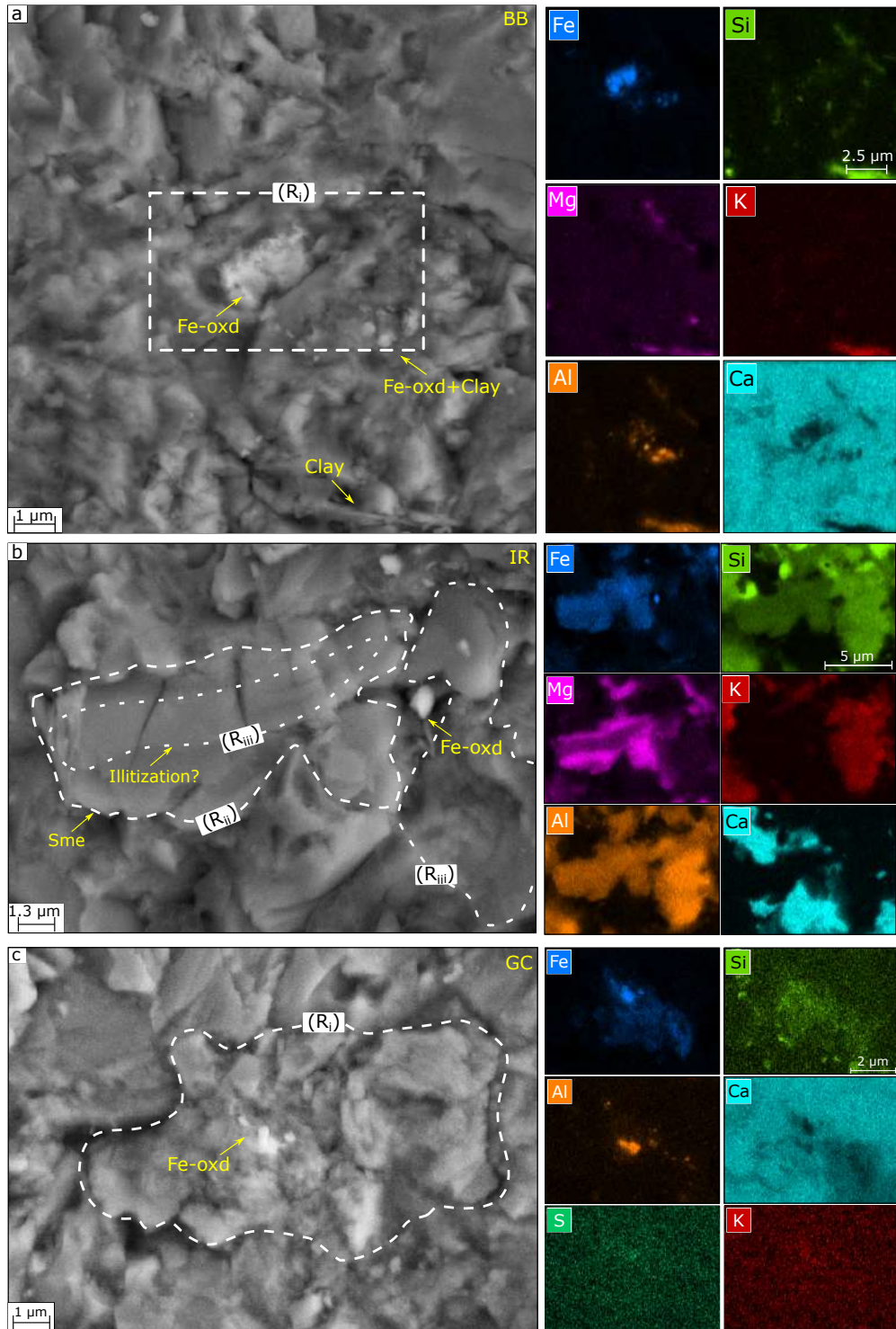


Figure 12. SEM (SE-mode) images showing the occurrences of iron oxides (Fe-oxd) near aluminosilicates in samples of the Bambuí (a) and Irecê basin (b), as well as in Guia Formation (c). The right-column images are EDS chemical maps with the same target in the left column. R_i , R_{ii} , and R_{iii} highlight the chemically different occurrences of the aluminosilicates (smectite, illite, chlorite) and/or K-feldspar (check SEM section for clarity). Sme: smectite.

916 Besides the importance of detecting “iron islands” as a marker of the presence of possible
 917 ferromagnetic grains (previously detected through the magnetic mineralogy experiments),
 918 most of the potassium is spatially correlated to these occurrences as well. Comparing this
 919 data to previous XRD and petrographic data, potassium should be related either to the
 920 clay minerals from the rock matrix or to K-feldspar. Once again, these are both important
 921 correlations to associate the remagnetisation of these units to smectite-illitisation, even if
 922 paired with mechanisms (such as hydrocarbon percolation, in the case of Guia samples).

923 Following the XAS data, for the Bambuí example (Figure 13a), a rounded particle in focus
 924 is shown to decrease iron concentration from the centre towards the border. Its pre-edge
 925 region in XAS (Figure 13a'), also present in the other samples evaluated through XAS
 926 analysis, arises from $1s \rightarrow 3d$ transitions present in K-edges of first-row transition metals
 927 (Penner-Hahn, 2003; Shulman et al., 1976). The rising-edge region does not entirely match
 928 the spectrum of bulk phases of magnetite, maghemite, or haematite. Energy shifts of the
 929 absorption threshold occur due to the distinct Fe-O bond lengths, so local geometry influ-
 930 ences the chemical sensitivity of XANES (Piquer et al., 2014). For this specific particle,
 931 the rising edge and central peak more strongly match with maghemite. Since iron seems to
 932 diminish from the centre towards the border (Figure 13a), this might indicate a core-shell
 933 structure, where a preserved magnetite is surrounded by a maghemite rim. This particle
 934 would then be within the theoretical PSD range of magnetite, while its morphology would
 935 point towards a diagenetic origin. This is also evidence of an isolated ultrafine particle in
 936 the rock matrix, that would contribute to a central ridge in FORC diagrams. And more
 937 importantly, it is a direct observation of a magnetic mineral within the stable PSD range
 938 (Nagy, 2017), capable of maintaining a very stable remanence and a probable product of
 939 alteration chemical remanence (a-CRM) after an in-situ crystallisation.

940 For the example shown for the Irecê sample (Figure 13b), subhedral and irregularly shaped
 941 particles of around 1000 nm yield a XANES spectrum whose rising edge and central peak
 942 match with magnetite. These nanoscopic particles are dispersed within an iron-bearing
 943 net, possibly iron-bearing silicates. The narrow peak (Figure 13b') is a common “white-
 944 line” feature, which indicates an intense absorption in the near-edge (Penner-Hahn, 2003).
 945 These are interesting results that demonstrate that even if haematite or pyrrhotite may give
 946 important contributions to the remanence of these rocks, very thin magnetite particles are
 947 present in the Salitre rocks as well. In this case, we interpret this as a probable growth
 948 chemical remanence (g-CRM), due to its chemical purity. Yet again, these ranges are still
 949 within the stable range of PSD grains and are mostly the ones bearing a stable remanence.

950 For the Guia sample, although iron oxides are more common, we show an example of
 951 a globular-shaped particle (Figure 13c) yielding an XAS spectrum matching with pyrite
 952 (FeS_2) (Figure 13c'). Right ahead of the pre-edge region, there is an increase of energy
 953 before the main peak, which has also been detected in the nanoparticulate phases of FeS
 954 (Matamoros-Veloza, 2018). Nevertheless, the match between the reference material and the
 955 data supports the interpretation of such a particle as a pyrite framboid as their presence is
 956 common in sedimentary systems with hydrocarbon (Machel, 2001).

957 Collaboratively, the utilisation of highly precise XRF and XAS data forms a potent tool
 958 for investigating remanence-bearing minerals in weakly magnetic rocks. In addition to
 959 identifying grains falling within the vortex state dimensions for magnetite, as observed by
 960 Nagy et al. (2019) (Nagy, Williams, Tauxe, & Muxworthy, 2019), our analysis reveals even
 961 smaller mono-elementary regions enriched in iron dispersed throughout the samples (as in
 962 Figure 13b). While the morphology of these smaller grains is challenging to discern due to
 963 experimental constraints, they likely signify even smaller particles within the thin section,
 964 approaching the limits of PSD with SD states. In the case of remagnetised carbonates,
 965 this innovative approach provides a new means of confirming the presence of clay minerals
 966 surrounding authigenic ferromagnetic minerals and verifying their respective phases.

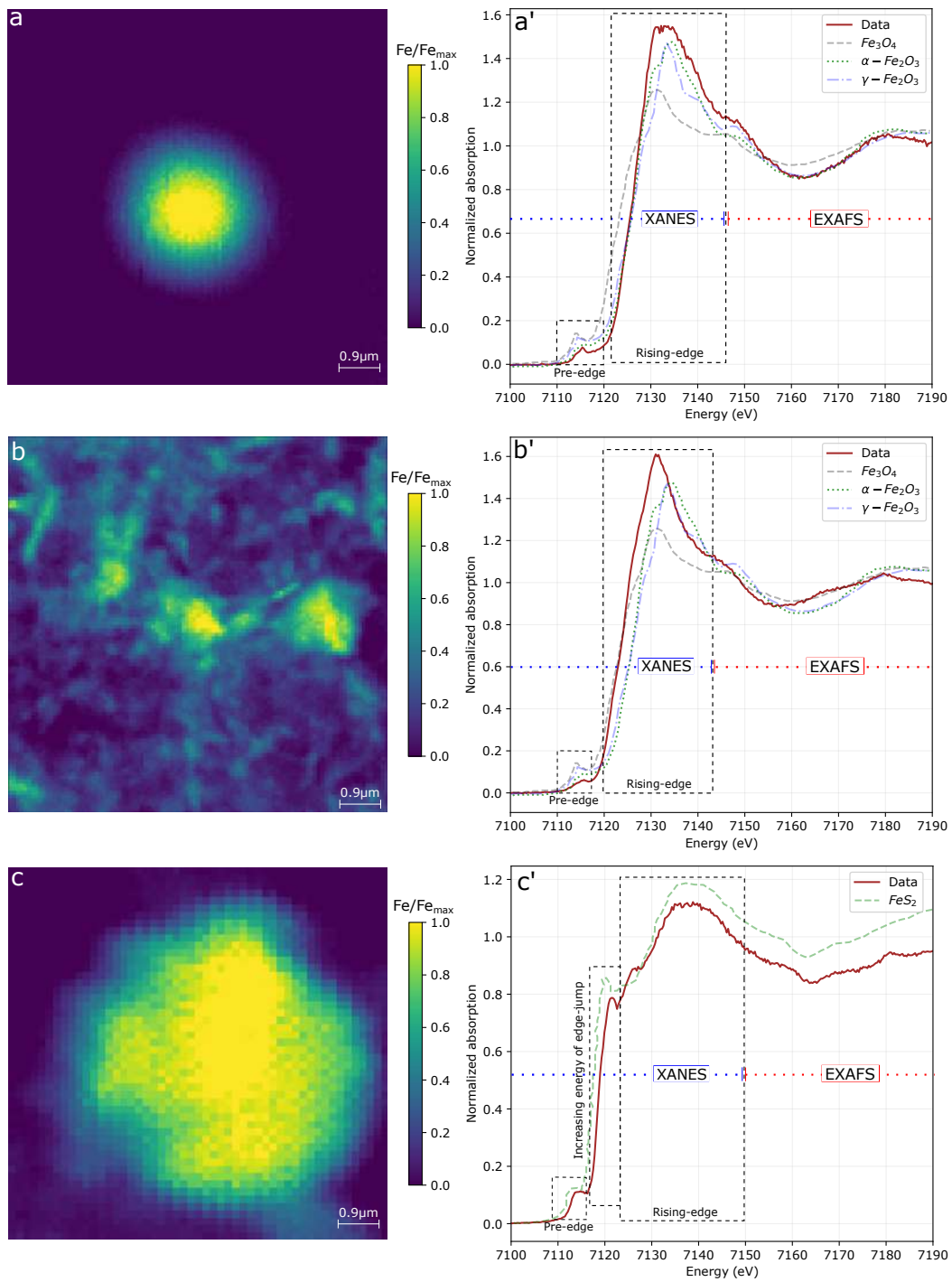


Figure 13. Compositional maps of Fe ($K\alpha \approx 6400\text{eV}$) for the Bambuí, Irecê, and Guia samples (a,b and c, respectively). Normalised XAS spectrum collected in fluorescence mode around the iron activation energy ($E_0 \approx 7112\text{eV}$) are shown in the right column (a',b' and c'), and compared to data extracted from literature: for magnetite, maghemite, and haematite from Piquer et al. (2014); and pyrite from Ravel (2013).

4.5 TGA-QMS

The examination of samples from the Araras Group adds a layer of intricacy to our understanding, introducing complexity arising from the interplay of hydrocarbon percolation. This process opens avenues for crystallisation through organic biodegradation processes (Emmertson et al., 2013). Notably, the Mirassol d'Oeste samples exhibit a consistent presence of stable detrital remanent magnetisation (DRM) components (Trindade et al., 2003; Font et al., 2005) while the overlying Guia formation bears only a secondary remagnetised component. In addition, Mirassol d'Oeste samples offer evidence of some degree of hydrocarbon percolation Júnior et al. (2016). It is important, therefore, to discern the extent of organic matter and hydrocarbon content within them. Our exploration extends to a TGA-QMS analysis, aiming to not only verify the presence but also quantify the pivotal amount of volatile components (such as CO_2 , SO_2 , SO_3 , and H_2O) in these samples.

H_2O is lost throughout the whole range of the analysed temperatures ($30 - 600^\circ C$) for all of the samples, following a linear trend, which is attributed to the loss of structural water (OH) from clay minerals. The most important mass loss event is related to CO_2 release, which occurs in a similar range for samples enriched in bitumen (Figure 14',c') with two major peaks, one at $50^\circ C$ and the other at $\approx 550^\circ C$. This is a common range for bitumen decomposition with peak liberation of CO_2 (Zhao et al., 2012) at $550^\circ C$. Thermal decomposition of calcite starts only around $700^\circ C$ (Karunadasa et al., 2019) while dolomite decomposition occurs between $700^\circ C - 750^\circ C$ (Gunasekaran & Anbalagan, 2007). Therefore, the CO_2 loss we show for these samples is related to none of these processes. More importantly, TGA-QMS analysis indicates that bitumen is also present at the base of the Mirassol d'Oeste formation, which was also previously reported by the work of Júnior et al. (2016). However, when looking at the ion current normalised by the individual mass of the samples (CO_2 /mass at the CO_2 's major peak), $MO_{transition}$ and GT samples have twice the mass of bitumen of MO_{base} . Nevertheless, this confirms that bitumen percolation was not so efficient in the base of the Mirassol d'Oeste formation, and that is probably why detrital remanence was preserved.

SO_3 emissions were not detected in the TGA-QMS analysis, but SO_2 is detectable in the GT and $MO_{transition}$ samples (Figure 14b',c'). For GT samples, SO_2 emissions occur between $420 - 540^\circ C$, while $MO_{transition}$ samples are between $\approx 400 - 430^\circ C$. We interpret these as related to pyrite. In atmospheres containing high amounts of O_2 in temperatures $< 800K$, pyrite will directly oxidise, but in a low-content O_2 atmosphere (or higher temperatures) it will be oxidised firstly to a mineral of the troilite group (pyrrhotite or troilite, (G. Hu et al., 2006)). Between $400 - 600^\circ C$ (in atmospheric air) pyrite will decompose to form FeS and S, so S further combines with oxygen to form SO_2 , and FeS will sequentially react with oxygen gas to form iron sulphate (Zunino & Scrivener, 2022). TGA analysis performed during the combustion of pyrite-bearing shales reported SO_2 emissions between $400 - 430^\circ C$ (Labus, 2020). The grain size of pyrite particles can also influence the range of SO_2 emissions because the thermal decomposition will strongly influence the kinetic phenomena. Emissions of fine particles ($< 45\mu m$) should start around $320^\circ C$, stopping around $540^\circ C$, while larger particles' ($< 200\mu m$) emissions begin around $450^\circ C$ (stopping around $550^\circ C$, (Zumaquero et al., 2021). Pyrrhotite decomposition in GT samples should be contained within the higher temperature SO_2 emissions, but since these are too restricted in $MO_{transition}$ samples they are probably not in the detection range.

5 Discussion

5.1 Remagnetisation fingerprints (?) of South American Neoproterozoic carbonates

Classical paleomagnetic/paleointensity techniques apply magnetic measurements to infer the composition, size distribution and remanence of macroscopic (bulk) samples. There are

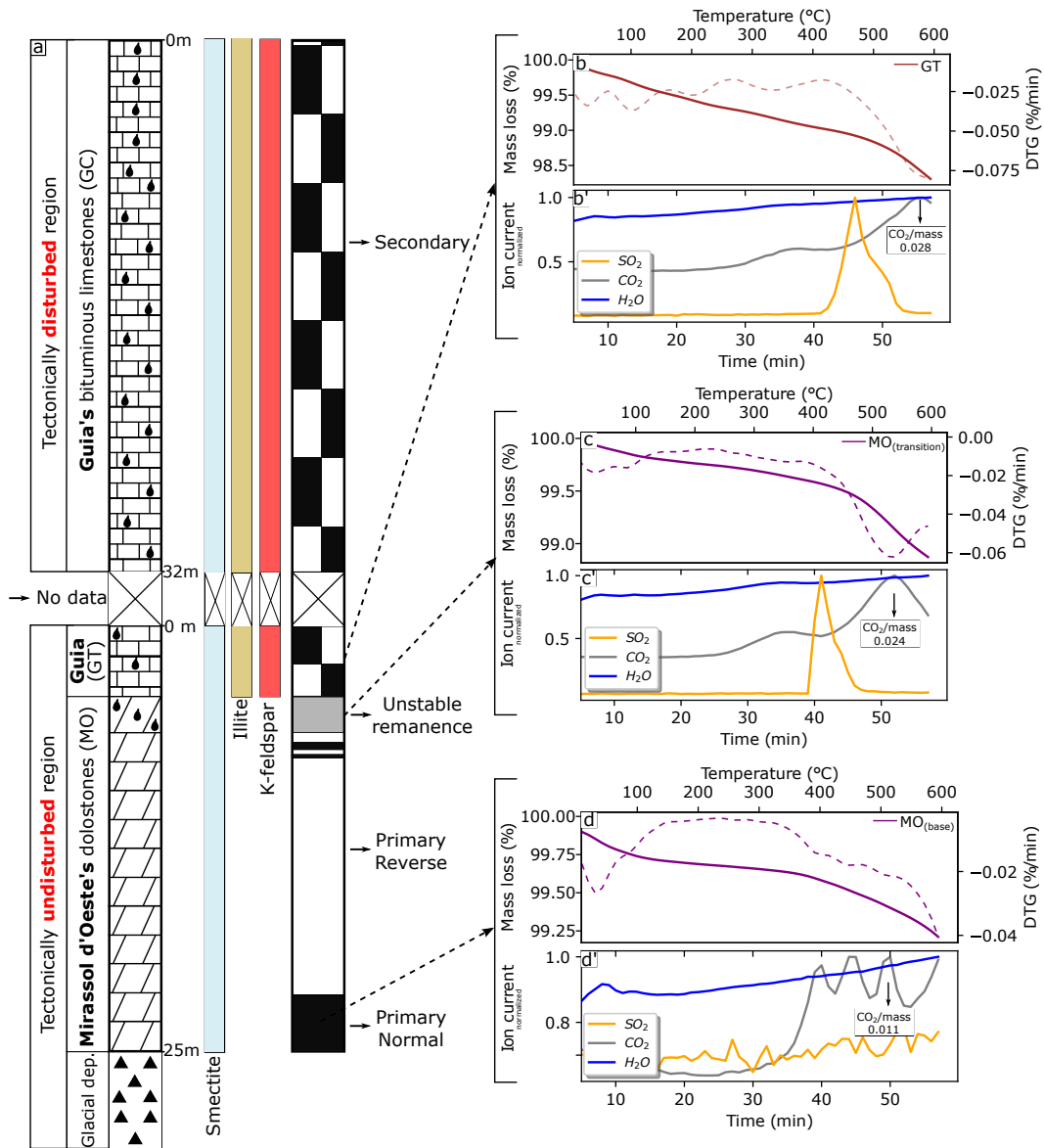


Figure 14. a) Stratigraphic profiles of the Araras Group over the deformed (Paraguay belt) and underformed regions (Amazon craton), modified from Trindade et al. (2003); Font et al. (2006). Blue, ocher and red bars indicate where the presence of smectite, illite and K-feldspar (respectively) was detected through either DRX, petrography, or SEM analysis. The polarity chart shows that Guia Formation only yields a remagnetised component, while percolation of bitumen in the upper section of the Mirassol d'Oeste formation ($MO_{transition}$) has completely erased stable remanence. In the right column, thermogravimetric analysis coupled to a Quadrupole Mass Spectrometer (TGA-QMS) shows the mass loss (%) of the basal stratum of b) Mirassol d'Oeste (MO_{base}), its bitumen-enriched portion c) ($MO_{transition}$) and the overlying d) Guia Formation (GT). Normalised ion current flow (b',c', d') allows the detection the volatilised emissions throughout the heating process.

1017 many advantages to using bulk samples, which include: (i) avoiding heterogeneous char-
1018 acteristics that might not be representative of the larger sample; and (ii) data acquisition
1019 techniques that are relatively fast, simple, sensitive to even trace amounts of magnetic min-
1020 erals, and representative of the overall behaviour of an assemblage of grains. Nevertheless,
1021 this approach may mask important magnetic phenomena or lead to erroneous interpretations
1022 due to the ambiguity of the techniques.

1023 Distortion in hysteresis, IRM and ARM curves is very often present in natural samples, often
1024 due to the effect of a mixture of grains with different magnetic properties, which commonly
1025 rely on unmixing techniques to better understand their component characteristics (U. Bel-
1026 lon et al., 2023; Egli, 2003; Maxbauer et al., 2016). Populations of grains with different
1027 magnetic properties might arise either for groups of particles with different compositions or
1028 for particles with the same composition but in a distinctly different domain state. When we
1029 consider any geological event triggering the growth of new magnetic grains, it is expected
1030 that some grains will grow beyond their blocking volume (VB) where their magnetic state
1031 is stable, and so produce a stable growth-chemical remanence, whilst another population
1032 of grains within the sample might still not have grown beyond the superparamagnetic (SP)
1033 threshold, where the grains are not capable of holding a magnetic recording. It is very logi-
1034 cal, therefore, to find an important contribution of SP particles in remagnetised carbonates
1035 that often contain significant quantities of SP particles, and so it is important to correctly
1036 identify and quantify such SP particles within the total population of magnetic grains.

1037 SP particles can strongly influence magnetic hysteresis (Tauxe et al., 1996) and low/high-
1038 frequency susceptibility (Hrouda et al., 2013). However, their quantification is likely prob-
1039 lematic for both of the techniques. Mixtures of distinct coercivity components can also cause
1040 both potbelly and wasp-waisted hysteresis (U. Bellon et al., 2023; Tauxe et al., 1996), and,
1041 but there are many possible mineral alteration pathways by which a remagnetised carbonate
1042 could create more than one magnetic mineral in sufficient quantity to influence the samples’
1043 bulk magnetic properties. When we observe hysteresis parameters in the Day plot (Figure
1044 6) compared to other compiled remagnetised carbonates, our data do not necessarily match
1045 with the “remagnetised fingerprint”, even though they are distorted hysteresis loops. What
1046 all of the studied samples have in common are properties that match with the PSD state.

1047 The PSD state describes a great variety of magnetic structures limited between the SD
1048 and MD states. It can also be broadly defined in terms of single and multi-vortex states
1049 often characterised by magnetisation helicity within a grain. From a uniform SD state, the
1050 magnetic domain states evolve from a flowering state to a single-vortex (SV) and further
1051 on to a multi-vortex (MV) state, after which it becomes energetically favourable to form
1052 large uniformly magnetised regions separated by domain walls in what is known as mul-
1053 tidomain (MD) states (Nagy, Williams, Tauxe, & Muxworthy, 2019). A long-held premise
1054 of palaeomagnetism is that SD grains contain stable remanences on the scale of billions of
1055 years (Butler, 1992). However Nagy (2017) have shown, through micromagnetic models,
1056 that there is an unstable magnetic zone (UMZ) whose grain size range approaches 50% of
1057 the SD size range. Within the vortex state, there are many possible domain configurations,
1058 the main ones are described as hard-aligned SV (HSV) and easy-aligned SV (ESV) states.
1059 Although the ESV magnetic structure can yield stabilities exceeding that of SD (Nagy,
1060 Williams, Tauxe, Muxworthy, & Ferreira, 2019), HSV states are often unstable, even at
1061 room temperature (Nagy, 2017). For equidimensional octahedral grains of magnetite, the
1062 UMZ occurs for grains sizes of 84-100 nm, but this range will vary with both mineralogy
1063 and morphology (Wang, 2022; Nagy, Williams, Tauxe, Muxworthy, & Ferreira, 2019).

1064 Particles within the UMZ will suffer not only a decrease in thermal stability, but other
1065 magnetic properties will change as well. For instance, coercivity is largely reduced and
1066 the magnetic susceptibility can be as high as those of SP particles (Wang, 2022; Nagy,
1067 Williams, Tauxe, Muxworthy, & Ferreira, 2019). These results might have a profound
1068 implication for the interpretation of bulk magnetic properties of remagnetised carbonates
1069 since the effects of distorted hysteresis loops and the frequency-dependent susceptibility of

1070 grains within the UMZ could be erroneously interpreted as the result of SP grains. Because
 1071 the UMZ can occupy a large range of sizes between the SD and ESV states, a significant
 1072 amount of authigenically grown grains could be magnetically unstable. In addition, chemical
 1073 alteration processes (like maghemitisation) that create a core-shell structure within the
 1074 magnetic particle will reduce the dimension of fine-grained parent particles as the daughter
 1075 phases grow, thereby moving the parent phase to within the UMZ zone (Ge et al., 2021).
 1076 That could be the case for grains as those observed for the Bambuí sample (Figure 13b).

1077 For samples containing multiple types of magnetic minerals, more reliable methods, such
 1078 as FORC diagrams, are available for inferring domain states. In our investigations, remagne-
 1079 tised carbonates exhibit FORCs indicating a central ridge, attributed to non-interacting
 1080 single domain/PSD grains (Roberts, 2022). This interpretation is supported by our direct
 1081 microscopic observations (Figures 12, 13). The frequent distribution towards zero coercivity
 1082 suggests the likely presence of SP particles. However, the significance of these contributions
 1083 to the bulk properties of rocks remains open for discussion. Frequency-dependent suscepti-
 1084 bility may not be sensitive enough to characterise them accurately (as it is observed in the
 1085 dispersion of χ_{ON}/χ_{FN} parameters of Figure 5) and is subject to uncertainties in samples
 1086 with multiple magnetic minerals.

1087 Despite potential reasons linking specific properties of remagnetised carbonate rocks, false
 1088 negatives might persist. In cases where carbonate rocks only carry secondary components,
 1089 anomalous properties may not be observed and they might be very similar to primary
 1090 remanence-bearing rocks (such as in MO samples), as seen in most of our studied remagne-
 1091 tised samples. Nonetheless, combining magnetic properties with other analytical techniques
 1092 (e.g., high-resolution chemical/mineralogical studies, as demonstrated in our study) can
 1093 clarify remagnetisation mechanisms and link them to significant geological phenomena in
 1094 sedimentary basins.

1095 5.2 West Gondwana large scale remagnetisation

1096 Despite employing a multidisciplinary approach to comprehend the characteristics of these
 1097 rocks, determining the primary trigger for remagnetisation remains a complex task. The
 1098 remagnetisation event's nature must align with a process capable of impacting vast ex-
 1099 panses of land. While fluid percolation seems enticing for such phenomena, it necessitates
 1100 the carbonate sequences to possess homogeneous porosity and permeability to enable the
 1101 remagnetisation of entire intracratonic basins within a short time frame. Further, although
 1102 orogenic fluid percolation may still play a significant role in initiating remagnetisation, the
 1103 fact that these basins share a remarkably similar mineralogical composition prompts con-
 1104 sideration of mineral transformation, specifically smectite illitisation, as a key candidate in
 1105 this discussion. Regardless, we also must take into account the geotectonic scenario, the
 1106 final amalgamation of the Gondwana and the Brasiliano orogenies happening throughout
 1107 the supercontinent (Figure 1a).

1108 Our interpretation considers a diagenetic evolution of these sedimentary basins and sequen-
 1109 tially discusses the implications of each particular phenomenon to the growth and preserva-
 1110 tion of the remanence.

1111 K-feldspars have been detected in all the remagnetised units, either through XRD or through
 1112 petrographic observation. Likewise, smectite and illite were also present in amounts to over-
 1113 come diamagnetic (calcite/dolomite) and ferromagnetic signatures in these rocks. Glacial
 1114 melting is the probably responsible source for the large influx of terrigenous materials in
 1115 these cap carbonates. K^+ will also be available in the pore waters. Early diagenetic re-
 1116 actions will mobilise ions of sulphur, where nanoprecursors (mackinawite) will likely form,
 1117 which are known precursors of other iron sulphides (Rickard, 1995). With an increase in
 1118 temperature, the medium tends to become more reductive and pH values stabilise around
 1119 slightly acid/to basic conditions (considering an evolution to normal geothermal trend on a
 1120 sedimentary basin). Any metastable iron-hydroxide of detrital origin tends to be consumed

1121 by iron-reducing bacteria (rather than metastable phases, Phillips et al. (1993)) so only the
 1122 most stable phases of iron oxides are preserved in the sedimentary column. The presence
 1123 of a minimum amount of S^{2-} in the medium from the consumption of mackinawite and
 1124 the availability of Fe^{2+} will lead to pyrite nucleation, since its formation is kinetically hin-
 1125 dered in such conditions (Rickard & Luther, 2007). When reaching a temperature around
 1126 $70^{\circ}C$, smectite-illitisation begins (Huggett, 2005) and Fe^{2+} ions are released into the sys-
 1127 tem. In such conditions, authigenic magnetite has the thermodynamic/kinetic conditions
 1128 to grow and main chemical stability (Pourbaix, 1974). As the intensive conditions (pressure
 1129 and depth) increase up to the peak of the illitisation reaction (120°), a g-CRM is slowly
 1130 acquired as the magnetite particles reach their blocking volume in a sin-diagenetic period.

1131 As suggested by: i) their degree of compaction (enough to make any macro-to-nanoporosities
 1132 be hardly detected); ii) the presence of incipient chloritisation, and iii) the illite KI values
 1133 (which indicates epizone temperatures), the rocks studied here must have reached low green-
 1134 schist facies (around 300°). As the diagenetic nature of the processes slowly transitioned
 1135 towards the incipient metamorphism (anchizone) towards higher temperatures, magnetite
 1136 still has the thermodynamic conditions to keep its growing process. But after 180° , mono-
 1137 clinic pyrrhotite growth is kinetically (Lennie et al., 1995) and is thermodynamic favoured
 1138 (Ning et al., 2015) under very similar pH/Eh conditions as those of magnetite. Likewise,
 1139 if sulphur and iron are in micromolar concentrations, pyrite thermodynamic stability will
 1140 collapse and its partial/total dissolution will provide the ions so monoclinic pyrrhotite (as
 1141 well as magnetite, Brothers et al. (1996)) can grow and eventually achieve a g-CRM.

1142 Aubourg et al. (2019) explored the occurrence of magnetite and monoclinic pyrrhotite in
 1143 clay-rich rocks, specifically shales and slates. The primary objective was to discern the coex-
 1144 istence patterns of these minerals under different temperature conditions, utilising magnetic
 1145 remanence analysis. Their findings indicated that magnetite and SP-pyrrhotite were simul-
 1146 taneously present within the temperature range of $77 - 128^{\circ}$. Additionally, at temperatures
 1147 ranging from $300 - 350^{\circ}$, MD magnetite coexisted with SD pyrrhotite, while temperatures
 1148 exceeding 347° exclusively revealed the presence of pyrrhotite. The study suggests that the
 1149 formation of pyrrhotite may occur at the expense of magnetite and can function as a temper-
 1150 ature indicator. It also proposes that rocks of this nature, when subjected to metamorphic
 1151 conditions, would record the magnetic field due to subsequent denudation processes and
 1152 cooling down, essentially exhibiting a thermoremanent magnetisation (TRM). However, our
 1153 samples presented some distinctive characteristics. Petrographic observation and the illite
 1154 crystallinity index both indicated incipient metamorphic conditions extending well beyond
 1155 128° but limited to low greenschist. Furthermore, the palaeomagnetic components obtained
 1156 from the thermal demagnetisation of the Sete Lagoas, Salitre, and Guia formations (Figure
 1157 15a) displayed unique demagnetisation behaviours attributed to both PSD/SD monoclinic
 1158 pyrrhotite and magnetite, resulting in statistically indistinguishable directions (Figure 15a').

1159 Because the detrital sources in the carbonatic matrix are not homogeneously distributed,
 1160 different sectors of a macro/micro-region can be influenced by the influx of Fe^{2+} /or S^{2-}
 1161 (from smectite-illitisation and/or sulphide dissolution) and therefore favour the growth of
 1162 either one of these ferrimagnetic minerals. If considering pyrite as a source for monoclinic
 1163 pyrrhotite growth (or even an early formed hexagonal pyrrhotite), its (FeS_2) previous for-
 1164 mation rates and distribution (during a previous early diagenetic stage) might harshly vary
 1165 with small distances because of local homogeneities and the formation/concentration of
 1166 metastable phases (Rickard & Luther, 2007). A new CRM registered by these ferromag-
 1167 netic particles could completely overcome a DRM/pDRM in terms of intensity (Kars et al.,
 1168 2012), explaining why only the remagnetisation component is observed in these rocks.

1169 Although the hypothesis seems to explain the formation of these ferromagnetic grains with-
 1170 out the necessity of summoning a problematic process such as orogenic fluid percolation,
 1171 it does not explain why their characteristic remanence bearing a single polarity produces
 1172 paleomagnetic poles with such restricted confidence ellipses (Figure 1b) far from the syn-

1173 diagenetic their ages. Instead, what we further discuss here is not the generation of these
1174 particles, but a thermal phenomenon able to lock their remanence in a very effective way.

1175 Palaeotemperature data calculated from the illite crystallinity index (KI) can be paired
1176 with the previously published paleomagnetic data (thermal demagnetisation) to propose a
1177 thermoviscous component for the remanence observed in these Neoproterozoic carbonates.
1178 When looking upon the lower-range blocking temperatures of the components yielded by
1179 magnetite (Figure 15a), i.e.: i) 340 – 360° for the Sete Lagoas (BB) samples; ii) 300 – 340°
1180 for the Salitre (IR) samples, and iii) 300° for the GC samples, the directional similarity (site
1181 means) is noticed as medium-to-high inclination vector with an NNE trend (Figure 15'),
1182 which is further confirmed by their paleomagnetic pole positions (Figure 1b).

1183 Since these units held crystallinity indexes indicating an epizone environment, let us consider
1184 its lower boundary (300°C) as the peak temperature to which these rocks were submitted.
1185 Following Néel theory (Néel, 1955), it is possible to attend that a remanence carrying grain
1186 (in these case particles that originally carried a g-CRM) when laboratory heated to an
1187 unblocking temperature T_1 along a relaxation time τ_1 would lose its remanence acquired at
1188 a given geological time (τ_2) at a T_2 temperature (Pullaiah et al., 1975):

$$\frac{T_2 \cdot \ln(C \cdot \tau_2)}{M_{s[T_2]} \cdot H_{c[T_2]}} = \frac{T_1 \cdot \ln(C \cdot \tau_1)}{M_{s[T_1]} \cdot H_{c[T_1]}} \quad (5)$$

1189 $M_s[T]$ is intrinsically related to the remanence carrying phases, for magnetite (for example)
1190 it is $M_s = M_{s[293K]} - ((T_C - T)/(T_C - 293K))^{0.43}$ (Dunlop & Özdemir, 1997). The microco-
1191 ercivity of the same magnetic mineral is also temperature-dependent and arises mainly from
1192 shape anisotropy and/or magnetocrystalline anisotropy. Microcoercivity arising from shape
1193 anisotropy is (i) $H_{c[T]} = \Delta_{N(\text{demagnetizing factor})} \cdot M_{s[T]}$, while magnetocrystalline effects are
1194 (ii) $H_{c[T]} = K_{1[T]}/8 \cdot M_{s[T]} \equiv M_{s[T]}^{7.5}$ (Nagata, 1961; Stacey & Banerjee, 1974; Pullaiah
1195 et al., 1975) in which $K_{1[T]}$ is the first anisotropy constant. Because at NTP conditions
1196 the shape anisotropy controls the magnetisation in magnetite grains at least 10% elongated,
1197 $H_{c_{s,\text{anisotropy}}[T]} \equiv M_{s[T]}$.

1198 By following Pullaiah's approach (Eq. 5), the correspondent viscous relaxation curves (Fig-
1199 ure 15b) are calculated, making it clear that if these rocks were exposed to an environmental
1200 temperature of 300° for a short period (< 10 years) it would be enough to completely relax
1201 their remanence. If we consider a continental context in which the basins were kept warm
1202 under low greenschist metamorphic conditions, their remanence would be constantly reset
1203 until a temperature-decreasing scenario.

1204 A g-CRM remanence component carried by monoclinic pyrrhotite (which is even statistically
1205 similar to that of magnetite) would be easily erased since their blocking temperatures do
1206 not surpass 300°. After a temperature drop, these authigenic grains would block their
1207 directions again. Similarly, to magnetite, pyrrhotite viscous decay becomes steeper near its
1208 T_c (Dunlop et al., 2000), and since none of the samples of the Bambuí, Irecê or Araras'
1209 pyrrhotite components showed blocking temperatures smaller than 250° (D'Agrella-Filho
1210 et al., 2000; Font et al., 2006; Trindade et al., 2004), the blocking of directions along the
1211 environment heat dissipation (even at slow cooling rates) would rapidly occur. There is
1212 only a small difference between the characteristic remanence yielded by the pyrrhotite and
1213 magnetite components in these rocks, the first one yielding mean site directions with much
1214 lower precision parameter (k) and larger confidence ellipses (α_{95}) than the second one.

1215 The paleomagnetic register of pyrrhotite-bearing rocks exposed to metamorphic conditions
1216 can officially register the magnetic field as they cool down, but such efficiency of polarity
1217 recording is strictly connected to cooling rates (Rochette et al., 1992). In fact, the sequence
1218 of thermomagnetic experiments developed by Crouzet et al. (2001) for multipolarity-bearing
1219 remagnetised carbonates of the Western Alps confirms that single-domain pyrrhotite can
1220 sequentially register pTRMs during slow cooling.

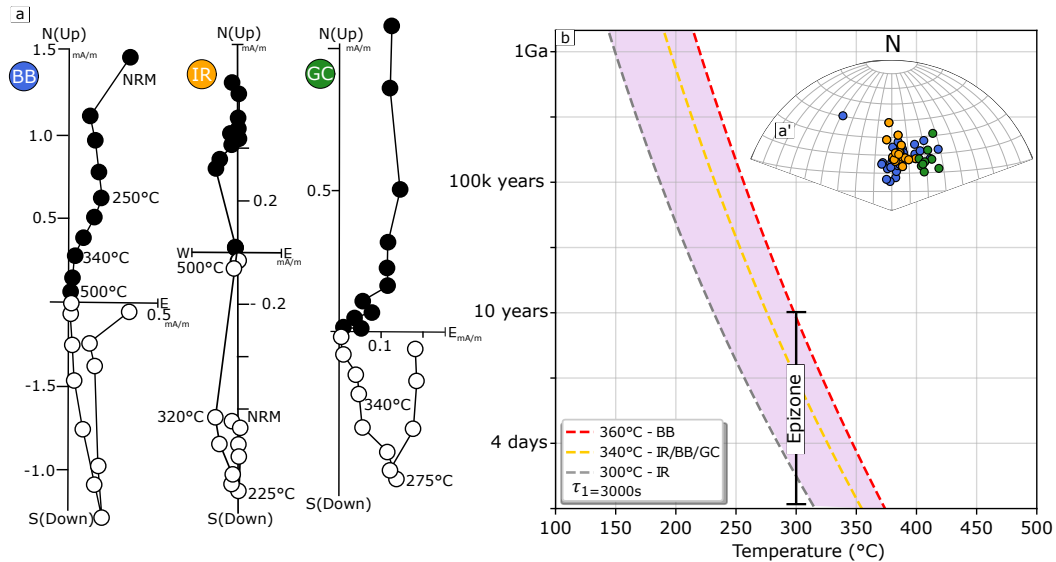


Figure 15. a) Zijderveld diagrams of thermally demagnetised samples from the Sete Lagoas (BB, D'Agrella-Filho et al. (2000)), Salitre (IR, Trindade et al. (2004)) and Guia in the Cáceres region (GC, Font et al. (2006)). a') Blue, orange and green circles represent site mean directions of the BB, IR and GC units (respectively). b) Pullaiah's nomogram (Pullaiah et al., 1975) for magnetite. Viscous relaxation curves are calculated (Eq. 5) using the blocking temperatures marked with dashed lines. Epizone's lower boundary is where relaxation curves are intercepted by the 300° isotherm.

1221 Distinguishing from remagnetised rocks bearing multipolarity components, Bambuí, Irecê
 1222 and Guia samples yield only a single polarity component related to pyrrhotite (as well as
 1223 for magnetite). A thermoviscous overprint of (what originally could be a g-CRM) caused
 1224 by a heating event and a succeeding cooling could explain the contemporaneity of such
 1225 components and the large-scale remagnetisation event affecting the whole of Gondwana.
 1226 The temperature increase from deep diagenetic conditions, up to the anchizone and further
 1227 to the epizone favours the conditions for monoclinic pyrrhotite to authigenically form.

1228 The most obvious candidates to elevate the temperatures up to low greenschist metamorphic
 1229 conditions are the collision events of the Brasiliano (Panafrican) orogenies, which culminated
 1230 in the amalgamation of different terranes to the Amazon and São Francisco Craton during
 1231 the Late Precambrian – Early Paleozoic (Almeida et al., 1973; Mohriak & Fainstein, 2012).
 1232 Peak metamorphic conditions related to the closing of the Clymene Ocean and bending of
 1233 the Paraguay belt event (the portion between the southeast margin of the Amazon craton
 1234 and the São Francisco Craton to the East, Figure 2b) has yielded a weighted mean age of ca.
 1235 528 ± 36 Ma ($^{40}\text{Ar}/^{39}\text{Ar}$) (Tohver et al., 2010). Such an event could easily remagnetize
 1236 the portion of the Guia Formation over the Cáceres region (GT) samples, and offer a diffusion
 1237 heat source for the nearby areas, where such formation lies undeformed over the Amazon
 1238 Craton (GT) region that did not reach high KU values such as those over the Paraguay belt.
 1239 As for the São Francisco Craton, the east bordering Araçuaí belt (Figure 2a) comprises a long
 1240 magmatic history (630- 480 Ma, Tedeschi (2016); Pedrosa-Soares (2020)), with metamorphic
 1241 peaks around 580 Ma (Pedrosa-soares, 2007). The Araçuaí belt history yields a characteristic
 1242 slow cooling of the middle crust, resulting in temperatures of 500°C around 510-500 Ma
 1243 (Vauchez et al., 2019). The effect of such a high-temperature regime on the nearby orogenic
 1244 region could explain the epizone conditions described by the illite-crystallinity calculations
 1245 in both Bambuí and Irecê. Other researchers have already reported carbonates from the

1246 Bambuí as overprinted by a greenschist metamorphism (Caby & Costa Campos Neto, 2022;
1247 Misi et al., 2014), including the presence of metamorphic chlorite.

1248 Even so, the fact these distinct units from basins separated hundreds of kilometres apart
1249 bear statistically indistinguishable paleomagnetic directions not only requires their contem-
1250 poraneous heating but a sequential cooling with a very restricted span of time. Early 2000's
1251 paleomagnetic works of Trindade et al. (2004) and D'Agrella-Filho et al. (2000) positioned
1252 the paleomagnetic poles of these remagnetised rocks around the 520 Ma interval in the
1253 Gondwana APW curve. However, when plotted along Gondwana's mean paleomagnetic
1254 poles APW curve (Figure 1b) of Torsvik (2012), the directions seem closer to the 460-470
1255 Ma interval. The high-quality poles of West Gondwana, e.g., SAVN (Araçuaí orogen in
1256 Brazil, 500 Ma) and CF (Pampia terrane in Argentina, 519 Ma) are far from remagnetised
1257 carbonates grouping (Table 1).

1258 Therefore, the blocking of remanent magnetisation in these carbonates could be linked
1259 to the Early- to Middle-Ordovician period. The Late-Cambrian/Early Paleozoic marks the
1260 termination of Gondwana's assembly and the orogenic collapse of Neoproterozoic belts (e.g.,
1261 the Araçuaí-Ribeira in the Brazilian Atlantic coast, Alkmim et al. (2006); Pedrosa-Soares et
1262 al. (2001); Wiedemann et al. (2002) and the Damara orogen (Southwest Africa, Goscombe
1263 et al. (2018)). Although there is a considerable amount of post-collisional magmatism
1264 related to this period, the end of the main orogenic activity should lead to the relaxation
1265 of the upwardly compressed isotherms (Fonseca et al., 2021). A Paleozoic cooling event
1266 is registered in most parts of the West Gondwana. Earliest zircon's AHe and ZHe ages
1267 of apatite and zircon crystals from the Neoproterozoic Dom Feliciano belt (South Brazil)
1268 show a spread of ages from 472 to 26 Ma, the Ordovician ages implying an exhumation
1269 of the crystalline basement. In the Brasília belt, apatite fission track ages (AFT, Fonseca
1270 et al. (2020)) indicate a fast increase of cooling ages around 480 Ma, which indicates the
1271 exhumation of the basement as well. Reported AFT ages in the São Francisco Craton
1272 (Fonseca et al., 2021) show that Early Paleozoic cooling ages quickly increase towards the
1273 Devonian, which could be the result of an interplay of interplate tectonics readjustments and
1274 erosional process (that could have been enhanced by Late Ordovician glaciation, Torsvik
1275 and Cocks (2013)).

1276 If the remanence observed in these units is related to the Paleozoic cooling event, that also
1277 explains why only a single polarity would be observed for magnetite/pyrrhotite (components
1278 B/C, Figure 15a), even considering such a large continental area), since the Amazon and São
1279 Francisco cratons would be in the southern hemisphere (Merdith et al., 2021) in such period,
1280 and so these components could be related to the Moyero superchron (Pavlov & Gallet, 2005).
1281 Still, considering to prove the Paleozoic cooling event as the thermal blocking mechanism
1282 responsible for freezing the remanence of authigenic minerals in carbonate rocks must be
1283 further tested. An important step would be applying numerical geodynamical simulations
1284 that would allow us to study the heat dissipation of the lithospheric mantle after major
1285 collisional events in a supercontinent since surface processes (such as denudation) can be
1286 intimately related to mantle dynamics (Braun, 2010; Sacek, 2014).

1287 **5.3 Hydrocarbon percolation in carbonates of the Araras group**

1288 Even after accounting for the remanence exhibited by rocks in the Guia Formation, whether
1289 from the deformed (GC) or undeformed (GT) terrain, which was also preserved during
1290 the Paleozoic cooling event, three questions regarding the carbonates of the Araras group
1291 arise: a) If we consider smectite-illitisation as a significant process for releasing Fe^{2+} and
1292 thereby facilitating the formation of authigenic ferrimagnetic minerals, why did smectite
1293 not undergo conversion to illite in the Mirassol d'Oeste (the underlying stratum to Guia
1294 formation)? b) What role does hydrocarbon percolation play within this geological unit?
1295 c) The majority of dolostones in the Mirassol d'Oeste exhibit only primary remanence.
1296 How is it then that only the limestones in the Guia Formation underwent remagnetisation,

1297 while the bitumen-enriched upper section of the Mirassol d'Oeste did not experience this
1298 phenomenon?

1299 Hydrocarbon strongly percolates in the Guia Formation, mostly occupying the S_0 structure
1300 or occurring as a forceful percolation that sections the stratigraphic layers, which suggests
1301 a post-diagenetic age for such fluids. Although the hydrocarbon should have originally mi-
1302 grated to the rocks of the Araras group, Júnior et al. (2016) has suggested that the alteration
1303 of these fluids to bitumen has happened in situ (indigenous origin). Mid-chain monomethyl
1304 alkanes analysed from gas chromatography in a sample from the Guia Formation are com-
1305 monly reported in mid-to-late Proterozoic oil and their source rocks (Júnior et al., 2016).
1306 Hydrocarbon occurrence often accompanies the development of authigenic ferromagnetic
1307 phases, as observed in various studies (Benthien & Elmore, 1987; R. Elmore et al., 1987;
1308 McCabe et al., 1987; Font et al., 2006; Aldana et al., 2011; Costanzo-Álvarez et al., 2019;
1309 J. Hu et al., 2023). Hydrocarbon biodegradation, a significant contributor to ion exchange
1310 and a potential catalyst for acquiring chemical remanent magnetisation is intricately tied
1311 to bacterial activity. Efficiency in hydrocarbon biodegradation within bacterial environ-
1312 ments is subject to various environmental factors, including compositional variations within
1313 hydrocarbon fluids, levels of oxygen availability, availability of nitrogen, phosphorus, and
1314 carbon, salinity impacting metabolic processes related to hydrocarbons, pressure modulat-
1315 ing reaction rates, water activity linked to rock permeability and porosity, and pH levels
1316 exerting a strong influence on the overall process (Leahy & Colwell, 1990). Finally, the
1317 temperature plays a crucial role in creating a suitable environment for the development of
1318 bacterial colonies in this context. Besides the effects of biodegradation, the maturation of
1319 organic matter within the carbonates (especially the hydrocarbon) could also induce the for-
1320 mation of authigenic magnetic minerals (Fruit et al., 1995; Banerjee et al., 1997). Certainly,
1321 the observed effects significantly influence the production of magnetic grains in the Araras
1322 group. It's important to note that the processes of smectite illitisation and organic matter
1323 maturation may not be entirely separate; there could be an overlap. This is because clays
1324 with a high organic matter content may play a connecting role, potentially facilitating the
1325 interaction between smectite illitisation and organic matter maturation processes (Kennedy
1326 et al., 2002; R. D. Elmore et al., 2012).

1327 While Font et al. (2005) describes the DRM of Mirassol d'Oeste dolostones as held by spec-
1328 ular haematite, the data reported by Trindade et al. (2003) show mainly magnetite blocking
1329 temperatures for such primary remanence. Magnetic experiments from this work for MO
1330 samples agree with Trindade et al. (2003)'s data, indicating there must be a stratigraphic
1331 variability in the basal stratum of the Mirassol d'Oeste formation. As for the Guia For-
1332 mation, the deformed region over the Paraguay belt was reported to have remanence held
1333 by both monoclinic pyrrhotite and magnetite, while remanence in the undeformed region
1334 over the Amazon craton would be held by pyrrhotite only (Font et al., 2006). Yet, the
1335 results shown here indicate that even if stable remanence is not carried by magnetite in GT
1336 samples, it is still present in these rocks.

1337 Our TGA-QMS analysis provided insights into the percolation of organic matter within the
1338 Araras group samples. This was achieved by correlating the release of volatile phases, specifi-
1339 cally CO_2 and SO_2 , with an increase in temperature. In our interpretation, the releases
1340 of CO_2 and SO_2 correspond to the decomposition of bitumen and pyrite, as explained in
1341 more detail in the results section. Our analysis aligns well with the observation of a signifi-
1342 cant amount of bitumen, comparable to the Guia formation, particularly within the upper
1343 portion of the Mirassol d'Oeste formation (referred to as $MO_{transition}$, see Figure 14c').
1344 This corresponds to a point where stable remanence completely disappears, as illustrated
1345 in Figure 14a. It's worth noting that hydrogen sulphide, a common sulphur compound
1346 in petroleum (Shi & Wu, 2021), can lead to the dissolution of iron oxides/hydroxides and
1347 sulphides upon contact. As suggested by Font et al. (2006), this phenomenon is likely re-
1348 sponsible for the disappearance of the primary direction in the upper section of the Mirassol

1349 d'Oeste formation, as hydrocarbon does not strongly percolate at the base of these cap
1350 carbonates (see emission in Figure 14d').

1351 If the biodegradation/transformation of hydrocarbons alone were the sole factor responsible
1352 for the pyrrhotite/magnetite crystallisation in the Guia Formation, one would expect the
1353 transition from Mirassol d'Oeste to the Guia Formation to exhibit stable remanence compa-
1354 rable to GT samples. This anticipation arises from the pervasive evidence of hydrocarbon
1355 percolation in the upper section of Mirassol d'Oeste. The mechanism involves the dissolu-
1356 tion of detrital ferromagnetic phases by H_2S , liberating iron, which then binds to sulphur
1357 to crystallise pyrite due to the required minimal sulphur content for its formation (Rickard
1358 & Luther, 2007). Similarly, the biodegradation of organic matter results in the reduction of
1359 iron facilitated by sulphate-reducing bacteria, leading to the formation of metastable mack-
1360 inawite. This metastable form can subsequently transform into nanoscopic crystals of pyrite
1361 (Duverger et al., 2020). Moreover, with increasing temperature, there is the potential for
1362 pyrrhotite/magnetite to crystallise at the top of the Mirassol d'Oeste formation. However,
1363 the observed stable remanence in GT samples suggests that factors beyond hydrocarbon
1364 biodegradation contribute to the unique crystallisation patterns in the Guia Formation.

1365 KI values of rocks of Guia Formation rocks over the Amazon craton are slightly greater
1366 than those over the Paraguay belt, indicating that GT samples (and consequently MO sam-
1367 ples) could have reached anchizones' temperatures, meaning that the necessary temperature
1368 ($70 - 120^\circ C$) to convert smectite to illite was achieved. Still, significant K^+ mineral sources
1369 were not found in analysed MO samples, either through petrographic or XRD data. Illiti-
1370 sation of smectite requires potassium inputs (Huggett, 2005), which is probably delivered
1371 by orthoclase dissolution in the Guia Formation, and the lack of sources of such element
1372 could inhibit the driving mechanism of pyrrhotite and magnetite authigenic formation in
1373 MO samples. With the increase of temperature towards anchizone conditions, smectite-
1374 illitisation delivers more Fe^{2+} in the medium and the thermodynamic conditions necessary
1375 to monoclinic pyrrhotite arise. In both the deformed and undeformed regions, magnetite
1376 and pyrrhotite can nucleate. However, over the non-deformed region, the remanence is held
1377 only by pyrrhotite (although magnetite is also detected in such samples). We speculate this
1378 could be related to the higher temperatures achieved in the Paraguay belt region, which
1379 favours multiple mechanisms (including clay transformation and organic matter maturation
1380 reactions) to be paired and, consequently, a larger volume of magnetite particles would
1381 eventually reach the blocking volumes to bear, together with pyrrhotite, a stable remanence
1382 (GC samples).

1383 6 Conclusion

1384 In this manuscript, we have assessed the remagnetisation of Neoproterozoic carbonate rocks
1385 in South America, employing paleomagnetic analyses alongside macro/microchemical and
1386 imaging approaches. In this context, we scrutinise not only the extensive remagnetisa-
1387 tion influencing intracratonic basins throughout West Gondwana, elucidating the geological
1388 phenomena underpinning it, but also appraise how the magnetic characteristics align with
1389 anticipated magnetic "fingerprints" associated with carbonate remagnetisation.

1390 Except for samples from the Irecê basin, the hysteresis parameters in our study deviated
1391 from the globally observed cluster of remagnetised rocks. Instead, they closely aligned with
1392 non-remagnetised carbonate units around the pseudo-single domain area. This discrepancy
1393 leads to a "false negative" scenario for the identified fingerprint. In simpler terms, these car-
1394 bonate rocks only reveal a secondary component and do not exhibit the expected behaviour.
1395 Taking a broader perspective, the unusual Hcr/Hc ratios in remagnetised carbonates typi-
1396 cally correspond to mixtures of SD+SP particles. Despite our efforts to quantify the SP
1397 contribution through susceptibility loss in frequency-dependent measurements, which indi-
1398 cates a susceptibility loss of over 5% in most samples from remagnetised units (attributed
1399 to remagnetised carbonates), we cannot solely attribute this behaviour to SP particles due

1400 to the limitations of our method. Additionally, samples from our control unit, the base of
1401 the Mirassol d'Oeste (non-remagnetised), show a susceptibility loss comparable to that of
1402 the Bambuí em Irecê formation, highlighting another challenge to the original fingerprint
1403 assumptions. On the other hand, FORC diagrams reveal a predominant distribution along
1404 the coercivity axis, indicating a broad spectrum of non-interacting single-domain/pseudo-
1405 single-domain grains. For instance, FORC distributions frequently reach zero coercivities,
1406 potentially providing more concrete evidence of SP particles in these rocks. In contrast,
1407 the non-remagnetised unit demonstrates a much larger contribution to the interaction axis
1408 rather than the coercivity axis. Nevertheless, our thermal experiments, specifically the
1409 Lowrie test, support the earlier paleomagnetic interpretation that monoclinic pyrrhotite
1410 and magnetite are the primary magnetic carriers in these rocks remagnetised rocks. Conse-
1411 quently, samples comprising an assemblage of more than one magnetic mineral will exhibit
1412 the collective properties of these magnetic carriers, making it challenging for their position
1413 on the Day plot diagram to carry a clear genetic connotation regarding the origin of their
1414 remanence (whether primary or secondary).

1415 Proposing mechanisms like orogenic fluid percolation to explain remagnetisation would nec-
1416 cessitate a textural homogeneity, specifically in terms of porosity and permeability. This
1417 homogeneity would be required to account for the simultaneous remagnetisation of basins
1418 separated by significant distances. While fluid percolation can indeed induce changes in
1419 the redox/pH state of the environment and prompt alterations, if the rocks lack a uni-
1420 form fabric, these changes should be localised along the pathways of fluid percolation.
1421 Instead, we posit that the development of secondary magnetic minerals in these rocks is
1422 intricately linked to temperature increases and the smectite-illite transformation that re-
1423 leases Fe^{2+} into the medium. This released iron can then nucleate to generate magnetite
1424 and/or react with sulphur from the dissolution of other sulphides (e.g., pyrite), leading
1425 to the generation of monoclinic pyrrhotite as temperatures rise. XRD analysis, supported
1426 by petrographic/microscopic data, confirms the presence of both smectite and highly crys-
1427 talline illite, along with mineral sources of K^+ (orthoclase) necessary for the reaction to
1428 occur. In all the examined samples, we observe a spatial correlation of aluminosilicates
1429 with iron oxides/sulphides through micro-XRF. Significantly, XAS analysis allows us to
1430 confirm the presence of irregularly shaped grains of pure magnetite and core-shell struc-
1431 tures of maghemite-magnetite within the aluminosilicates, both with coherent dimensions
1432 of PSD grains. Specifically in the Guia formation (where bitumen is abundant), the gen-
1433 eration of these authigenic phases is believed to be an interplay between organic matter
1434 maturation/biodegradation and smectite-illitisation.

1435 Henceforth, we recommend that researchers investigating carbonate sedimentary systems
1436 with high detrital content from a palaeomagnetic standpoint should examine both the pres-
1437 ence and composition of clay minerals. Additionally, they should explore the spatial relation-
1438 ship between these clay minerals and potential carriers of remanence, as clay transformation
1439 may play a significant constraint on magnetic mineral authigenesis.

1440 While the processes we discuss here are linked to those initially capable of generating miner-
1441 als under their respective Curie temperatures and consequently imparting chemical remanent
1442 magnetisation, our proposition suggests that the current remanence of these basins results
1443 from thermoremanent magnetisation. A crucial observation supporting this interpretation
1444 is the statistically similar directions exhibited by both pyrrhotite and magnetite components
1445 in all these basins. This implies a rapid blocking process capable of influencing a continen-
1446 tal area. Analysis of the thermal demagnetisation data of these samples leads us to infer
1447 that only a few thousand years of exposure to temperatures above $300^{\circ}C$ would suffice to
1448 thermally relax the magnetisation of both pyrrhotite and magnetite. The crystalline index
1449 of illite in these samples, along with petrographic observations and previous data, confirms
1450 that these samples likely experienced temperatures equivalent to low-greenschist grades. We
1451 propose that such heat must have been generated during the final amalgamation of Gond-
1452 wana. As the heat propagation progressively increases, it unblocks the remanence of these

1453 ferrimagnetic phases, prompting a constant reset of the remanence. In conclusion, sequential
 1454 cooling after the Brasiliano orogeny relaxes the isotherms previously shifted upwards due to
 1455 the collision. Consequently, this process locks in the remanences on these basins across the
 1456 continent, elucidating their similar single-polarity remanences. These remanences reflect
 1457 poles falling close to the Early-Middle Ordovician medium poles of the Gondwana apparent
 1458 polar wander path.

1459 Open Research Section

1460 The experimental data reported in this research is stored at Zenodo (U. D. Bellon et al.,
 1461 2023) and can be publicly accessed at <https://doi.org/10.5281/zenodo.10283417>.

1462 Acknowledgments

1463
 1464 Magnetic experiments were performed at the USPMag lab at the Instituto de Astrono-
 1465 mia, Geofísica e Ciências Atmosféricas (IAG) of the Universidade de São Paulo (USP).
 1466 X-ray diffraction data were collected at the Institute of Energy and Environment (IEE)
 1467 of the University of São Paulo. Special recognition to Dra. Cilene de Medeiro and Dra.
 1468 Ingrid Barcelos, for the assistance provided when collecting SEM-EDS data at the Micro-
 1469 scopic Sample Laboratory, at the Brazilian Synchrotron Light Laboratory (LNLS). Exper-
 1470 iments performed at the CARNAUBA beamline (LNLS) are related to proposal 20220316.
 1471 This work is funded by the São Paulo Research Foundation (FAPESP), grants 21/00861-2,
 1472 22/14100-6 and 16/06114-6. The opinions, hypotheses, and conclusions or recommenda-
 1473 tions expressed in this material are the responsibility of the authors and do not necessarily
 1474 reflect the views of FAPESP. W.W. would like to acknowledge support from the Natural
 1475 Environmental Research Council through grants NE/V001233/1 and NE/S011978/1.

1476 References

- 1477 Abrajewitch, A., & Kodama, K. (2009). Biochemical vs. detrital mechanism of remanence
 1478 acquisition in marine carbonates: A lesson from the k-t boundary interval. *Earth*
 1479 *Planet. Sci. Lett*, *286*(1–2), 269–277. doi: 10.1016/j.epsl.2009.06.035.
- 1480 Aldana, M., Costanzo-Álvarez, V., Gómez, L., González, C., Díaz, M., Silva, P., & Rada,
 1481 M. (2011). Identification of magnetic minerals related to hydrocarbon authigenesis
 1482 in venezuelan oil fields using an alternative decomposition of isothermal remanence
 1483 curves. *Studia Geophysica et Geodaetica*, *55*, 343–358. doi: 10.1007/s11200-011-0019
 1484 -0
- 1485 Alkmim, F., Marshak, S., Pedrosa-Soares, A., Peres, G., Cruz, S., & Whittington, A.
 1486 (2006). Kinematic evolution of the araquai-west congo orogen in brazil and africa:
 1487 Nutcracker tectonics during the neoproterozoic assembly of gondwana. *Precambrian*
 1488 *Res*, *149*(1–2), 43–64. Retrieved from [https://doi.org/10.1016/j.precamres](https://doi.org/10.1016/j.precamres.2006.06.007)
 1489 [.2006.06.007](https://doi.org/10.1016/j.precamres.2006.06.007). doi: 10.1016/j.precamres.2006.06.007.
- 1490 Almeida, F., Amaral, G., Cordani, U., & Kawashita, K. (1973). The precambrian evolution
 1491 of the south america cratonic margin south of the amazon river. In *The ocean basins*
 1492 *and margins* (p. 411–446). New York: Plenum Publishing.
- 1493 Alvarenga, C. (1990). Phénomènes sédimentaires, structuraux et circulation de fluides
 1494 développés à la transition chaicirc;ne-craton. exemple de la chaîne paraguay d'âge
 1495 protérozoïque supérieur, mato grosso, brésil. In *Univ. Aix-Marseille III*.
- 1496 Alvarenga, C., & Trompette, R. (1992). Glacially influenced sedimentation in the later
 1497 proterozoic of the paraguay belt (mato grosso, brazil. *Palaeogeogr. Palaeoclimatol.*
 1498 *Palaeoecol*, *92*(1–2), 85–105. doi: 10.1016/0031-0182(92)90136-S.
- 1499 Aster, R., Borchers, B., & Thurber, C. (2013). Nonlinear regression. In *Parameter estima-*
 1500 *tion and inverse problems* (p. 217–238). Elsevier.

- 1501 Aubourg, C., Jackson, M., Ducoux, M., & Mansour, M. (2019). Magnetite-out and
 1502 pyrrhotite-in temperatures in shales and slates. *Terra Nova*, *31*(6), 534-539.
 1503 Retrieved from <https://onlinelibrary.wiley.com/doi/abs/10.1111/ter.12424>
 1504 doi: <https://doi.org/10.1111/ter.12424>
- 1505 Babinski, M., Liu, D., Trindade, R., Neves, B., & Santos, R. (2004). *U–pb shrimp ages of*
 1506 *detrital zircons from the bebedouro formation, northeast brazil: constraints on sediment*
 1507 *provenance and depositional age of neoproterozoic glacial rocks of the são francisco*
 1508 *craton*.
- 1509 Babinski, M., Vieira, L., & Trindade, R. (2007). Direct dating of the sete lagoas cap car-
 1510 bonate (bambuí group, brazil) and implications for the neoproterozoic glacial events.
 1511 *Terra Nov*, *19*(6), 401–406,. doi: 10.1111/j.1365-3121.2007.00764.x.
- 1512 Bachtadse, V., Voo, R., & Hälbig, I. (1987). Paleomagnetism of the western cape fold
 1513 belt, south africa, and its bearing on the paleozoic apparent polar wander path for
 1514 gondwana. *Earth Planet. Sci. Lett*, *84*(4), 487–499,. doi: 10.1016/0012-821X(87)
 1515 90013-6.
- 1516 Banerjee, S., Elmore, R. D., & Engel, M. H. (1997). Chemical remagnetization and burial
 1517 diagenesis: Testing the hypothesis in the pennsylvanian belden formation, colorado.
 1518 *Journal of Geophysical Research: Solid Earth*, *102*(B11), 24825-24842. Retrieved from
 1519 <https://agupubs.onlinelibrary.wiley.com/doi/abs/10.1029/97JB01893> doi:
 1520 <https://doi.org/10.1029/97JB01893>
- 1521 Bellon, U., Trindade, R., & Williams, W. (2023). Unmixing of magnetic hysteresis
 1522 loops through a modified gamma-cauchy exponential model. *Geochemistry, Geophys.*
 1523 *Geosystems*, *24*, 1–21,. doi: 10.1029/2023GC011048.
- 1524 Bellon, U. D., Williams, W., Trindade, R., Galante, D., Sant’Anna, L., & Pescarini,
 1525 T. (2023). Magnetic properties and chemical analysis of remagnetised carbonates
 1526 of south america [dataset]. *Zenodo*. Retrieved from [https://doi.org/10.5281/](https://doi.org/10.5281/zenodo.10283417)
 1527 [zenodo.10283417](https://doi.org/10.5281/zenodo.10283417) doi: 10.5281/zenodo.10283417
- 1528 Benthien, R., & Elmore, R. (1987). Origin of magnetization in the phosphoria formation
 1529 at sheep mountain, wyoming: a possible relationship with hydrocarbons. *Geophys-*
 1530 *ical Research Letters*, *14*(4), 323–326. Retrieved from [https://doi.org/10.1029/](https://doi.org/10.1029/GL014i004p00323)
 1531 [GL014i004p00323](https://doi.org/10.1029/GL014i004p00323) doi: 10.1029/GL014i004p00323
- 1532 Braun, J. (2010). The many surface expressions of mantle dynamics. *Nat. Geosci*, *3*(12),
 1533 825–833,. doi: 10.1038/ngeo1020.
- 1534 Brigatti, M. F., Galán, E., & Theng, B. K. G. (2013). Structure and Mineralogy of Clay
 1535 Minerals. In *Developments in clay science* (Vol. 5, pp. 21–81). Retrieved from
 1536 <https://linkinghub.elsevier.com/retrieve/pii/B978008098258800002X> doi:
 1537 [10.1016/B978-0-08-098258-8.00002-X](https://doi.org/10.1016/B978-0-08-098258-8.00002-X)
- 1538 Brothers, L., Engel, M., & Elmore, R. (1996). The late diagenetic conversion of
 1539 pyrite to magnetite by organically complexed ferric iron. *Chemical Geology*, *130*(1),
 1540 1-14. Retrieved from [https://www.sciencedirect.com/science/article/pii/](https://www.sciencedirect.com/science/article/pii/0009254196000071)
 1541 [0009254196000071](https://www.sciencedirect.com/science/article/pii/0009254196000071) doi: [https://doi.org/10.1016/0009-2541\(96\)00007-1](https://doi.org/10.1016/0009-2541(96)00007-1)
- 1542 Butler, R. (1992). *Paleomagnetism: magnetic domains to geologic terranes, no*.
- 1543 Butler, R., & Banerjee, S. (1975). Theoretical single-domain grain size range in magnetite
 1544 and titanomagnetite [[Online].]. *J. Geophys. Res. Oct*, *80*(29). Retrieved from [http://](http://pilotscholars.up.edu/env_facpubs/17)
 1545 pilotscholars.up.edu/env_facpubs/17. (Available:)
- 1546 Caby, R., & Costa Campos Neto, M. (2022). Basement domes in a greenschist facies context:
 1547 Tectono-metamorphic evolution of the southern quadrilátero ferrífero, southeast brazil.
 1548 *Tectonophysics*, *828*(February), 229280,. (p.) doi: 10.1016/j.tecto.2022.229280.
- 1549 Callaway, W., & McAtee, J. (1985). Magnetic susceptibilities of representative smectites.
 1550 *Am. Mineral*, *70*(9–10), 996–1003,.
- 1551 Carvallo, C., Muxworthy, A., & Dunlop, D. (2006). First-order reversal curve (forc) diagrams
 1552 of magnetic mixtures: Micromagnetic models and measurements. *Phys. Earth Planet.*
 1553 *Inter*, *154*(3–4), 308–322,. doi: 10.1016/j.pepi.2005.06.017.
- 1554 Carvallo, C., Özdemir, O., & Dunlop, D. (2004). First-order reversal curve (forc) diagrams
 1555 of elongated single-domain grains at high and low temperatures. *J. Geophys. Res.*

- 1556 *Solid Earth*, 109(4). doi: 10.1029/2003JB002539.
- 1557 Chang, L. (2013). Low-temperature magnetic properties of pelagic carbonates: Oxidation of
1558 biogenic magnetite and identification of magnetosome chains. *J. Geophys. Res. Solid*
1559 *Earth*, 118(12), 6049–6065,. doi: 10.1002/2013JB010381.
- 1560 Chang, L. (2014). Magnetic detection and characterization of biogenic magnetic minerals:
1561 A comparison of ferromagnetic resonance and first-order reversal curve diagrams. *J.*
1562 *Geophys. Res. Solid Earth*, 119(8), 6136–6158,. doi: 10.1002/2014JB011213.
- 1563 Chemale, J., Alkmin, F., & Endo, I. (1993). Late proterozoic tectonism in the interior of
1564 the são francisco craton. In tion & H. Dispersal (Eds.), *Gondwana eight —assembly*
1565 *evolu* (p. 29–42). Balkema, Rotterdam.
- 1566 Costanzo-Álvarez, V., Rapalini, A., Aldana, M., Díaz, M., Kietzmann, D., & Iglesia-
1567 Llanos, M. (2019). A combined rock-magnetic and epr study about the effects of
1568 hydrocarbon-related diagenesis on the magnetic signature of oil shales (vacca muerta
1569 formation, southwestern argentina. *Journal of Petroleum Science and Engineer-*
1570 *ing*, 173(September 2018), 861–879. Retrieved from [https://doi.org/10.1016/](https://doi.org/10.1016/j.petrol.2018.10.082)
1571 [j.petrol.2018.10.082](https://doi.org/10.1016/j.petrol.2018.10.082) doi: 10.1016/j.petrol.2018.10.082
- 1572 Couto, D. (2020). Mineralogy composition and texture indicative of fluid-assisted remobi-
1573 lization in carbonate units of the irecê basin, brazil. *J. South Am. Earth Sci*, 110,
1574 103346,. doi: 10.1016/j.jsames.2021.103346.
- 1575 Crouzet, C., Rochette, P., & Ménard, G. (2001, 06). Experimental evaluation of thermal
1576 recording of successive polarities during uplift of metasediments. *Geophysical Journal*
1577 *International*, 145(3), 771–785. Retrieved from [https://doi.org/10.1046/j.0956-](https://doi.org/10.1046/j.0956-540x.2001.01423.x)
1578 [540x.2001.01423.x](https://doi.org/10.1046/j.0956-540x.2001.01423.x) doi: 10.1046/j.0956-540x.2001.01423.x
- 1579 Dannemann, S., Appel, E., Rösler, W., Neumann, U., Liebke, U., & Nag, D. (2022). Palaeo-
1580 magnetic indication for india–asia collision at 12°n and maximum 810 km greater india
1581 extent in the western suture zone. *Geophysical Journal International*, 229, 1193–1211.
1582 Retrieved from <https://doi.org/10.1093/gji/ggab528> doi: 10.1093/gji/ggab528
- 1583 Dardenne, M. (1978). Síntese sobre a estratigrafia do grupo bambuí no brasil central. In
1584 *Anais do xxx congresso brasileiro de geologia* (p. 597–610).
- 1585 Davidson, M., Egger, J., Elmore, R., Engel, M., Woods, S., & Abraham, M. (2000). Orogenic
1586 fluids and secondary magnetizations : testing the relationship in the south wales
1587 coalfield foreland basin. *Journal of Geochemical Exploration*, 70, 581–584.
- 1588 Day, R., Fuller, M., & Schmidt. (1977). Hysteresis properties of titanomagnetites: grain-
1589 size and compositional dependence. *Physics of the Earth and Planetary Interiors*, 13,
1590 260–267. doi: [https://doi.org/10.1016/0031-9201\(77\)90108-X](https://doi.org/10.1016/0031-9201(77)90108-X)
- 1591 Dearing, J. (1996). Frequency-dependent susceptibility measurements of environmental
1592 materials. *Geophys. J. Int*, 124(1), 228–240,. doi: 10.1111/j.1365-246X.1996.tb06366
1593 .x.
- 1594 Duncan, D. (2018). Synchrotron-based spectroscopy in on-surface polymerization of covalent
1595 networks. In *Encyclopedia of interfacial chemistry* (p. 436–445). Surface Science and
1596 Electrochemistry, Elsevier.
- 1597 Dunlop, D. (2002). Theory and application of the day plot (m_{rs} / m_s versus h_{cr} / h_c)
1598 1. theoretical curves and tests using titanomagnetite data. *J. Geophys. Res*, 107(B3).
1599 (p. 2056,) doi: 10.1029/2001JB000486.
- 1600 Dunlop, D., & Özdemir, O. (1997). *Rock magnetism: Fundamentals and frontiers* (1st ed.).
1601 Cambridge: Cambridge University Press.
- 1602 Dunlop, D., Özdemir, O., Clark, D., & Schmidt, P. (2000). Time–temperature relations for
1603 the remagnetization of pyrrhotite (fe₇s₈) and their use in estimating paleotempera-
1604 tures. *Earth Planet. Sci. Lett*, 176(1), 107–116,. doi: 10.1016/S0012-821X(99)00309
1605 -X.
- 1606 Duverger, A., Berg, J., Busigny, V., Guyot, F., Bernard, S., & Miot, J. (2020). Mechanisms
1607 of pyrite formation promoted by sulfate-reducing bacteria in pure culture. *Front. Earth*
1608 *Sci*, 8(November), 1–15,. doi: 10.3389/feart.2020.588310.
- 1609 D’Agrella-Filho, M. (1995). Paleomagnetism of carbonatic sedimentary sequences of the
1610 salitre formation, chapada diamantina—bahia. In *4th in. cong* (p. 262–265). Sociedade

- 1611 Brasileira de Geofísica.
- 1612 D'Agrella-Filho, M., Babinski, M., Trindade, R., Schmus, W., & Ernesto, M. (2000).
 1613 Simultaneous remagnetization and u–pb isotope resetting in neoproterozoic carbon-
 1614 ates of the são francisco craton, brazil. *Precambrian Res*, *99*(3–4), 179–196,. doi:
 1615 10.1016/S0301-9268(99)00059-5.
- 1616 D'Agrella-Filho, M., Irene, M., Raposo, B., & Egydio-silva, M. (2004). Paleomagnetic study
 1617 of the juiz de fora complex, se brazil: Implications for gondwana. *Gondwana Res*, *7*(I),
 1618 103–113,.
- 1619 D'Agrella-Filho, M., & Pacca, I. (1986). Paleomagnetism of metamorphic rocks from the
 1620 piquete region-ribeira valley, southeastern brazil. *Rev. Bras. Geociências*, *4*, 79–84,.
- 1621 Egli, R. (2003). Analysis of the field dependence of remanent magnetization curves. *J.*
 1622 *Geophys. Res. Solid Earth*, *108*(B2), 1–25,. doi: 10.1029/2002jb002023.
- 1623 Egli, R. (2013). Variforc: An optimized protocol for calculating non-regular first-order
 1624 reversal curve (forc) diagrams. *Glob. Planet. Change*, *110*, 302–320,. Retrieved from
 1625 <https://doi.org/10.1016/j.gloplacha.2013.08.003>. doi: 10.1016/j.gloplacha
 1626 .2013.08.003.
- 1627 Egli, R., Chen, A., Winklhofer, M., Kodama, K., & Horng, C.-S. (2010). Detection of
 1628 noninteracting single domain particles using first-order reversal curve diagrams. *Geo-*
 1629 *chemistry, Geophys. Geosystems*, *11*(1), –. doi: 10.1029/2009GC002916.
- 1630 Elmore, R., Engel, M., Crawford, L., Nick, K., Imbus, S., & Sofer, Z. (1987). Evi-
 1631 dence for a relationship between hydrocarbons and authigenic magnetite. *Nature*,
 1632 *325*(6103), 428–430. Retrieved from <https://doi.org/10.1038/325428a0> doi:
 1633 10.1038/325428a0
- 1634 Elmore, R. D., Muxworthy, A. R., & Aldana, M. (2012). Remagnetization and chemical
 1635 alteration of sedimentary rocks. *Geological Society of London*, *371*, 1–21.
- 1636 Emmerton, S., Muxworthy, A., Sephton, M., Aldana, M., Costanzo-Alvarez, V., Bayona, G.,
 1637 & Williams, W. (2013). Correlating biodegradation to magnetization in oil bearing
 1638 sedimentary rocks. *Geochimica et Cosmochimica Acta*, *112*, 146–165. Retrieved from
 1639 <https://doi.org/10.1016/j.gca.2013.03.008> doi: 10.1016/j.gca.2013.03.008
- 1640 Evans, M. E., & Heller, F. (2003). *Environmental Magnetism: Principles and Applications*
 1641 *of Enviromagnetic*. Academic Press. doi: 10.1007/978-1-4020-4423-6_95
- 1642 Figueiredo, F., Almeida, R., Tohver, E., Babinski, M., Liu, D., & Fanning, C. (2009). Neo-
 1643 proterozoic glacial dynamics revealed by provenance of diamictites of the bebedouro
 1644 formation, são francisco craton, central eastern brazil. *Terra Nov*, *21*(5), 375–385,.
 1645 doi: 10.1111/j.1365-3121.2009.00893.x.
- 1646 Fonseca, A., Novo, T., Nachtergaele, S., Fonte-Boa, T., Ranst, G., & Grave, J. (2021).
 1647 Differential phanerozoic evolution of cratonic and non-cratonic lithosphere from a
 1648 thermochronological perspective: São francisco craton and marginal orogens (brazil).
 1649 *Gondwana Res*, *93*, 106–126,. doi: 10.1016/j.gr.2021.01.006.
- 1650 Fonseca, A., Piffer, G., Nachtergaele, S., Ranst, G., Grave, J., & Novo, T. (2020). Devonian
 1651 to permian post-orogenic denudation of the brasília belt of west gondwana: insights
 1652 from apatite fission track thermochronology. *J. Geodyn*, *137*(March), 101733,. (p.)
 1653 doi: 10.1016/j.jog.2020.101733.
- 1654 Font, E., Rapalini, A. E., Tomezzoli, R. N., Trindade, R. I. F., & Tohver, E. (2012). Episodic
 1655 remagnetizations related to tectonic events and their consequences for the south amer-
 1656 ica polar wander path. *Geological Society, London, Special Publications*, *371*(1), 55-
 1657 87. Retrieved from <https://www.lyellcollection.org/doi/abs/10.1144/SP371.7>
 1658 doi: 10.1144/SP371.7
- 1659 Font, E., Trindade, R., & Nédélec, A. (2005). Detrital remanent magnetization in haematite-
 1660 bearing neoproterozoic puga cap dolostone, amazon craton: A rock magnetic and sem
 1661 study. *Geophys. J. Int*, *163*(2), 491–500,. doi: 10.1111/j.1365-246X.2005.02776.x.
- 1662 Font, E., Trindade, R., & Nédélec, A. (2006). Remagnetization in bituminous limestones
 1663 of the neoproterozoic araras group (amazon craton): Hydrocarbon maturation, burial
 1664 diagenesis, or both? *J. Geophys. Res. Solid Earth*, *111*(6), 1–17,. doi: 10.1029/
 1665 2005JB004106.

- 1666 Franceschinis, P., Rapalini, A., Escayola, M., & Picada, C. (2019). Paleogeographic and tec-
 1667 tonic evolution of the pampia terrane in the cambrian: New paleomagnetic constraints.
 1668 *Tectonophysics*, 779, 228386,. doi: 10.1016/j.tecto.2020.228386.
- 1669 Fruit, D., Elmore, R. D., & Halgedahl, S. (1995). Remagnetization of the folded belden for-
 1670 mation, northwest colorado. *Journal of Geophysical Research: Solid Earth*, 100(B8),
 1671 15009-15023. Retrieved from [https://agupubs.onlinelibrary.wiley.com/doi/](https://agupubs.onlinelibrary.wiley.com/doi/abs/10.1029/95JB00045)
 1672 [abs/10.1029/95JB00045](https://doi.org/10.1029/95JB00045) doi: <https://doi.org/10.1029/95JB00045>
- 1673 Gaucher, C., Boggiani, P., Sprechmann, P., Sial, A., & Fairchild, T. (2003). Integrated cor-
 1674 relation of the vendian to cambrian arroyo del soldado and corumbá groups (uruguay
 1675 and brazil): palaeogeographic, palaeoclimatic and palaeobiologic implications. *Pre-*
 1676 *cambrian Res*, 120(3-4), 241-278,. doi: 10.1016/S0301-9268(02)00140-7.
- 1677 Ge, K., Williams, W., Nagy, L., & Tauxe, L. (2021). Models of maghematization: Ob-
 1678 servational evidence in support of a magnetic unstable zone. *Geochemistry, Geophys.*
 1679 *Geosystems*, 22(3), 1-12,. doi: 10.1029/2020GC009504.
- 1680 Geiss, C., Egli, R., & Zanner, C. (2008). Direct estimates of pedogenic magnetite as a tool
 1681 to reconstruct past climates from buried soils. *J. Geophys. Res*, 113(B11), 11102,.
 1682 doi: 10.1029/2008JB005669.
- 1683 Golovanova, I. V., Danukalov, K. N., Salmanova, R. Y., Levashova, N. M., Parfiriev,
 1684 N. P., Sergeeva, N. D., & Meert, J. G. (2023, jul). Magnetic field hyperactivity
 1685 during the early Neoproterozoic: A paleomagnetic and cyclostratigraphic study
 1686 of the Katav Formation, southern Urals, Russia. *Geoscience Frontiers*, 14(4),
 1687 101558. Retrieved from [https://www.sciencedirect.com/science/article/](https://www.sciencedirect.com/science/article/pii/S1674987123000257)
 1688 [pii/S1674987123000257](https://linkinghub.elsevier.com/retrieve/pii/S1674987123000257)[https://linkinghub.elsevier.com/retrieve/pii/](https://linkinghub.elsevier.com/retrieve/pii/S1674987123000257)
 1689 [S1674987123000257](https://linkinghub.elsevier.com/retrieve/pii/S1674987123000257) doi: 10.1016/j.gsf.2023.101558
- 1690 Goscombe, B., Foster, D., Gray, D., & Wade, B. (2018). The evolution of the damara oro-
 1691 genic system: A record of west gondwana assembly and crustal response. In S. Sieges-
 1692 mund, B. S., O. M., & O. P. (Eds.), *Geology of southwest gondwana* (p. 303-352).
 1693 Springer.
- 1694 Grotzinger, J. P., & James, N. P. (2000). Precambrian carbonates: evolution of understad-
 1695 ing. In J. P. Grotzinger & N. P. James (Eds.), *Carbonate sedimentation and diagenesis*
 1696 *in the evolving precambrian world* (pp. 3-20). Tulsa, Oklahoma, U.S.A: Society for
 1697 Sedimentary Geology.
- 1698 Guacaneme, C., Babinski, M., Paula-Santos, G., & Pedrosa-Soares, A. (2017). C, o, and
 1699 sr isotopic variations in neoproterozoic-cambrian carbonate rocks from sete lagoas
 1700 formation (bambuí group), in the southern são francisco basin, brazil. *Brazilian J.*
 1701 *Geol*, 47(3), 521-543,. doi: 10.1590/2317-4889201720160126.
- 1702 Guimarães, G., Pierosan, R., & Ruiz, A. (2017). Geologia e petrologia do granito são
 1703 vicente na região do parque estadual Águas quentes, estado de mato grosso, brasil.
 1704 *Geol. USP. Série Científica*, 17(3), 29,. doi: 10.11606/issn.2316-9095.v17-426.
- 1705 Gunasekaran, S., & Anbalagan, G. (2007). Thermal decomposition of natural dolomite.
 1706 *Bull. Mater. Sci*, 30(4), 339-344,. doi: 10.1007/s12034-007-0056-z.
- 1707 Haldar, S., & Tišljár, J. (2014). Sedimentary rocks. *Introduction to Mineralogy and Petrol-*
 1708 *ogy*, 3(C), 121-212.
- 1709 Harrison, R., Muraszko, J., Heslop, D., Lascu, I., Muxworthy, A., & Roberts, A. (2018). An
 1710 improved algorithm for unmixing first-order reversal curve diagrams using principal
 1711 component analysis. *Geochem. Geophys. Geosyst*, 19, 1595-1610,.
- 1712 Henderson, C., Cressey, G., & Redfern, S. (1995). Geological applications of synchrotron
 1713 radiation. *Radiat. Phys. Chem*, 45(3), 459-481,. doi: 10.1016/0969-806X(95)92799-5.
- 1714 Heslop, D. (2020). An automatic model selection-based machine learning framework to
 1715 estimate forc distributions. *J. Geophys. Res. Solid Earth*, 125(10), 1-16,. doi: 10.1029/
 1716 2020JB020418.
- 1717 Hirt, A. M., Banin, A., & Gehring, A. U. (1993, 12). Thermal generation of ferromagnetic
 1718 minerals from iron-enriched smectites. *Geophysical Journal International*, 115(3),
 1719 1161-1168. Retrieved from [https://doi.org/10.1111/j.1365-246X.1993.tb01518](https://doi.org/10.1111/j.1365-246X.1993.tb01518.x)
 1720 [.x](https://doi.org/10.1111/j.1365-246X.1993.tb01518.x) doi: 10.1111/j.1365-246X.1993.tb01518.x

- 1721 Hrouda, F. (2011). Models of frequency-dependent susceptibility of rocks and soils revisited
1722 and broadened. *Geophys. J. Int.*, *187*(3), 1259–1269,. doi: 10.1111/j.1365-246X.2011
1723 .05227.x.
- 1724 Hrouda, F., Pokorný, J., Ježek, J., & Chadima, M. (2013). Out-of-phase magnetic suscep-
1725 tibility of rocks and soils: A rapid tool for magnetic granulometry. *Geophys. J. Int.*,
1726 *194*(1), 170–181,. doi: 10.1093/gji/ggt097.
- 1727 Hu, G., Dam-Johansen, K., Wedel, S., & Hansen, J. (2006). Decomposition and oxidation of
1728 pyrite. *Prog. Energy Combust. Sci.*, *32*(3), 295–314,. doi: 10.1016/j.pecs.2005.11.004.
- 1729 Hu, J., Zhang, Y., Jia, D., Muxworthy, A., Selby, D., & Li, Y. (2023). Combining paleo-
1730 omagnetic and re-os isotope data to date hydrocarbon generation and accumulation
1731 processes. *Journal of Geophysical Research: Solid Earth*, *128*(2). Retrieved from
1732 <https://doi.org/10.1029/2022JB025955> doi: 10.1029/2022JB025955
- 1733 Huang, W., Lippert, P., Jackson, M., Dekkers, M., Zhang, Y., Li, J., ... Hinsbergen,
1734 D. (2017). Remagnetization of the paleogene tibetan himalayan carbonate rocks
1735 in the gamba area: Implications for reconstructing the lower plate in the india-asia
1736 collision. *Journal of Geophysical Research: Solid Earth*, *122*, 808–825. Retrieved from
1737 <https://doi.org/10.1002/2016JB013662> doi: 10.1002/2016JB013662
- 1738 Huggett, J. M. (2005). Sedimentary Rocks — Clays and Their Diagenesis. In *Encyclopedia of*
1739 *geology* (pp. 62–70). Elsevier. Retrieved from [https://linkinghub.elsevier.com/](https://linkinghub.elsevier.com/retrieve/pii/B0123693969003117)
1740 [retrieve/pii/B0123693969003117](https://linkinghub.elsevier.com/retrieve/pii/B0123693969003117) doi: 10.1016/B0-12-369396-9/00311-7
- 1741 Jaboyedoff, M., Bussy, F., Kübler, B., & Thelin, P. (2001). Illite ‘crystallinity’ revisited.
1742 *Clays Clay Miner.*, *49*(2), 156–167,. doi: 10.1346/CCMN.2001.0490205.
- 1743 Jackson, M. (1990). Diagenetic sources of stable remanence in remagnetized paleozoic
1744 cratonic carbonates: a rock magnetic study. *J. Geophys. Res.*, *95*(B3), 2753–2761,.
1745 doi: 10.1029/JB095iB03p02753.
- 1746 Jackson, M., & Sun, W. (1992). The rock magnetic fingerprint of chemical remagnetization
1747 in midcontinental paleozoic carbonates. *Geophys. Res. Lett.*, *19*(8), 781–784,.
- 1748 Jackson, M., & Swanson-Hysell, N. (2012). Rock magnetism of remagnetized carbonate
1749 rocks: Another look. *Geol. Soc. Spec. Publ.*, *371*(1), 229–251,. doi: 10.1144/SP371.3.
- 1750 Jiao, W., Li, Y., Yang, Z., & Liu, J. (2019). A widespread early mesozoic remagnetization
1751 in south china. *Journal of Geophysical Research: Solid Earth*, *124*, 88–103. Retrieved
1752 from <https://doi.org/10.1029/2018JB016707> doi: 10.1029/2018JB016707
- 1753 Júnior, G., Nogueira, A., Neto, E., Moura, C., Araújo, B., & Reis, F. (2016). Organic
1754 matter in the neoproterozoic cap carbonate from the amazonian craton, brazil. *J.*
1755 *South Am. Earth Sci.*, *72*, 7–24,. doi: 10.1016/j.jsames.2016.07.012.
- 1756 Kars, M., Aubourg, C., Pozzi, J., & Janots, D. (2012). Continuous production of nanosized
1757 magnetite through low grade burial. *Geochemistry, Geophys. Geosystems*, *13*(8), – .,
1758 doi: 10.1029/2012GC004104.
- 1759 Karunadasa, K., Manoratne, C., Pitawala, H., & Rajapakse, R. (2019). Thermal de-
1760 composition of calcium carbonate (calcite polymorph) as examined by in-situ high-
1761 temperature x-ray powder diffraction. *J. Phys. Chem. Solids*, *134*(May), 21–28,. doi:
1762 10.1016/j.jpcs.2019.05.023.
- 1763 Kennedy, M. J., Pevear, D. R., & Hill, R. J. (2002). Mineral surface control of organic
1764 carbon in black shale. *Science*, *295*(5555), 657-660. Retrieved from [https://www](https://www.science.org/doi/abs/10.1126/science.1066611)
1765 [.science.org/doi/abs/10.1126/science.1066611](https://www.science.org/doi/abs/10.1126/science.1066611) doi: 10.1126/science.1066611
- 1766 Klopogge, J. T., Komarneni, S., & Amonette, J. E. (1999). Synthesis of smectite clay
1767 minerals: A critical review. *Clays and Clay Minerals*, *47*(5), 529–554. doi: 10.1346/
1768 CCMN.1999.0470501
- 1769 Kübler, B. (1964). Les argiles indicateurs de métamorphisme. *Rev. Inst. Français du*
1770 *Pétrole*, *29*, 1096–1113,.
- 1771 Kübler, B. (1967). La cristallinité de l’illite et les zones tout à fait supérieures du
1772 métamorphisme. In *Etages tectoniques, colloque de neuchâtel* (p. 105–121).
- 1773 Kübler, B. (1968). Evaluation quantitative du métamorphisme par cristallinité de l’illite.
1774 *Bull. Cent. Rech. Pau SNPA*, *2*, 385–397,.

- 1775 Kübler, B. (1990). ‘cristallinité’ de l’illite et mixed-layer: Brève révision. *Schweizerische*
1776 *Mineral. Petrophische Mitteilungen*, *70*, 89–93,.
- 1777 Labus, M. (2020). Pyrite thermal decomposition in source rocks. *Fuel*, *287*, 119529,. doi:
1778 10.1016/j.fuel.2020.119529.
- 1779 Lanson, B., Sakharov, B. A., Claret, F., & Drits, V. A. (2009). Diagenetic smectite-to-
1780 illite transition in clay-rich sediments: A reappraisal of x-ray diffraction results using
1781 the multi-specimen method. *American Journal of Science*, *309*(6), 476–516. doi:
1782 10.2475/06.2009.03
- 1783 Lascu, I., Einsle, J., Ball, M., & Harrison, R. (2018). The vortex state in geologic materials:
1784 A micromagnetic perspective. *J. Geophys. Res. Solid Earth*, *123*(9), 7285–7304,. doi:
1785 10.1029/2018JB015909.
- 1786 Leahy, J., & Colwell, R. (1990). Microbial degradation of hydrocarbons in the environment.
1787 *Microbiological Reviews*, *54*(3), 305–315.
- 1788 Lennie, A., England, K., & Vaughan, D. (1995). Transformation of synthetic mackinawite
1789 to hexagonal pyrrhotite; a kinetic study. *Am. Mineral*, *80*(9–10), 960–967,. doi:
1790 10.2138/am-1995-9-1012.
- 1791 Levi, S. (2007). Magnetization, Chemical Remanent (CRM). In D. Gubbins & E. Herrero-
1792 Bervera (Eds.), *Encyclopedia of geomagnetism and paleomagnetism* (pp. 580–588).
1793 Dordrecht: Springer Netherlands. Retrieved from [https://doi.org/10.1007/978-1-](https://doi.org/10.1007/978-1-4020-4423-6_190)
1794 [4020-4423-6_190](https://doi.org/10.1007/978-1-4020-4423-6_190) doi: 10.1007/978-1-4020-4423-6_190
- 1795 Liu, Q., Roberts, A. P., Larrasoana, J. C., Banerjee, S. K., Guyodo, Y., Tauxe, L., &
1796 Oldfield, F. (2012). Environmental magnetism: Principles and applications. *Reviews*
1797 *of Geophysics*, *50*(4). doi: <https://doi.org/10.1029/2012RG000393>
- 1798 Lowrie, W. (1990). Identification of ferromagnetic minerals in a rock by coercivity and
1799 unblocking temperature properties. *Geophys. Res. Lett*, *17*(2), 159–162,. doi: 10.1029/
1800 GL017i002p00159.
- 1801 Machel, H. (2001). Bacterial and thermochemical sulfate reduction in diagenetic settings
1802 — old and new insights. *Sediment. Geol*, *140*(1–2), 143–175,. doi: 10.1016/S0037
1803 -0738(00)00176-7.
- 1804 Martín-Hernández, F., & Hirt, A. (2003). The anisotropy of magnetic susceptibility in
1805 biotite, muscovite and chlorite single crystals. *Tectonophysics*, *367*(1–2), 13–28,. doi:
1806 10.1016/S0040-1951(03)00127-6.
- 1807 Matamoros-Veloza, A. (2018). A highly reactive precursor in the iron sulfide system. *Nat.*
1808 *Commun*, *9*(1), 3125,. doi: 10.1038/s41467-018-05493-x.
- 1809 Maxbauer, D., Feinberg, J., & Fox, D. (2016). Max unmix: A web application for unmixing
1810 magnetic coercivity distributions. *Comput. Geosci*, *95*, 140–145,. doi: 10.1016/j.cageo
1811 .2016.07.009.
- 1812 McCabe, C., & Elmore, R. (1989). The occurrence and origin of late paleozoic remagnetiza-
1813 tion in the sedimentary rocks of north america. *Reviews of Geophysics*, *27*, 471–494.
1814 doi: 10.1029/RG027i004p00471
- 1815 McCabe, C., Sassen, R., & Saffer, B. (1987). Occurrence of secondary magnetite within
1816 biodegraded oil. *Geology*, *15*(1), 7. Retrieved from [https://doi.org/10.1130/0091-](https://doi.org/10.1130/0091-7613(1987)15)
1817 [7613\(1987\)15](https://doi.org/10.1130/0091-7613(1987)15) doi: 10.1130/0091-7613(1987)15
- 1818 McCabe, C., Voo, R., Peacor, D., Scotese, C., & Freeman, R. (1983). Diagenetic magnetite
1819 carries ancient yet secondary remanence in some paleozoic sedimentary carbonates.
1820 *Geology*, *11*, 221–223. Retrieved from [https://doi.org/10.1130/0091-7613\(1983\)](https://doi.org/10.1130/0091-7613(1983)11)
1821 [11](https://doi.org/10.1130/0091-7613(1983)11) doi: 10.1130/0091-7613(1983)11
- 1822 Merdith, A. S., Williams, S. E., Collins, A. S., Tetley, M. G., Mulder, J. A., Blades, M. L.,
1823 ... Müller, R. D. (2021, mar). Extending full-plate tectonic models into deep time:
1824 Linking the Neoproterozoic and the Phanerozoic. *Earth-Science Reviews*, *214*, 103477.
1825 doi: 10.1016/j.earscirev.2020.103477
- 1826 Miller, J., & Kent, D. (1988). Regional trends in the timing of alleghanian remagnetization
1827 in the appalachians. *Geology*, *16*, 588–591.
- 1828 Misi, A., Azmy, K., Kaufman, A., Oliveira, T., Sanches, A., & Oliveira, G. (2014). Review of
1829 the geological and geochronological framework of the vazante sequence, minas gerais,

- 1830 brazil: Implications to metallogenic and phosphogenic models. *Ore Geol. Rev.*, *63*,
1831 76–90,. doi: 10.1016/j.oregeorev.2014.05.002.
- 1832 Misi, A., & Kyle, J. (1994). Upper proterozoic carbonate stratigraphy, diagenesis,
1833 and stromatolitic phosphorite formation, irece basin, bahia, brazil. *J. Sediment.*
1834 *Res. A Sediment. Petrol. Process*(2), 299–310,. doi: 10.1306/d4267d84-2b26-11d7
1835 -8648000102c1865d.
- 1836 Misi, A., & Veizer, J. (1998). Neoproterozoic carbonate sequences of the una group, irecê
1837 basin, brazil: chemostratigraphy, age and correlations. *Precambrian Res.*, *89*(1–2),
1838 87–100,. doi: 10.1016/S0301-9268(97)00073-9.
- 1839 Mohriak, W., & Fainstein, R. (2012). Phanerozoic regional geology of the eastern brazilian
1840 margin. In *Regional geology and tectonics: Phanerozoic passive margins, cratonic*
1841 *basins and global tectonic maps* (p. 222–282). Elsevier.
- 1842 Morad, S. (1978). Feldspars in sedimentary rocks. In *Sedimentology* (p. 452–457). Berlin,
1843 Heidelberg: Springer.
- 1844 Moreira, D., Uhlein, A., Dussin, I., Uhlein, G., & Misuzaki, A. (2020). A cambrian age for the
1845 upper bambuí group, brazil, supported by the first u-pb dating of volcanoclastic bed. *J.*
1846 *South Am. Earth Sci.*, *99*(January), 102503,. (p.) doi: 10.1016/j.jsames.2020.102503.
- 1847 Muxworthy, A., & Dunlop, D. (2002). First-order reversal curve (forc) diagrams for
1848 pseudo-single-domain magnetites at igh temperature. *Earth Planet. Sci. Lett.*, *203*(1),
1849 369–382,. doi: 10.1016/S0012-821X(02)00880-4.
- 1850 Mählmann, R., & Frey, M. (2012). Standardisation, calibration and correlation of the
1851 kübler-index and the vitrinite/bituminite reflectance: an inter-laboratory and field
1852 related study. *Swiss J. Geosci.*, *105*(2), 153–170,. doi: 10.1007/s00015-012-0110-8.
- 1853 Nagata, T. (1961). *Rock Magnetism*. Tokyo: Maruzen Company Ltd.
- 1854 Nagy, L. (2017). Stability of equidimensional pseudo–single-domain magnetite over billion-
1855 year timescales. *Proc. Natl. Acad. Sci. U. S. A.*, *114*(39), 10356–10360,. doi: 10.1073/
1856 pnas.1708344114.
- 1857 Nagy, L., Williams, W., Tauxe, L., & Muxworthy, A. (2019). From nano to micro: Evolution
1858 of magnetic domain structures in multidomain magnetite. *Geochemistry, Geophys.*
1859 *Geosystems*, *20*(6), 2907–2918,. doi: 10.1029/2019GC008319.
- 1860 Nagy, L., Williams, W., Tauxe, L., Muxworthy, A., & Ferreira, I. (2019). Thermomagnetic
1861 recording fidelity of nanometer-sized iron and implications for planetary magnetism.
1862 *Proc. Natl. Acad. Sci.*, *116*(6), 1984–1991,. doi: 10.1073/pnas.1810797116.
- 1863 Néel, L. (1955). Some theoretical aspects of rock-magnetism. *Advances in Physics*, *4*(14),
1864 191–243. Retrieved from <https://doi.org/10.1080/00018735500101204> doi: 10
1865 .1080/00018735500101204
- 1866 Ning, J., Zheng, Y., Brown, B., Young, D., & Nesic, S. (2015). Construction and verification
1867 of pourbaix diagrams for hydrogen sulfide corrosion of mild steel. *NACE - Int. Corros.*
1868 *Conf. Ser*(5507), 1–19,.
- 1869 Nogueira, A., & Riccomini, C. (2006). O grupo araras (neoproterozóico) na parte norte da
1870 faixa paraguai e sul do craton amazônico, brasil. *Rev. Bras. Geociências*, *36*(4).
- 1871 Nogueira, A., Riccomini, C., Sial, A., Moura, C., & Fairchild, T. (2003). Soft-sediment de-
1872 formation at the base of the neoproterozoic puga cap carbonate (southwestern amazon
1873 craton, brazil): Confirmation of rapid icehouse to greenhouse transition in snowball
1874 earth. *Geology*, *31*(7), 613–616,. doi: 10.1130/0091-7613(2003)031
- 1875 Oliveira, L., Gonçalves, M., & Tella, V. (2014). *Projeto sirius: a nova fonte de luz síncrotron*
1876 *brasileira*.
- 1877 Ormerod, R. (2001). Surface chemistry: Electron yield spectroscopy. In *Encyclopedia of*
1878 *materials* (p. 9006–9008). Science and Technology, Elsevier.
- 1879 Parry, L. (1982). Magnetization of immobilized particle dispersions with two distinct particle
1880 sizes. *Phys. Earth Planet. Inter.*, *28*(3), 230–241,. doi: 10.1016/0031-9201(82)90004-8.
- 1881 Patarachao, B. (2019). Xrd analysis of illite-smectite interstratification in clays from oil
1882 sands ores. *Adv. X-ray Anal.*, *62*(C), 22–31,.
- 1883 Paula-Santos, G., Babinski, M., Kuchenbecker, M., Caetano-Filho, S., Trindade, R., &
1884 Pedrosa-Soares, A. (2015). New evidence of an ediacaran age for the bambuí group

- 1885 in southern são francisco craton (eastern brazil) from zircon u–pb data and isotope
1886 chemostratigraphy. *Gondwana Res*, 28(2), 702–720,. doi: 10.1016/j.gr.2014.07.012.
- 1887 Pavlov, V., & Gallet, Y. (2005). A third superchron during the early paleozoic. *International*
1888 *Union of Geological Sciences*, 28. doi: 10.18814/epiiugs/2005/v28i2/001
- 1889 Pedrosa-soares, A. (2007). Orógeno araçuai: síntese do conhecimento 30 anos após
1890 almeida 1977. *Geonomos*, 15(1), 1–16,. Retrieved from [https://doi.org/10.18285/
1891 geonomos.v15i1.103](https://doi.org/10.18285/geonomos.v15i1.103). (doi:) doi: 10.18285/geonomos.v15i1.103.
- 1892 Pedrosa-Soares, A. (2020). O orógeno araçuai à luz da geocronologia: um tributo a umberto
1893 cordani. In A. November, W. Teixeira, & B. Neves (Eds.), *Geocronologia e evolução*
1894 *tectônica do continente sul-americano: a contribuição de umberto giuseppe cordani*
1895 (1st ed., p. 250–272). São Paulo: Solaris Edições Culturais.
- 1896 Pedrosa-Soares, A., Cordani, U., & Nutman, A. (2000). Constraining the age of neopro-
1897 terozoic glaciation in eastern brazil: first u-pb (shrimp) data of detrital zircons. *Rev.*
1898 *Bras. Geociências*, 30.
- 1899 Pedrosa-Soares, A., Noce, C., Wiedemann, C., & Pinto, C. (2001). The araçuai-west-
1900 congo orogen in brazil: An overview of a confined orogen formed during gondwanaland
1901 assembly. *Precambrian Res*, 110(1–4), 307–323,. doi: 10.1016/S0301-9268(01)00174
1902 -7.
- 1903 Penner-Hahn, J. (2003). X-ray absorption spectroscopy. In *Comprehensive coordination*
1904 *chemistry* (Vols. II, vol. 2, p. 159–186). Elsevier.
- 1905 Phillips, E. J. P., Lovley, D. R., & Roden, E. E. (1993). Composition of non-microbially
1906 reducible fe(iii) in aquatic sediments. *Applied and Environmental Microbiology*, 59(8),
1907 2727–2729. Retrieved from [https://journals.asm.org/doi/abs/10.1128/aem.59
1908 .8.2727–2729.1993](https://journals.asm.org/doi/abs/10.1128/aem.59.8.2727-2729.1993) doi: 10.1128/aem.59.8.2727-2729.1993
- 1909 Piceda, C., Franceschinis, P., Escayola, M., & Rapalini, A. (2018). Paleomagnetism of the
1910 santa victoria group in the mojotoro range, salta: Contributions to the paleogeographic
1911 position of pampia in early paleozoic [paleomagnetismo del grupo santa victoria en
1912 la sierra de mojotoro, salta: Aportes a la reconstrucción pal. *Rev. la Asoc. Geol.*
1913 *Argentina*, 75(4), 518–532,. Retrieved from [https://revista.geologica.org.ar/
1914 raga/article/view/134](https://revista.geologica.org.ar/raga/article/view/134). (Online]. Available:)
- 1915 Pike, C., Roberts, A., Dekkers, M., & Verosub, K. (2001). An investigation of multi-domain
1916 hysteresis mechanisms using forc diagrams. *Phys. Earth Planet. Inter*, 126(1–2),
1917 11–25,. Retrieved from [https://doi.org/10.1016/S0031-9201\(01\)00241-2](https://doi.org/10.1016/S0031-9201(01)00241-2). doi:
1918 10.1016/S0031-9201(01)00241-2.
- 1919 Piquer, C., Laguna-Marco, M., Roca, A., Boada, R., Guglieri, C., & Chaboy, J. (2014). Fe
1920 k-edge x-ray absorption spectroscopy study of nanosized nominal magnetite. *J. Phys.*
1921 *Chem*, 118(2), 1332–1346,. doi: 10.1021/jp4104992.
- 1922 Potter, D., Corbett, P., Barclay, S., & Haszeldine, R. (2004). Quantification of illite content
1923 in sedimentary rocks using magnetic susceptibility - a rapid complement or alternative
1924 to x-ray diffraction. *J. Sediment. Res*, 74(5), 730–735,. doi: 10.1306/021304740730.
- 1925 Pourbaix, M. (1974). *Atlas of Electrochemical Equilibria in Aqueous Solutions* (1st ed.,
1926 Vol. 2). Houston: National Association of Corrosion Engineers. doi: 1
- 1927 Pullaiah, G., Irving, E., Buchan, K., & Dunlop, D. (1975). Magnetization changes
1928 caused by burial and uplift. *Earth Planet. Sci. Lett*, 28(1), 133–143,. doi: 10.1177/
1929 001139217502300101.
- 1930 Ravel, B. (2013). Xas-education, examples, fes2. In *Transmission scan of*
1931 *fes2*. Retrieved from [https://github.com/bruceravel/XAS-Education/blob/
1932 06b144d1a3418c3f1ddec2454167d62f58f1f256/Examples/FeS2/fes2_rt01_mar02
1933 .xmu](https://github.com/bruceravel/XAS-Education/blob/06b144d1a3418c3f1ddec2454167d62f58f1f256/Examples/FeS2/fes2_rt01_mar02.xmu) (accessed Oct. 10, 2022).)
- 1934 Ravel, B., & Newville, M. (2005). Athena , artemis , hephaestus : data analysis for x-ray
1935 absorption spectroscopy using ifeffit. *J. Synchrotron Radiat*, 12(4), 537–541,. doi:
1936 10.1107/S0909049505012719.
- 1937 Riccomini, C., Nogueira, A., & Sial, A. (2007). Carbon and oxygen isotope geochemistry
1938 of ediacaran outer platform carbonates, paraguay belt, central brazil. *An. Acad. Bras.*
1939 *Cienc*, 79(3), 519–527,. doi: 10.1590/s0001-37652007000300012.

- 1940 Rickard, D. (1995). Kinetics of fcs precipitation: Part 1. competing reaction mechanisms.
 1941 *Geochimica et Cosmochimica Acta*, 59(21), 4367-4379. Retrieved from <https://www>
 1942 [.sciencedirect.com/science/article/pii/S001670379500251T](https://www.sciencedirect.com/science/article/pii/S001670379500251T) doi: <https://doi>
 1943 [.org/10.1016/0016-7037\(95\)00251-T](https://doi.org/10.1016/0016-7037(95)00251-T)
- 1944 Rickard, D., & Luther, G. (2007). Chemistry of iron sulfides. *Chem. Rev*, 107(2), 514–562.,
 1945 doi: 10.1021/cr0503658.
- 1946 Roberts, A. (2011). Magnetotactic bacterial abundance in pelagic marine environments is
 1947 limited by organic carbon flux and availability of dissolved iron. *Earth Planet. Sci.*
 1948 *Lett*, 310(3–4), 441–452., doi: 10.1016/j.epsl.2011.08.011.
- 1949 Roberts, A. (2015). Magnetic mineral diagenesis. *Earth-Science Reviews*, 151, 1–47.
 1950 Retrieved from <http://dx.doi.org/10.1016/j.earscirev.2015.09.010> doi: 10
 1951 [.1016/j.earscirev.2015.09.010](https://doi.org/10.1016/j.earscirev.2015.09.010)
- 1952 Roberts, A. (2022). Unlocking information about fine magnetic particle assemblages
 1953 from first-order reversal curve diagrams: Recent advances. *Earth-Science Rev*,
 1954 227(January), 103950., (p.) doi: 10.1016/j.earscirev.2022.103950.
- 1955 Roberts, A., Florindo, F., Chang, L., Heslop, D., Jovane, L., & Larrasoña, J. (2013).
 1956 Magnetic properties of pelagic marine carbonates. *Earth-Science Rev*, 127, 111–139.,
 1957 doi: 10.1016/j.earscirev.2013.09.009.
- 1958 Roberts, A., Heslop, D., Zhao, X., & Pike, C. (2014). Understanding fine magnetic particle
 1959 systems through use of first-order reversal curve diagrams. *Rev. Geophys*, 52(4),
 1960 557–602., doi: 10.1002/2014RG000462.
- 1961 Roberts, A., Pike, C., & Verosub, K. (2000). First-order reversal curve diagrams: A new
 1962 tool for characterizing the magnetic properties of natural samples. *J. Geophys. Res.*
 1963 *Solid Earth*, 105(B12), 28461–28475., doi: 10.1029/2000jb900326.
- 1964 Rochette, P., Ménard, G., & Dunn, R. (1992, 02). Thermochronometry and cooling rates
 1965 deduced from single sample records of successive magnetic polarities during uplift of
 1966 metamorphic rocks in the Alps (France). *Geophysical Journal International*, 108(2),
 1967 491-501. Retrieved from <https://doi.org/10.1111/j.1365-246X.1992.tb04630.x>
 1968 doi: 10.1111/j.1365-246X.1992.tb04630.x
- 1969 Rodrigues, J. (2008). *Proveniência de sedimentos dos grupos canastra, ibiá, vazante e*
 1970 *bambuú - um estudo de zircões detriticos e idades modelo sm-nd*. Universidade de
 1971 Brasília.
- 1972 Sacek, V. (2014). Drainage reversal of the amazon river due to the coupling of surface
 1973 and lithospheric processes. *Earth Planet. Sci. Lett*, 401, 301–312., doi: 10.1016/
 1974 [j.epsl.2014.06.022](https://doi.org/10.1016/j.epsl.2014.06.022).
- 1975 Santana, A., Chemale, F., Scherer, C., Guadagnin, F., Pereira, C., & Santos, J. (2021). Pale-
 1976 ogeographic constraints on source area and depositional systems in the neoproterozoic
 1977 irecê basin, são francisco craton. *J. South Am. Earth Sci*, 109(February 2020). doi:
 1978 10.1016/j.jsames.2021.103330.
- 1979 Schreiner, W. (2002). Paramagnetic anisotropy of a natural kaolinite and its modification
 1980 by chemical reduction. *J. Magn. Magn. Mater*, 241(2–3), 422–429., doi: 10.1016/
 1981 [S0304-8853\(01\)00480-2](https://doi.org/10.1016/S0304-8853(01)00480-2).
- 1982 Shi, Q., & Wu, J. (2021). Review on sulfur compounds in petroleum and its products: State-
 1983 of-the-art and perspectives. *Energy & Fuels*, 35(18), 14445–14461., doi: 10.1021/
 1984 [acs.energyfuels.1c02229](https://doi.org/10.1021/acs.energyfuels.1c02229).
- 1985 Shulman, G., Yafet, Y., Eisenberger, P., & Blumberg, W. (1976). Observations and inter-
 1986 pretation of x-ray absorption edges in iron compounds and proteins. *Proc. Natl. Acad.*
 1987 *Sci. U. S. A*, 73(5), 1384–1388., doi: 10.1073/pnas.73.5.138.
- 1988 Stacey, F., & Banerjee, S. K. (1974). *The Physical Principles of Rock Mag-*
 1989 *netism*. Elsevier. Retrieved from [https://linkinghub.elsevier.com/retrieve/](https://linkinghub.elsevier.com/retrieve/pii/S001670379500251T)
 1990 [pii/001282527490110X](https://doi.org/10.1016/0016-7037(95)00251-T)
- 1991 Stamatakos, J., Hirt, A., & Lowrie, W. (1996). The age and timing of folding in the central
 1992 appalachians from paleomagnetic results. *GSA Bulletin*, 108, 815–829.
- 1993 Strehlau, J., Hegner, L., Strauss, B., Feinberg, J., & Penn, R. (2014). Simple and efficient
 1994 separation of magnetic minerals from speleothems and other carbonates. *J. Sediment.*

- 1995 *Res*, 84(11), 1096–1106,. doi: 10.2110/jsr.2014.89.
- 1996 Szczerba, M., Kłapyta, Z., & Kalinichev, A. (2014). Ethylene glycol intercalation in smec-
1997 tites. molecular dynamics simulation studies. *Appl. Clay Sci*, 91–92, 87–97,. doi:
1998 10.1016/j.clay.2014.02.014.
- 1999 Sánchez-Bettucci, L., & Rapalini, A. (2002). Paleomagnetism of the sierra de las animas
2000 complex, southern uruguay: its implications in the assembly of western gondwana.
2001 *Precambrian Res*, 118(3–4), 243–265,. doi: 10.1016/S0301-9268(02)00114-6.
- 2002 Tauxe, L., Banerjee, S., Butler, R., & van der Voo, R. (2018). *Essentials of paleomagnetism:*
2003 *Third web edition*. UC Press. Retrieved from [https://earthref.org/MagIC/books/](https://earthref.org/MagIC/books/Tauxe/Essentials/)
2004 [Tauxe/Essentials/](https://earthref.org/MagIC/books/Tauxe/Essentials/)
- 2005 Tauxe, L., Mullender, T., & Pick, T. (1996). Potbellies, wasp-waists, and superparam-
2006 agnetism in magnetic hysteresis. *J. Geophys. Res. Solid Earth*, 101(B1), 571–583,.
2007 Retrieved from <https://doi.org/10.1029/95JB03041>. doi: 10.1029/95JB03041.
- 2008 Tedeschi, M. (2016). The ediacaran rio doce magmatic arc revisited (araçuaí-ribeira orogenic
2009 system, se brazil. *J. South Am. Earth Sci*, 68, 167–186,. Retrieved from [https://](https://doi.org/10.1016/j.jsames.2015.11.011)
2010 doi.org/10.1016/j.jsames.2015.11.011. doi: 10.1016/j.jsames.2015.11.011.
- 2011 Temporim, F., Bellon, U., Domeier, M., Trindade, R., & Agrella-filho, M. (2021). Con-
2012 straining the cambrian drift of gondwana with new paleomagnetic data from post-
2013 collisional plutons of the araçuaí orogen, se brazil. *Precambrian Res*, 359(December
2014 2020), 106212,. (p.) doi: 10.1016/j.precamres.2021.106212.
- 2015 Tohver, E., D’Agrella-Filho, M., & Trindade, R. (2006). Paleomagnetic record of africa and
2016 south america for the 1200-500 ma interval, and evaluation of rodinia and gondwana
2017 assemblies. *Precambrian Res*, 147(3–4), 193–222,. doi: 10.1016/j.precamres.2006.01
2018 .015.
- 2019 Tohver, E., Trindade, R., Solum, J., Hall, C., Riccomini, C., & Nogueira, A. (2010).
2020 Closing the clymene ocean and bending a brasiliano belt: Evidence for the cambrian
2021 formation of gondwana, southeast amazon craton. *Geology*, 38(3), 267–270,. doi:
2022 10.1130/G30510.1.
- 2023 Tohver, E., Weil, A., Solum, J., & Hall, C. (2008). Direct dating of carbonate remagnetiza-
2024 tion by 40ar/39ar analysis of the smectite – illite transformation. *Earth Planet. Sci.*
2025 *Lett*, 274, 524–530,. doi: 10.1016/j.epsl.2008.08.002.
- 2026 Tolentino, H. (2017). CarnaÚba: The coherent x-ray nanoprobe beamline for the brazilian
2027 synchrotron sirius/lpls. *J. Phys. Conf. Ser*, 849, 012057,. doi: 10.1088/1742-6596/
2028 849/1/012057.
- 2029 Tolentino, H. (2021). X-ray microscopy developments at sirius-lpls: first commissioning ex-
2030 periments at the carnauba beamline. In *X-ray nanoimaging: Instruments and methods*
2031 *v* (p. 6,). doi: 10.1117/12.2596496.
- 2032 Torsvik, T. (2012). Phanerozoic polar wander, palaeogeography and dynamics. *Earth-*
2033 *Science Rev*, 114(3–4), 325–368,. doi: 10.1016/j.earscirev.2012.06.007.
- 2034 Torsvik, T., & Cocks, L. (2013). Gondwana from top to base in space and time. *Gondwana*
2035 *Res*, 24(3–4), 999–1030,. doi: 10.1016/j.gr.2013.06.012.
- 2036 Trindade, R., D’Agrella-Filho, M., Babinski, M., Font, E., & Brito, B. (2004). Paleomag-
2037 netism and geochronology of the bebedouro cap carbonate : evidence for continental-
2038 scale cambrian remagnetization in the são francisco craton , brazil. *Precambrian Res*,
2039 128, 83–103,. doi: 10.1016/j.precamres.2003.08.010.
- 2040 Trindade, R., Font, E., D’Agrella-Filho, M., Nogueira, A., & Riccomini, C. (2003). Low-
2041 latitude and multiple geomagnetic reversals in the neoproterozoic puga cap carbonate,
2042 amazon craton. *Terra Nov*, 15(6), 441–446,. doi: 10.1046/j.1365-3121.2003.00510.x.
- 2043 Trindade, R., & Macouin, M. (2007, mar). Palaeolatitude of glacial deposits and
2044 palaeogeography of Neoproterozoic ice ages. *Comptes Rendus Geoscience*, 339(3-4),
2045 200–211. Retrieved from [https://www.sciencedirect.com/science/article/](https://www.sciencedirect.com/science/article/pii/S1631071307000338)
2046 [pii/S1631071307000338](https://www.sciencedirect.com/science/article/pii/S1631071307000338)[https://linkinghub.elsevier.com/retrieve/pii/](https://linkinghub.elsevier.com/retrieve/pii/S1631071307000338)
2047 [S1631071307000338](https://linkinghub.elsevier.com/retrieve/pii/S1631071307000338) doi: 10.1016/j.crte.2007.02.006
- 2048 Tucker, M. (2001). *Sedimentary petrology. an introduction to the orgin of sedimentary rocks*.
2049 Blackwell Science Ltd.

- 2050 Vauchez, A., Hollanda, M., Monié, P., Mondou, M., & Egydio-Silva, M. (2019). Slow cooling
2051 and crystallization of the roots of the neoproterozoic araquai hot orogen (se brazil): Im-
2052 plications for rheology, strain distribution, and deformation analysis. *Tectonophysics*,
2053 *766*(October), 500–518,. doi: 10.1016/j.tecto.2019.05.013.
- 2054 Wang, Y. (2022). Micromagnetic modeling of a magnetically unstable zone and its geological
2055 significances. *J. Geophys. Res. Solid Earth*, *127*(9), 1–14,. doi: 10.1029/2022JB024876
- 2056 .
- 2057 Wiedemann, C., Medeiros, S., Ludka, I., Mendes, J., & Costa-de Moura, J. (2002). Ar-
2058 chitecture of late orogenic plutons in the araquai-ribeira fold belt, southeast brazil.
2059 *Gondwana Res*, *5*(2), 381–399,. doi: 10.1016/S1342-937X(05)70730-9.
- 2060 Wohlfarth, E., & Tonge, D. (1957). The remanent magnetization of single domain ferromag-
2061 netic particles. *Philos. Mag*, *2*(23), 1333–1344,. doi: 10.1080/14786435708243210.
- 2062 Woods, S. D., Elmore, R. D., & Engel, M. H. (2002). Paleomagnetic dating of the
2063 smectite-to-illite conversion: Testing the hypothesis in jurassic sedimentary rocks,
2064 skye, scotland. *Journal of Geophysical Research: Solid Earth*, *107*(B5), EPM 2-1-
2065 EPM 2-10. Retrieved from [https://agupubs.onlinelibrary.wiley.com/doi/abs/](https://agupubs.onlinelibrary.wiley.com/doi/abs/10.1029/2000JB000053)
2066 [10.1029/2000JB000053](https://doi.org/10.1029/2000JB000053) doi: <https://doi.org/10.1029/2000JB000053>
- 2067 Xu, Y., Tan, X., Li, S., Li, Y., Ran, B., Han, Y., . . . Ma, Z. (2022). Paleomagnetism
2068 of the greater indian passive margin sediments from the upper cretaceous succession:
2069 Evidence for long-delayed remagnetizations and implication for the india-asia collision.
2070 *Journal of Asian Earth Sciences*, *229*, 105165. Retrieved from [https://doi.org/](https://doi.org/10.1016/j.jseaes.2022.105165)
2071 [10.1016/j.jseaes.2022.105165](https://doi.org/10.1016/j.jseaes.2022.105165) doi: 10.1016/j.jseaes.2022.105165
- 2072 Yamashita, H. (2003). Xafs analysis and applications to carbons and catalysts. In *Carbon*
2073 *alloys: Novel concepts to develop carbon science and technology* (p. 189–209). Elsevier
2074 Ltd.
- 2075 Zhao, H., Cao, Y., Sit, S., Lineberry, Q., & Pan, W. (2012). Thermal characteristics
2076 of bitumen pyrolysis. *J. Therm. Anal. Calorim*, *107*(2), 541–547,. doi: 10.1007/
2077 [s10973-011-1590-x](https://doi.org/10.1007/s10973-011-1590-x).
- 2078 Zhu, J., Zeng, Z., & Li, W. (2021). K-edge xanes investigation of fe-based oxides by
2079 density functional theory calculations. *J. Phys. Chem. C*, *125*(47), 26229–26239,.
2080 doi: 10.1021/acs.jpcc.1c08461.
- 2081 Zumaquero, E., Gilabert, J., Díaz-Canales, E., Gazulla, M., & Gómez-Tena, M. (2021).
2082 Study on sulfide oxidation in a clay matrix by the hyphenated method. *Minerals*,
2083 *11*(10), 1121,. doi: 10.3390/min11101121.
- 2084 Zunino, F., & Scrivener, K. (2022). Oxidation of pyrite (fes₂) and troilite (fes) impurities
2085 in kaolinitic clays after calcination. *Mater. Struct*, *55*(1), 9,. doi: 10.1617/s11527-021-
2086 -01858-9.